Dynamics in Discrete Time: Successional Communities, Spatial Models, and Allee Effects

Nora Gilbertson

A dissertation
submitted in partial fulfillment of the
requirements for the degree of

Doctor of Philosophy

University of Washington

2022

Reading Committee:

Mark Kot, Chair

Bernard Deconinck

Mark Lewis

Program Authorized to Offer Degree:
Applied Mathematics

University of Washington

Abstract

Dynamics in Discrete Time: Successional Communities, Spatial Models, and Allee Effects

Nora Gilbertson

Chair of the Supervisory Committee:
Associate Professor Mark Kot
Department of Applied Mathematics

As humans rapidly alter the environment around them, impacts such as habitat disturbances and fragmentation, range shifts, and invasions are increasingly common. In the face of these events, knowledge of population dynamics and how these dynamics may respond to changing environmental factors is of particular relevance. Mathematical models can help analyze such population behavior, and their predictions can aid decision-making regarding species conservation, habitat design, biological control, and other matters related to ecosystem management. In this dissertation, I build and analyze several discrete-time population models, including developing a method for analyzing the spatial models known as integrodifference equations (IDEs). First, I describe the ecological underpinnings of the models and the mathematical components of both nonspatial and spatial discrete-time models.

Next, I examine a reduced successional community. Succession may become more common with increased habitat disturbances and with climate change opening new ecological niches for species. I present a simple mathematical model for the dynamics of a successional pioneer–climax system using difference equations, where the climax population is subject to an Allee effect. Each population is subject to inter- and intraspecific competition; population growth is dependent on the combined densities of both species. I fully characterize the long-term dynamics of the model, uncovering diverse sets of potential behaviors including some behaviors not previously seen in

pioneer–climax models. Competitive exclusion of the pioneer species and of the climax species are both possible depending on the relative strength of competition. Stable coexistence of both species may also occur at both fixed population-densities and fluctuating densities. The abrupt loss of a coexistence state, shifting the system to an exclusion state, is also possible.

Then I consider IDEs, popular models for exploring a variety of problems related to population persistence and spread. I present a novel method for approximating the equilibrium population-distributions of IDEs with strictly-increasing growth, for populations on a finite habitat-patch. This method approximates the growth function of the IDE with a piecewise-constant function, and I call the resulting model a block-pulse IDE. I write out analytic expressions for the iterates and equilibria of the block-pulse IDEs as sums of cumulative distribution functions. I characterize the dynamics of one-, two-, and three-step block-pulse IDEs, including stability analyses and an exploration of bifurcation structure. I demonstrate the use of block-pulse IDEs by using three-, five-, and ten-step block- pulse IDEs to approximate models with compensatory Beverton-Holt growth and depensatory, or Allee-effect, growth. For the IDE with Allee-effect growth, I also calculate the critical patch-size needed for persistence for several dispersal kernels, showing that this patch size depends on the choice of dispersal kernel when an Allee effect is involved.

Finally, I conclude with some of the implications of these results. I discuss open problems and extensions of the current models and methods, and motivate paths for future exploration.

TABLE OF CONTENTS

LIST OF FIGURES

LIST OF TABLES

ACKNOWLEDGMENTS

The things that are good in life are good because of the people who have had a hand in them. Whether or not they are aware of it, whether or not they enjoy math, whether or not they are named here, I would like to thank all those who have made this thing called a PhD *good*.

Chief among these people is my advisor, Mark Kot. I have been incredibly privileged to learn from him, and the knowledge I have gained is immeasurable. Thank you to Mark for not only increasing my mathematical and ecological knowledge in breadth and depth, but also for fostering my writing skills, my historical perspectives, and my supply of interesting facts. Your patient mentoring and cheerful enthusiasm have made the past years something very good indeed. I would also like to thank the other members of my committee, Bernard Deconinck, Mark Lewis, and Patrick Tobin, for their guidance, knowledge, and insightful discussions.

My immense gratitude goes to the Department of Applied Mathematics as a whole, for being a welcoming and supportive community throughout my time at UW. From faculty to staff to students, I do not think I could have landed in a better place. I would particularly like to thank Lauren Lederer, Tony Garcia, and Nick Cheung, whose help, support, and kindness have made this department run smoothly and made my own time here so much better. Thank you also to UW STEMsub staff, instructors, and students, who gave me the opportunity to teach and taught me in turn.

To my cohort, Tyler Chen, Jorge Cisneros, Micah Henson, Roman Levin, Yuying Liu, Katherine Owens, Diya Sashidhar, and Ying-Jen Yang: thank you for being the best cohort in the world. I could not have done this without all of you, from the very first day we met. To Ryan Creedon, Beth Sutherland, Ben Liu, Kelsey Marcinko, and Kelsey Maass, thank you for laughter, conversations both academic and not, and being stalwart friends. I am forever grateful for your friendship, your

kindness, and your remarkable minds.

To the women of the department and those of my cohort in particular, who created an incredible community and offered much-needed support – thank you for your commiseration, encouragement, and celebration. Thank you to the WAMM program and my mentees Yinxi Pan, Jan Dee, and Chloë Mitchell, and my independent research mentee Lisa Li. Each of these women have inspired me, reminded me of why I am here, and taught me in so many valuable ways.

To Sophie and Zach LaFond-Hudson, Kris Hansen and Peter Bohacek, Morghen Philippi, Amelia Schurke, and Shelby Ahrendt, thank you for your generosity of spirit, your intellectual inspiration, and your endless encouragement. To Elizabeth McNaughton, thank you for cheering me on since your day one and never failing to make me smile.

To Euan Smithers, Ashleigh Trinh, and my York cohort, thank you for snack supplies, for Sunday dinners, for silliness and seriousness, and for making a year living abroad the best experience I've ever had. To the faculty at the University of York, the Scottish Association for Marine Science, and Tom Adams and Mike Burrows in particular, thank you for fostering my intellectual development, your guidance as I learned the ropes of research, and the chance to go canoeing on the ocean and hunting for sea gliders.

To the Momentum Northwest ski team, thank you for deciding a random handful of graduate students needed to destress a bit by coaching a youth ski team – you were right. To Kristine Hampton, thank you for talks over tea, delicious baked goods, and your friendship, which was by far the best thing to come out of TA orientation. To Laura Moore, thank you for skis and walks and hikes and climbs, for your unrelenting optimism and support, for enabling me in the pursuit of ice cream and the pursuit of a PhD and everything in between, and for your resolute friendship that has seen me through these past years.

To my family who has cheered me on, thank you. It is the most fundamental truth that I would not be here without my parents. They gave me the freedom to pursue my interests, unfailing

encouragement to believe that I could succeed, and the support to actually do so. I may have confused them a bit when I decided math was the thing for me, but that never stopped them listening to me describe my work. Their love and confidence has buoyed me in moments of difficulty and reassured me even when things ran smoothly, and I am beyond privileged to be their daughter. As my final and most important acknowledgement, to Mom and Dad – thank you.

DEDICATION

To my mentors, my mentees, and all those who are curious

Chapter 1

INTRODUCTION

From the inception of ecology as a scientific field, scientists have been interested in the dynamic processes of populations and communities and have used mathematical models to examine these dynamics [92, 111]. Such models are powerful tools for analyzing the behavior of a population over time, allowing us to distill intricate ecological factors into more manageable parts. Population models offer a way to study questions relating to population behavior and persistence that often cannot be answered solely through empirical study. Among many other topics, mathematical models can help in predicting population responses to changing environmental factors, interactions between populations, and the dynamics of biological invasions. Such predictions can, in turn, inform decisions made in resource management, conservation, or biological control [103, 126].

There is a rich diversity among the types of population models that exist, with each type of model offering unique insight into certain classes of populations. One major class of models is discrete-time difference equations. These nonspatial models are appropriate for populations that have distinct, non-overlapping generations.

Spatial components often play a major role in population dynamics. Integrodifference equations (IDEs) are a popular method of modeling populations in discrete time and continuous space. IDEs are particularly useful when considering a population that, in addition to having non-overlapping generations, grows and disperses in distinct phases. This is a category of populations that includes many annual plants and insect species. Difference-equation models and IDEs may also be useful for populations whose growth is censused in discrete intervals.

1.1 Nonspatial dynamics: Difference-equation models

I focus on mechanistic models, both nonspatial and spatial, for populations that grow in discrete generations. Difference equations form the fundamental backbone of the models considered in this thesis. The general form of the nonspatial difference-equation model under consideration is

$$n_{t+1} = f(n_t)\, n_t = g(n_t), \tag{1.1}$$

where n_t is the population density in generation t and the product $g(n_t) = f(n_t)\, n_t$ is known as the growth or recruitment function. The function $f(n_t)$ is the per-capita number of recruits for the population, also known as the per-capita replacement rate, per-capita number of progeny, or the fitness function.

I am predominantly interested in understanding the long-term behavior of populations. When examining the long-term dynamics of a difference-equation model, I look for solutions of the model where the population is not changing over time, so that the population density is at equilibrium. In the difference equation above, these equilibrium solutions, or fixed points, satisfy $n_{t+1} = n_t = n$. In other words, we find the equilibrium population-densities n by solving

$$n = f(n)\, n. \tag{1.2}$$

The trivial fixed-point $n = 0$ is always a solution. Any other fixed points occur when the per-capita number of recruits is equal to one, $f(n) = 1$, so that each individual is exactly replacing itself.

Now, consider two species whose population densities at generation t are given by n_t and p_t. A general two-species difference-equation model is

$$n_{t+1} = f_n(n_t, p_t)\; n_t = g_n(n_t, p_t), \tag{1.3a}$$

$$p_{t+1} = f_p(n_t, p_t)\; p_t = g_p(n_t, p_t), \tag{1.3b}$$

where $f_n(n_t, p_t)$ and $f_p(n_t, p_t)$ are species-specific per-capita numbers of recruits. (Please note that precise notation varies slightly between chapters.) Fixed points of this system occur when both populations are at equilibrium, so that $n_{t+1} = n_t = n$ and $p_{t+1} = p_t = p$ are both satisfied.

1.2 Spatial models: Integrodifference equations

Nonspatial models can provide valuable insight into population dynamics. Incorporating spatial components, most notably dispersal, adds to this insight and offers a more realistic and nuanced portrayal of population dynamics. The work of Fisher [37] in population genetics later influenced Skellam [127] in his study of invasion waves in ecology. By incorporating dispersal, these studies began the shift from nonspatial to spatiotemporal models of population dynamics. Initially, dispersal meant diffusion, and the deterministic models under consideration used diffusion to represent population movement [125, 127].

The reaction-diffusion equations of Skellam [127], continuous in both time and space, are a precursor to the discrete-time and continuous-space IDE models. IDEs, though not under that name, first emerged in population genetics with the work of Slatkin [128], Weinberger [144], and Lui [83]. IDEs were later formalized in population ecology [64]. In many cases, IDEs provide more ecological realism than the classical reaction-diffusion models by accounting for long-distance dispersal as well as seasonal growth, features which many species possess [98, 3, 21, 84]. As a result, IDEs are frequently used to identify conditions for population persistence and spread in the contexts of environmental change and invasion [97, 36, 86, 153, 47, 45].

Consider a population whose density in generation t at spatial location y is given by $n_t(y)$. In a typical IDE, the population first grows according to some recruitment (or growth) function, $g[n_t(y)]$, and then disperses with probability governed by dispersal kernel $k(x,y)$ (though this order of events may be reversed [86]). The population density in the next generation $t+1$ at a particular spatial location x is

$$n_{t+1}(x) = \int_{\Omega} k(x,y)\, g[n_t(y)]\, dy, \tag{1.4}$$

where Ω is the habitat domain of the population.

There are a variety of ecological problems that IDEs are commonly used to examine. The invasion problem, in which we seek to estimate speeds of spatial spread over an infinite habitat-domain, is one major class of IDE problems [83, 2, 65, 141, 143, 145, 75, 36, 78, 52, 146, 41,

45, 130]. The results of these estimations can be used to try and control establishment and spread of invasive species, or understand conditions under which a population will be able to spread into newly available habitat.

Another key problem is population persistence on a finite habitat-patch, often considered in terms of the critical patch-size needed for persistence [64, 139, 69, 140, 34, 82, 110]. Such models can inform decisions about habitat-reserve design and ecosystem management.

Moving-habitat models consider an IDE with a finite habitat-patch that is shifting at some speed c. The third core IDE problem uses these models to find the critical speed of habitat movement beyond which a population cannot persist [153, 154, 47, 63, 102, 48, 113, 114, 53, 23, 89]. As climate change causes latitudinal and elevational range-shifts in many species [72, 19], these models can offer insight into the conditions under which populations will be able to keep pace with such climate-driven range shifts.

To create a realistic population model, whether nonspatial or spatial, we take key ecological features of the populations in question and distill them into mathematical terms. The underlying ecological system and the biological factors that drive population dynamics are as important to understanding a population model as the mathematical components and tools themselves. Any mathematical model involves simplification of the underlying system, often drastically so. Thus, it is critical that we take care to incorporate the ecological features of the system that most significantly influence population dynamics in order to build a useful model. I now consider the ecological underpinnings of the models that will be analyzed in this dissertation, and how these ecological factors influence model components.

1.3 Population growth

Population growth is frequently considered to be density dependent, so that growth is regulated by density-dependent factors like competition, predation, or disease. (Population growth may also be regulated by density-independent factors, which tend to be abiotic.) Three common forms of

density-dependent growth are compensatory, overcompensatory, and depensatory growth.

In compensatory growth, the per-capita number of recruits $f(n_t)$ is largest at small densities, so that the slope of the recruitment function $g(n_t)$ is steepest at arbitrarily small densities. As population density increases, the per-capita number of recruits decreases, while the overall recruitment of the population increases monotonically but with decreasing slope.

A classical example of compensatory growth is given by the Beverton-Holt model [10],

$$n_{t+1} = \frac{R_0 n_t}{1 + [(R_0 - 1)/K] n_t}, \tag{1.5}$$

where R_0 is the net reproductive rate of the population, or the average number of offspring or propagules from a reproducing individual. The parameter K is the carrying capacity, or the maximum population-density that can be sustained by the environment. There are two equilibria, the trivial extinction state at $n = 0$ and the persistence state at the carrying capacity $n = K$.

With overcompensatory growth, the per-capita number of recruits is also largest at small densities. As density increases, the per-capita number of recruits $f(n_t)$ decreases. At small densities, overall recruitment $g(n_t)$ will increase. However, in contrast to compensatory growth, density dependence is severe enough to cause an overall decrease in recruitment at larger densities.

A typical model for overcompensatory growth is given by the Ricker equation [112],

$$n_{t+1} = e^{r(1-n_t/K)} n_t, \tag{1.6}$$

where $r = \ln R_0$ is the intrinsic rate of growth and K is the carrying capacity. The Ricker model has the same fixed points as the Beverton-Holt model, the extinction state $n = 0$ and the persistence state $n = K$.

The third form of density-dependent growth I consider is depensatory or Allee-effect growth. Also known as positive density dependence, this form of growth happens when the per-capita number of recruits, or fitness, increases with density at low densities [1, 26]. Equivalently, at small densities the per-capita number of recruits decreases as density decreases.

Mechanisms causing an Allee effect often arise from cooperative effects, as opposed to the competitive effects that typically cause negative density dependence [1, 133, 66]. Some of these mechanisms that cause an improvement in fitness as density increases, both cooperative and not, include mate finding, group feeding, predator defense, inbreeding depression, and sex-ratio bias [44, 108, 129, 25, 11, 26]. When population densities are small, there are not enough individuals for the cooperative effects to aid population growth (or non-cooperative effects take their toll). As density increases, the per-capita number of recruits of the population increases as well. Competitive effects or other factors unrelated to the Allee effect typically cause growth to slow or decrease at larger densities.

There are two types of depensatory growth. The first is noncritical depensation or a weak Allee effect. In this case, the per-capita number of recruits increases with density at low densities, but is always above one so that an individual is always at least replacing itself. There are two equilibria for a nonspatial model with a weak Allee effect, the extinction state and a persistence state [11].

The second type of depensatory growth, which is of particular interest here, is critical depensation or a strong Allee effect. The per-capita number of recruits is below one for densities below some threshold, so that at low densities an individual fails to replace itself. This critical threshold is known as the Allee threshold. A third equilibrium point is introduced at the Allee threshold, and populations below this equilibrium will decline to extinction. The Allee threshold, therefore, is extremely important in determining whether a population can persist.

In addition to introducing a population threshold that must be surpassed for persistence, Allee effects may have a variety of other impacts on populations. These impacts are especially notable in spatial models. When dispersal is involved, a population may require a minimum founding-population size that is different from the Allee threshold to survive, as dispersal may push the population below the Allee threshold [45]. In populations that are spreading, Allee effects can slow the rate of spread, introduce a critical range-size necessary for invasion to occur, or prevent range expansion due to the minimum founding-population necessary for establishment [65, 61, 134, 57].

As a result of these impacts, Allee effects are of great interest to ecologists and mathematicians alike, particularly given that Allee effects appear to be widespread in a variety of populations [79, 134]. The mathematical dynamics caused by Allee effects can be quite different from models without Allee effects. Allee effects can greatly impact the survival of endangered or at-risk populations, affecting conservation and ecosystem-management decisions [129, 25, 66]. They may also be leveraged in controlling the spread of invasive species [57, 137].

A simple nonspatial model with a strong Allee effect is given by

$$n_{t+1} = \frac{\left[\left(1+\rho^2\right)/K\right] n_t^2}{1+\left(\rho/K\right)^2 n_t^2}, \tag{1.7}$$

where ρ is the growth parameter and K is the carrying capacity [95, 139]. The Allee growth-model has three equilibria at $n = 0$, $n = K/\rho^2$, and $n = K$. The intermediate equilibrium, $n = K/\rho^2$, is the Allee threshold that the population must surpass in order to persist.

1.4 Dispersal

Understanding the factors that affect a population's growth is one critical component of modeling population dynamics. Another key factor to consider is how the population moves in space, or disperses. We generally model dispersal events with dispersal kernels $k(x,y)$ that give the probability density of an individual moving from a starting location y to some final location x. These kernels may be derived directly from empirical data or mechanistically, using assumptions about the biological factors affecting dispersal [110, 84]. In this dissertation, I assume the dispersal kernels are proper, continuous, and bounded.

As noted earlier, for a long time dispersal was assumed to be diffusive, or Gaussian, which does not account for long-distance dispersal. However, empirical evidence indicates that many species disperse farther and at a faster rate than theoretical predictions using diffusive dispersal would suggest. For plants, this phenomenon is known as Reid's Paradox [21]. Skellam [127], in his analysis of population dynamics subject to diffusive dispersal, found that diffusion alone could not explain the extensive spread of oak trees in Britain after the last ice age. Rather, spread must have

been supported by another factor, such as birds contributing to seed dispersal. As a result of such evidence, leptokurtic and heavy-tailed kernels that account for more long-distance dispersal events have become increasingly popular for modeling population dispersal (e.g., Kot et al. [65], Clark [20], Cain et al. [17], Clark et al. [22], Liu and Kot [80]).

1.5 Successional communities

No population exists in isolation. In addition to growth and dispersal, the interactions between populations are another critical component of population models. Common forms of interaction that are of interest include competition, predation, mutualism, and parasitism, among others.

I am interested in the population interactions in a reduced successional community of plants, known as a pioneer–climax system. Succession is the process by which the community of an ecosystem changes over time [50]. The start of succession occurs after a disturbance to an ecosystem disrupts existing communities or when new, barren habitat is colonized [50, 100]. Thus, the principle of succession is inherent to environmental change.

Human-driven changes to the environment are increasing and putting ever-greater pressure on ecosystems. Perhaps the most obvious and overarching human impact on the natural world is anthropogenic climate change, which has resulted in effects such as warming temperatures, increased environmental disturbances, and population range-shifts [72, 19, 117]. Other changes include human-mediated transport and dispersal of organisms, leading to increasing numbers of biological invasions [73]. Climate change itself can facilitate invasions, as habitats previously unsuitable for non-native species become accessible due to changes in environmental conditions, or an ecological niche opens up as a result of habitat disturbance [142, 31]. As direct human action and anthropogenic climate change cause increased habitat-disturbances and environmental change, successional communities may become more common [117].

A highly simplified successional community is the aforementioned pioneer–climax system, involving a pioneer and climax plant species. The pioneer species is the first to move into new

habitat and to colonize an unpopulated environment [46, 28]. Pioneer species are hardy species that exhibit compensatory growth, doing best at low population-densities [28]. Climax species, on the other hand, are late-successional species that are good competitors but poor colonizers. At low population-densities, they rely on the pioneer species to provide resources that make the new environment tolerable [46, 138]. As a result of this interaction, climax species are subject to a strong Allee effect. Examples of pioneer and climax species pairs include white bursage and creosote bush, Douglas-fir and western hemlock, and quaking aspen and red maple.

1.6 Overview

The mathematical structure of pioneer–climax systems is well established, and the long-term dynamics of differential-equation pioneer–climax models have been thoroughly characterized [14, 15, 62, 120, 131, 132]. Studies of discrete-time models, however, have focused on analysis of the quasi-periodic solutions that arose [120, 121, 122], theoretical proof of criteria for exclusion and coexistence [39, 40], and restoring stability of a fixed point by reversing period-doubling bifurcations [118, 119, 123, 124].

Despite this extensive research, no one had undertaken a thorough investigation of the long-term dynamics of a discrete-time model. In chapter 2, I summarize the development and results of a difference-equation pioneer–climax model [42]. Inter- and intraspecific competitive effects drive population-density growth, and the population's response to density depends on the combined and weighted population-densities of both species. The model demonstrates diverse sets of long-term behaviors, including some novel dynamics regarding quasi-periodic coexistence states. With the results of this model analysis, the behavior of a discrete-time pioneer–climax model is fully characterized, and we gain further insight into the dynamics of successional communities.

With the nonspatial dynamics of a pioneer–climax system in hand, my original intent was to examine moving-habitat models for a climax population on its own and a pioneer–climax system, to determine how critical speeds of habitat-patch movement are affected by the Allee effect in the

climax population. To do so, I used the method of geometric symmetrization [63, 113] to approximate the critical speed beyond which the populations cannot persist. Geometric symmetrization is based on approximating the dominant eigenvalue of the integral operator or, more intuitively, approximating the proportion of individuals that remain in the habitat patch after dispersal. Allee effects typically cause significant analytical challenges in IDEs [84]. The critical-speed problem proved to be no different, as geometric symmetrization did not work with an Allee effect.

In light of this outcome, my focus shifted to analyzing IDEs with an Allee effect. The resulting work is not limited to Allee effects, but is broadly applicable to any increasing growth-function, including populations with compensatory or depensatory growth. In chapter 3, I formalize a method to approximate the equilibrium solutions of an IDE with a strictly-increasing growth-function and a symmetric and unimodal dispersal kernel, calling the resulting model a block-pulse IDE [43]. The block-pulse IDE approximates the growth function of the original model, creating a IDE with significant analytical tractability and allowing for comprehensive analysis, including analytic equilibrium expressions and explicit stability analyses.

The dynamics of block-pulse IDEs are surprisingly intricate on their own. Of more interest, however, is their usefulness in closely approximating the equilibrium solutions of the original IDE. With block-pulse IDEs, we obtain both stable and unstable equilibria, gain valuable information about spatial variation of the equilibrium population-distributions, and can calculate the critical patch-size needed for population persistence for a variety of dispersal kernels. It is my hope that the framework established here can be extended to other problems in spatial ecology, broadening the scope of problems we may analytically consider when an Allee effect is involved.

As with any body of research, persistent questions remain. In chapter 4, I discuss what I consider to be some of the most interesting questions for future exploration. By then, the relevance of successional communities, Allee effects, and population dynamics in an ever-changing environment should be clear. I have been continually inspired to examine the problems explored in this dissertation by both the underlying ecological motivations and the mathematical methods. It is

my hope that the preceding chapters and the questions posed in chapter 4 may similarly motivate others to explore such dynamics themselves.

Chapter 2

DYNAMICS OF A DISCRETE-TIME PIONEER–CLIMAX MODEL

2.1 Introduction

In ecological succession, newly established habitat is initially composed of pioneer plants, hardy species that do best at low population-densities and that can colonize unpopulated environments [46, 138, 28]. Later in succession come climax species, which are strong competitors but poor colonizers [46, 138]. At low population-densities, climax plants typically cannot persist on their own, and pioneer species act as nurse plants in a commensal interaction [46, 120]. As population density of the climax species increases, interaction dynamics become more competitive and the climax species tends to thrive [120, 100]. In nature, there are many pairs of plants that interact in this manner. White bursage and creosote bush from the Sonoran Desert, a pioneer species and a climax species, are one such pair [91].

Modeling pioneer–climax dynamics with systems of both differential and difference equations has a rich history [120, 39, 40, 15, 122, 131, 123, 62]. In these models, the long-term behavior of both species depends on inter- and intraspecific competition, and each species reacts differently to these competitive effects. Most pioneer–climax models distinguish density-dependent effects from competition using a total-density variable, a linear combination of the population densities of both pioneer and climax species weighted by competitive effects. Competitive effects are thus dependent only on individual population-densities. The models then assume that the per-capita replacement rate, or fitness, of each species is a function of the total-density variable, so that the species' response to density is modeled by this fitness function.

A pioneer species' fitness function is a monotonically decreasing function of total density [120]. A climax species, on the other hand, does poorly at low densities. As total density increases, its

fitness increases, until overcrowding at high densities results in a decrease in fitness [120], forming a one-humped function. Such fitness functions match ecological observations, incorporating the dependence of the climax species on the pioneer at low densities for resources such as shade or shelter [46, 91]. This formulation also includes the pioneer species being generally outcompeted by the climax species as density increases [91].

Initially, most researchers assumed that the eventual result of any pioneer–climax dynamical model would be pioneer exclusion, an assumption supported by model results and ecological theory [46, 120, 39]. Habitat disturbances that prevent a stable state with only climax species are likely to occur [136, 28], but scientists believed an undisturbed system would always result in climax species dominance. Selgrade and Namkoong [120], however, demonstrated the possibility of long-term dynamics other than pioneer exclusion by finding a Hopf bifurcation that led to stable periodic behavior and coexistence.

After this seminal work, more evidence for a variety of steady-state behaviors emerged [39, 40, 14, 62]. Much of this research used differential equations [118, 15, 131, 62, 24]. Studies that employed difference equations generally focused on analysis of the possible Neimark–Sacker bifurcation, the discrete-time equivalent of a Hopf bifurcation, or theoretical proof of exclusion and coexistence principles [120, 121, 39, 40, 122]. From these initial studies, pioneer–climax research turned to studying how a forcing term, representing stocking or harvesting, might be able to restore stability in the system after a Hopf or period-doubling bifurcation has occurred [118, 15, 122, 131, 119, 124, 132]. To this point, no one has undertaken a more general overview of the behavior of a simple pioneer–climax difference-equation model.

We aim to provide such an overview, in order to understand the full long-term dynamics of a discrete-time model for the first time. With this comprehensive analysis, we gain further insight into how difference-equation models may contrast with differential-equation models, and we shed light on the unique behaviors a discrete-time model may reveal. In particular, we would like to know if difference-equation models are likely to exhibit behaviors such as multiple stable states or

dangerous bifurcations leading to sudden regime shifts. We are also interested in whether pioneer persistence-states or coexistence states are common in this discrete-time model.

In this chapter, we present a basic pioneer–climax difference-equation model using similar assumptions to prior studies. In section 2.2, we describe the model and its development. In this section, we also nondimensionalize our model. Using a total-density variable, we separate inter- and intraspecific competition effects and model the fitness of each species as a function of the total-density variable. We use simple rational forms, for both fitness functions, that are constructed in keeping with earlier model assumptions and ecological theory.

In section 2.3, we characterize the zero-growth isoclines that provide the framework for our stability analysis. We also present the fixed points, or equilibria, of our model, which occur at the intersection of the zero-growth isoclines. Nine different geometric configurations of the zero-growth isoclines occur, as in Buchanan's 1999 analysis using differential equations. These nine cases present scenarios of both competitive exclusion and coexistence.

We perform a steady-state analysis of the long-term behavior of the model in section 2.4 and summarize the results of the stability analysis for all nine geometric cases. The full stability analysis is contained in appendix A.2, appendix B.2, and appendix C.2.

In two of the above cases, Neimark–Sacker bifurcations occur. We examine these bifurcations in section 2.5. In section 2.6, we highlight a global bifurcation similar to the heteroclinic cycle found in the differential-equation model of Kim and Marlin [62], as well as another global bifurcation, a homoclinic bifurcation, not previously found in pioneer–climax models. We also present numerical simulations that show the changing stabilities of the fixed points or limit cycles as the bifurcations occur.

In section 2.7, we describe both the implications of our findings and how our work motivates future research. Our results provide insight into the persistence of pioneer and climax plant species and highlight previously unobserved global behavior of discrete-time pioneer–climax models. The investigation presented here also opens the door to new research, setting the stage for examining

pioneer–climax models in a spatial context. In particular, this framework allows us to examine the invasion ecology of a spatial pioneer–climax model with flexible dispersal kernels and distinct growth and dispersal stages. As climate change alters ecosystems and induces range shifts in many species, we may see more successional communities, making such analyses highly valuable.

2.2 Model

2.2.1 Model development

We consider a model where sufficient resources exist that the per-capita replacement rates of the pioneer and climax species depend only on total-density variables, linear combinations of pioneer and climax densities weighted by competition coefficients. This construction allows us to distinguish between a species' response to density and its response to competitive effects. Let P_t and C_t be the population densities of the pioneer and climax species at time t. The total-density variables for each species are

$$M_t = w_{11}\, P_t + w_{12}\, C_t, \tag{2.1a}$$

$$N_t = w_{21}\, P_t + w_{22}\, C_t, \tag{2.1b}$$

where w_{ij} denotes the competitive effect of species j on species i. We take species 1 to be the pioneer species and species 2 to be the climax species.

The interaction between species is modeled by the system of difference equations

$$P_{t+1} = f(M_t)\, P_t, \tag{2.2a}$$

$$C_{t+1} = g(N_t)\, C_t, \tag{2.2b}$$

where $f(M_t)$ and $g(N_t)$ are the per-capita replacement rates, or fitness functions. We omit consideration of survivorship from one generation to the next (but see section 2.7). Note that for population growth of either species in this discrete-time model its fitness function $f(M_t)$ or $g(N_t)$ must be greater than 1.

We assume that the pioneer species' fitness function $f(M_t)$ is a monotonically decreasing function with respect to density that has a single root $f(M_t) = 1$. To model the pioneer species' dynamics under this assumption, consider the fitness function

$$f(M_t) = \frac{R_1}{1 + aM_t}. \tag{2.3}$$

The net reproductive rate of the pioneer species, R_1, is assumed to be greater than one to reflect the pioneer species' ability to survive on its own at low densities. We group deleterious effects such as overcrowding into the positive parameter a, so that the pioneer species' fitness always decreases with increasing total density, as shown in fig. 2.1a.

The climax species' fitness function $g(N_t)$ is a one-humped function of density with two roots $g(N_t) = 1$. Here, we take

$$g(N_t) = \frac{R_2(1 + b_1 N_t)}{1 + b_2 N_t^2}. \tag{2.4}$$

As with the pioneer species, R_2 is the climax species' net reproductive rate. As the climax species require the pioneer species to facilitate growth at low densities, R_2 is assumed to be less than one. Beneficial effects from the pioneer species acting as nurse plant for the climax species at low densities are incorporated in the positive parameter b_1. The positive parameter b_2, multiplied by the square of the total density, measures deleterious effects on the population at high densities due to effects such as overcrowding. This arrangement gives the desired form of the climax fitness function, increasing at low densities before hitting a maximum and decreasing as total density grows (fig. 2.1b). Thus, the fitness functions presented here match ecological theory on the per-capita replacement rates of pioneer and climax species [46, 91] as well as mathematical convention [120, 62] while maintaining a desirable simplicity.

2.2.2 Nondimensionalization

We scale the above system with respect to intraspecific competition, letting

$$x_t = w_{11}\, P_t, \tag{2.5a}$$

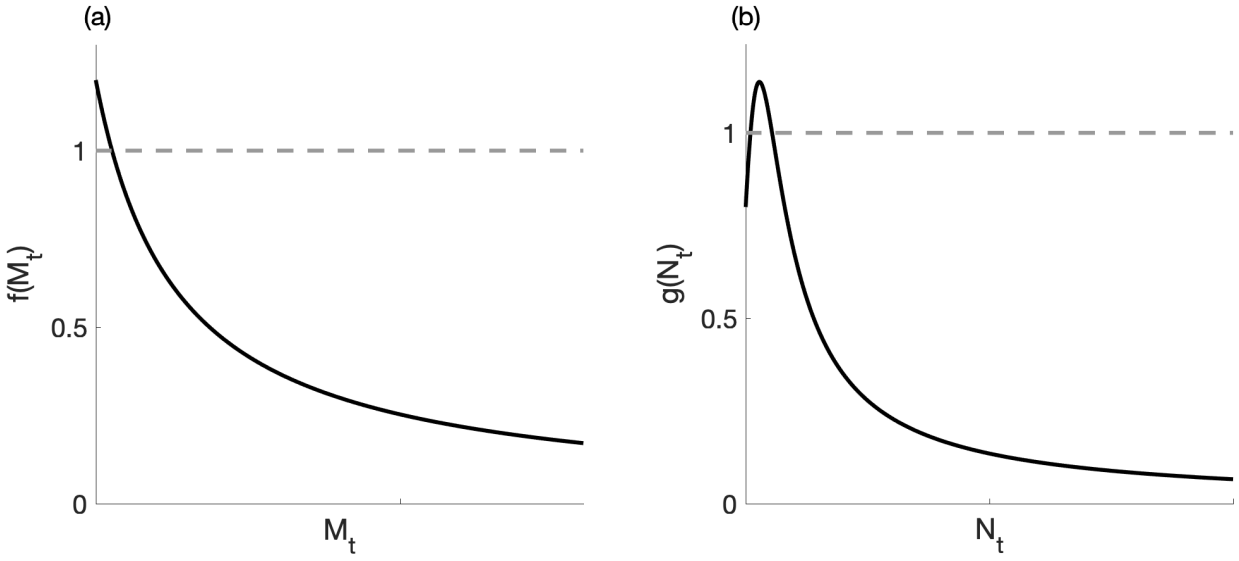

Fig. 2.1 Fitness functions for both species from the dimensional model. **a**, the pioneer species' fitness function $f(M_t)$. **b**, the climax species' fitness function $g(N_t)$. The horizontal dashed gray lines indicate where the fitness function is equal to one, where the root(s) of the functions occur. Parameter values are $R_1 = 1.2$, $R_2 = 0.8$, $a = 0.15$, $b_1 = 0.6$, $b_2 = 0.15$, $w_{11} = 1$, $w_{12} = 2$, $w_{21} = 1.2$, $w_{22} = 1$. Note that these parameter values correspond to the nondimensionalized model with $w_{12} = v_2$ and $w_{21} = v_1$.

$$y_t = w_{22}\, C_t. \tag{2.5b}$$

This rescaling results in the reformulated total-density variables

$$m_t = x_t + \left(\frac{w_{12}}{w_{22}}\right) y_t = x_t + v_2\, y_t, \tag{2.6a}$$

$$n_t = \left(\frac{w_{21}}{w_{11}}\right) x_t + y_t = v_1\, x_t + y_t, \tag{2.6b}$$

where v_1 and v_2 are now relative competition-coefficients measuring the strength of interspecific competition proportionate to intraspecific competition.

We now have the nondimensional model

$$x_{t+1} = f(m_t)\, x_t = \frac{R_1\, x_t}{1 + a\, m_t}, \tag{2.7a}$$

$$y_{t+1} = g(n_t)\, y_t = \frac{R_2(1+b_1\, n_t)\, y_t}{1+b_2\, n_t^2}. \tag{2.7b}$$

This scaling creates a model with fewer parameters, simplifying analysis significantly.

2.3 Zero-growth isoclines and equilibria

To organize our analysis of the model given by eq. (2.7), we use zero-growth isoclines as our framework. A zero-growth isocline is the set of points at which the population density of a species is not changing. Thus, in our discrete-time system, the zero-growth isoclines of the pioneer or climax species occur when $x_{t+1} = x_t = x$ or $y_{t+1} = y_t = y$ respectively. Under these conditions, our total-density variables are $m_t = m = x + v_2\, y$ and $n_t = n = v_1\, x + y$. This substitution gives us the equations

$$x = f(m)\, x, \tag{2.8a}$$

$$y = g(n)\, y. \tag{2.8b}$$

We see that eq. (2.8a) is satisfied either when $x = 0$ or when $f(m) = 1$. By construction, there is one root of the pioneer species' fitness function at $f(m) = 1$. Thus, in total, there are two pioneer species zero-growth isoclines, the trivial one $x = 0$ and a nontrivial isocline where $f(m) = 1$ in the (x, y) plane. Both isoclines are linear.

Similarly, eq. (2.8b) has the solutions $y = 0$ or $g(n) = 1$. As the climax species' fitness function has two roots, we therefore have three zero-growth isoclines for the climax species. These isoclines are the trivial isocline $y = 0$ and two nontrivial isoclines from the solutions to $g(n) = 1$ in the (x, y) plane. The climax species' zero-growth isoclines are also linear.

Explicitly solving for the pioneer species' zero-growth isocline given by $f(m) = 1$ in terms of x and y yields the line

$$x = m^* - v_2\, y, \tag{2.9}$$

where

$$m^* = \frac{R_1 - 1}{a}. \tag{2.10}$$

Doing the same for the climax species' zero-growth isoclines given by $g(n) = 1$ gives us the two lines

$$y = n_1^* - v_1 x, \tag{2.11a}$$

$$y = n_2^* - v_1 x, \tag{2.11b}$$

where

$$n_{1,2}^* = \frac{R_2 b_1 \pm \sqrt{R_2^2 b_1^2 - 4 b_2 (1 - R_2)}}{2 b_2}, \tag{2.12}$$

with n_1^* corresponding to the negative square root and n_2^* the positive square root.

A fixed point of eq. (2.7) occurs at the intersection of two zero-growth isoclines, one isocline from each species, such that both populations are not changing over time. Given two zero-growth isoclines for the pioneer species and three for the climax species, there are six possible intersection points, and therefore six possible fixed-points. We will label these fixed points as $E_i = (x_i, y_i)$ where the subscript denotes the number of the fixed point instead of the time step.

Four of these six, including the origin, are boundary equilibria and always exist. These boundary, or exclusion, equilibria are

$$E_1 = (x_1, y_1) = (0, 0)\,, \tag{2.13}$$

the equilibrium at the origin where neither species persists,

$$E_2 = (x_2, y_2) = (m^*,\ 0)\,, \tag{2.14}$$

the equilibrium where the pioneer species persists and excludes the climax species,

$$E_3 = (x_3, y_3) = (0,\ n_1^*)\,, \tag{2.15}$$

the lower equilibrium on the y axis where the climax species persists but the pioneer species does not, and

$$E_4 = (x_4, y_4) = (0,\ n_2^*)\,, \tag{2.16}$$

the upper equilibrium on the y axis where the climax species persists. The boundary equilibria result from the intersection of a trivial isocline ($x = 0$ or $y = 0$) with a zero-growth isocline of the other species.

Up to two interior equilibria may also exist. An interior coexistence state occurs when the nontrivial pioneer species' isocline crosses one of the nontrivial climax species' isoclines, i.e., when both $f(m) = 1$ and $g(n) = 1$. These equilibria are

$$E_5 = (x_5, y_5) = \left(\frac{m^* - v_2 n_1^*}{1 - v_1 v_2}, \frac{n_1^* - v_1 m^*}{1 - v_1 v_2} \right), \tag{2.17}$$

which results from the pioneer species' nontrivial zero-growth isocline crossing the lower climax species' nontrivial zero-growth isocline, and

$$E_6 = (x_6, y_6) = \left(\frac{m^* - v_2 n_2^*}{1 - v_1 v_2}, \frac{n_2^* - v_1 m^*}{1 - v_1 v_2} \right), \tag{2.18}$$

where the pioneer species' nontrivial zero-growth isocline crosses the upper climax species' nontrivial zero-growth isocline.

In order to analyze the equilibria and understand the long-term dynamics of our model in eq. (2.7), we must consider the orientations of the isocline intersections that give rise to each equilibrium point. There are nine distinct geometric configurations of the zero-growth isoclines, some with interior equilibria and some without (fig. 2.2, fig. 2.3). The cases are distinguished from each other by restrictions on the parameter values. In particular, we fix all parameters but the relative competition-coefficients v_1 and v_2, and obtain limits on v_1 and v_2 in terms of the other parameters for each case.

In three cases, the nontrivial isoclines do not cross each other and so only the four boundary-equilibria E_{1-4} exist. These cases are shown in fig. 2.2. In the six remaining cases, the nontrivial pioneer species' isocline crosses one or both of the nontrivial climax species' isoclines. The six configurations with interior equilibria are presented in fig. 2.3.

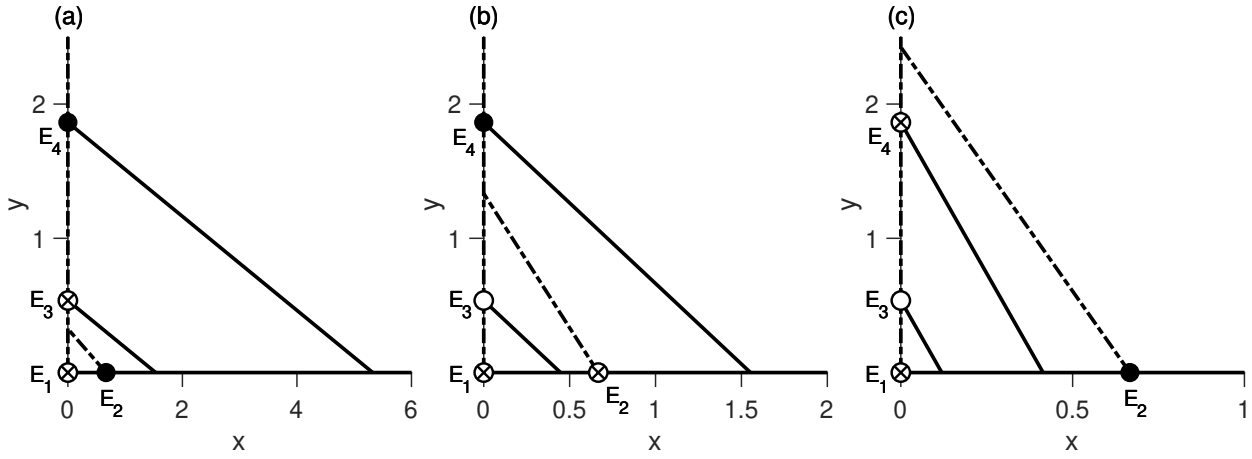

Fig. 2.2 Zero-growth isocline orientations and stabilities of fixed points for cases where only boundary fixed-points exist. The dashed-dotted lines are the pioneer species' zero-growth isoclines; solid lines (including $y = 0$) are the climax species' zero growth isoclines. Solid black circles indicate asymptotically-stable fixed-points. Circles with crosses are saddle points, while open circles signify other unstable fixed-points. For all cases, parameter values are $R_1 = 1.2$, $R_2 = 0.8$, $a = 0.3$, $b_1 = 0.6$, $b_2 = 0.2$. **a**, $v_1 = 0.35$, $v_2 = 2.05$. **b**, $v_1 = 1.2$, $v_2 = 0.5$. **c**, $v_1 = 4.5$, $v_2 = 0.275$.

2.4 Stability analysis

For all nine cases, we now determine the stabilities of the four to six equilibria that occur in each case. To assess stability of an equilibrium, we can examine the eigenvalues of the Jacobian of eq. (2.7) evaluated at that equilibrium. If both eigenvalues are less than one in magnitude, i.e., $|\lambda_1| < 1$ and $|\lambda_2| < 1$, we have asymptotic stability. The general form of the Jacobian matrix for eq. (2.7) is

$$\begin{aligned} J &= \begin{bmatrix} f(m_t) + x_t f'(m_t)\frac{\partial m}{\partial x} & x_t f'(m_t)\frac{\partial m}{\partial y} \\ y_t g'(n_t)\frac{\partial n}{\partial x} & g(n_t) + y_t g'(n_t)\frac{\partial n}{\partial y} \end{bmatrix} \\ &= \begin{bmatrix} f(m_t) + x_t f'(m_t) & v_2 x_t f'(m_t) \\ v_1 y_t g'(n_t) & g(n_t) + y_t g'(n_t) \end{bmatrix}. \end{aligned} \tag{2.19}$$

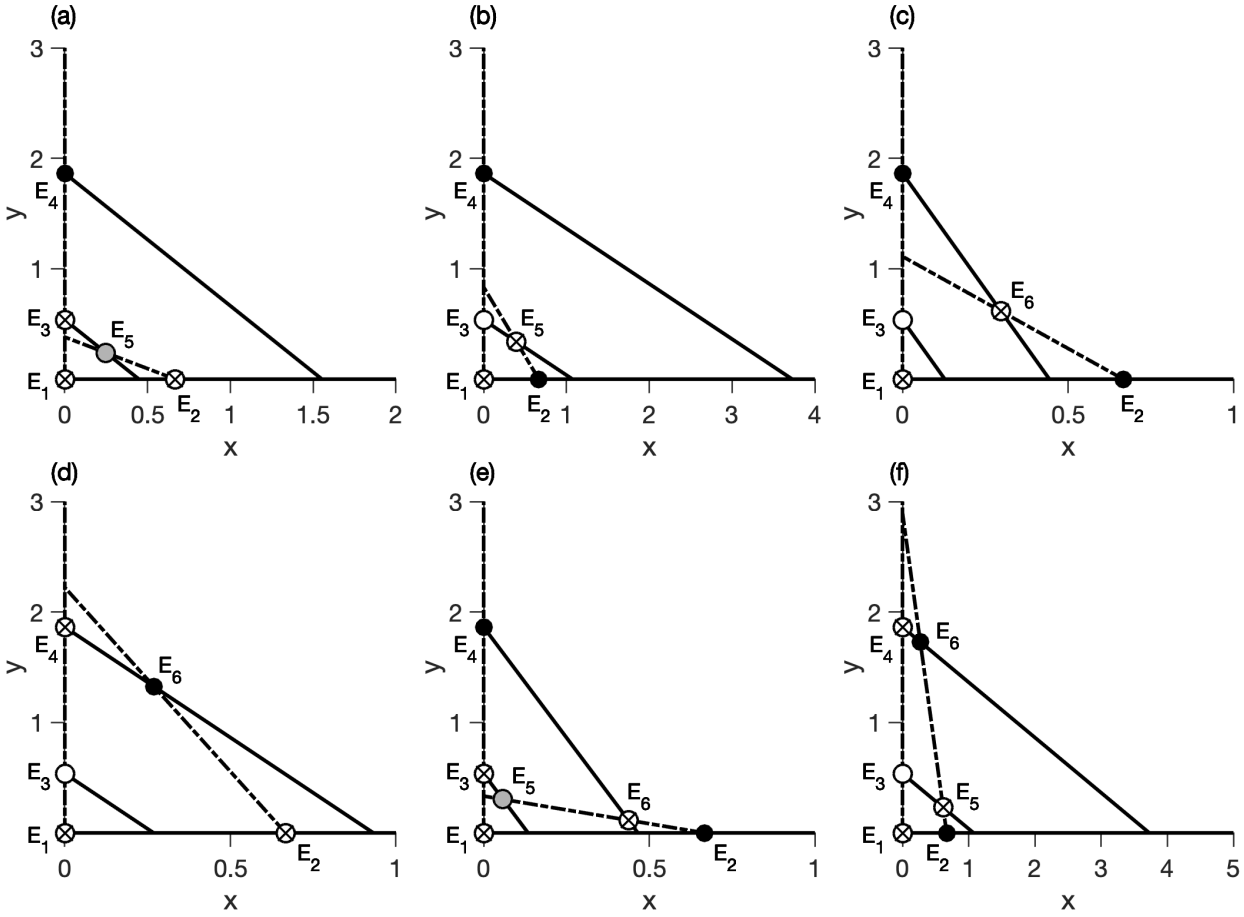

Fig. 2.3 Zero-growth isocline configurations and stabilities of equilibria for cases where interior equilibria occur. The dashed-dotted lines are the pioneer species' zero-growth isoclines; solid lines (including $y = 0$) are the climax species' zero growth isoclines. Parameter values for all cases are $R_1 = 1.2$, $R_2 = 0.8$, $a = 0.3$, $b_1 = 0.6$, $b_2 = 0.2$. The same classification system as in fig. 2.2 applies; gray shaded circles represent equilibria that undergo bifurcations. **a** and **b**, one interior equilibrium results from the crossing of the pioneer zero-growth isocline and the lower climax zero-growth isocline. **a**, $v_1 = 1.2$, $v_2 = 1.75$; **b**, $v_1 = 0.5$, $v_2 = 0.8$. **c** and **d**, one interior equilibrium results from crossing the upper climax zero-growth isocline. **c**, $v_1 = 4.2$, $v_2 = 0.6$; **d**, $v_1 = 2$, $v_2 = 0.3$. **e** and **f**, two interior equilibria occur. **e**, $v_1 = 4$, $v_2 = 2$; **f**, $v_1 = 0.5$, $v_2 = 0.23$.

2.4.1 *Boundary equilibria*

The eigenvalues of the Jacobian evaluated at each of the four boundary-equilibria are given in table 2.1. When $x = 0$ or $y = 0$, as in the boundary equilibria, an off-diagonal element of the Jacobian J is zero. This property allows us to simply read the eigenvalues off the diagonal of J. Additionally, for E_2 we may make the substitution $f(m) = 1$, as E_2 arises from the intersection of the isoclines $y = 0$ and $f(m) = 1$. Similarly, for $E_{3,4}$ we may say $g(n) = 1$, as these equilibria result from the intersections of $x = 0$ and the solutions to $g(n) = 1$.

The eigenvalues of all four boundary-equilibria are real for any parameter values. We can also prove that the eigenvalues for all boundary equilibria are positive in all nine cases (see appendix B.2 for details).

The origin is always a saddle point, as we assume $R_1 > 1$ and $R_2 < 1$. The stabilities of the other boundary equilibria are simple to determine in all cases by analyzing the eigenvalues. For E_{2-4}, we can establish whether λ_1 is greater or less than $+1$ by comparing where the non-zero component of the fixed point (i.e., x_2, y_3, or y_4) lands in relation to the root(s) where $g(v_1 x) = 1$ or $f(v_2 y) = 1$. This relation will be based on zero-growth isocline configuration for a given case. Similarly for E_{2-4}, λ_2 can be analyzed by determining the sign of the derivative of the fitness function evaluated at the given fixed-point. If the derivative is positive, $\lambda_2 > 1$, and if it is negative, $\lambda_2 < 1$.

For the three cases in which only boundary equilibria exist, this section completes our stability analysis. These three cases and the stabilities of their equilibria are shown in fig. 2.2. The stabilities of the boundary equilibria in the six cases where at least one interior fixed-point exists are shown in fig. 2.3. A full stability analysis for the boundary equilibria in all nine cases is presented in appendix B.2.

2.4.2 *Interior equilibria*

The remaining six cases, where at least one interior fixed-point occurs, are of significant interest given the potential for stable coexistence-states. We classify the stabilities of the boundary fixed-

Table 2.1 Boundary equilibria and their eigenvalues. Each equilibrium is generally represented by $E_i = (x_i, y_i)$.

Fixed point	Eigenvalues
E_1	$\lambda_1 = R_1, \lambda_2 = R_2$
E_2	$\lambda_1 = g(v_1 x_2), \lambda_2 = 1 + x_2 f'(x_2)$
E_3	$\lambda_1 = f(v_2 y_3), \lambda_2 = 1 + y_3 g'(y_3)$
E_4	$\lambda_1 = f(v_2 y_4), \lambda_2 = 1 + y_4 g'(y_4)$

points in these cases as above, by analyzing the magnitude of their eigenvalues. For the interior equilibria, however, analyzing the magnitude of the eigenvalues is difficult, as the form of the eigenvalues is complicated and the eigenvalues may be complex. Thus, to determine the stabilities of the interior equilibria, we use the Jury conditions [59] applied to the Jacobian of eq. (2.7) evaluated at each equilibrium point.

For this system, three Jury conditions together prove stability of an equilibrium, given by

$$1 - \tau + \Delta > 0, \tag{2.20a}$$

$$1 + \tau + \Delta > 0, \tag{2.20b}$$

$$\Delta < 1, \tag{2.20c}$$

where τ and Δ are the trace and determinant of the Jacobian J. The first condition ensures there are no eigenvalues greater than $+1$, the second that there are no eigenvalues less than -1. The third condition guarantees that no complex eigenvalues lie outside the unit circle.

Violating any of the Jury conditions as parameter values change will result in the equilibrium point changing stability via a local bifurcation [149]. Violating the first Jury condition leads to a transcritical bifurcation. Violating the second Jury condition results in a flip, or period-doubling, bifurcation. If the third condition is violated, a Neimark–Sacker bifurcation will occur. This bifurcation is the discrete-time analog of a Hopf bifurcation. By testing the Jury conditions on Jacobian

(2.19) evaluated at the interior equilibrium-point(s), for all six cases with coexistence states, we classify the stabilities of the interior equilibria as shown in fig. 2.3.

For every case, the first Jury condition is either always satisfied or never satisfied for any parameter values within the case's bounds. Thus, there are no transcritical bifurcations for either coexistence fixed-point while that fixed point remains within the interior of the first quadrant. However, the interior fixed-point will shift toward the x axis if v_1 is varied and the y axis if v_2 is varied. There are critical v_1 and v_2 values that distinguish each geometric case from the others, and precisely at these critical values the interior fixed-point hits one of the axes, colliding with one of the boundary equilibria in the process. Therefore, transcritical bifurcations do occur as the interior fixed-point passes through the boundary equilibria, corresponding to a change in geometric case. This bifurcation results in the coexistence equilibria exiting the first quadrant, leading to negative population-densities.

The results of the transcritical bifurcations that occur are evident from fig. 2.2 and fig. 2.3. Compare, for example, fig. 2.2c and fig. 2.3c. As v_2 decreases, the pioneer species' isocline (dashed-dotted line) in fig. 2.3c shifts, its y-intercept increasing, and the interior equilibrium E_5 moves toward the y axis. Eventually, E_5 collides with the y axis at E_4, and the equilibria exchange stabilities. The previously stable equilibrium E_4 becomes a saddle point, and E_5 passes out of the first quadrant as an asymptotically-stable fixed-point. As v_2 decreases further, the pioneer species' isocline lies fully above the two climax species' isoclines, and we are now in the case shown in fig. 2.2c, where we see that E_4 is indeed a saddle point and there is no interior fixed-point in the first quadrant.

The second Jury condition is never violated, and so there are no period-doubling bifurcations. More precisely, we can prove, through use of Descartes' Rule of Signs [29], that all real eigenvalues of Jacobian (2.19) are positive for both interior equilibria in all cases (see section C.2.3). This property rules out violation of the second Jury condition. This result is in contrast to several other studies that demonstrated period-doubling bifurcations in their discrete-time pioneer–climax

models [123, 119, 124, 58].

For all four cases in which equilibrium E_6 exists (fig. 2.3c, 2.3d, 2.3e, and 2.3f), we can prove that all eigenvalues of the Jacobian evaluated at E_6 are strictly real. We can prove the same for two of the cases with equilibrium E_5 (fig. 2.3b and 2.3f). Thus, we do not analyze the third Jury condition at all for E_6, nor for E_5 in two cases, as this condition applies to complex eigenvalues. We determine stabilities of the relevant interior equilibria in these cases by again using Descartes' Rule of Signs [29], to find the number of eigenvalues that are above and below $+1$. As we also know that our real roots are positive, this information is all we require to classify the stabilities of the interior fixed-point(s) in these cases.

In the remaining two cases in which E_5 occurs, one with only E_5 (fig. 2.3a) and one with both interior equilibria (fig. 2.3e), we cannot show that the eigenvalues at E_5 are always real. Numerically, we find that the eigenvalues may be real or complex for different parameter values. Thus, for these two cases we fix R_1, R_2, a, b_1, and b_2 and analyze the third Jury condition to find a region in the (v_1, v_2) plane for which equilibrium E_5 is asymptotically stable. The parameters v_1 and v_2 were selected to highlight how relative competition-coefficients affect stability. Competition is the main underlying factor influencing the density of both pioneer and climax species, as seen in the construction of our model. Therefore, the competition parameters were a natural choice to analyze.

The determinant of the Jacobian evaluated at E_5 is

$$\Delta = \big(1 + x_5 f'(m)\big)\big(1 + y_5 g'(n)\big) - v_1 v_2 x_5 y_5 f'(m) g'(n), \tag{2.21}$$

with $m = x_5 + v_2 y_5$ and $n = v_1 x_5 + y_5$. After substituting in the explicit forms of the equilibrium and derivatives, it is possible to solve the equation $\Delta = 1$ for v_2 as a function of v_1 (or vice versa). Thus, for both cases we can get a curve for the third Jury condition that defines the region of stability for E_5 in the (v_1, v_2) plane. These curves are shown in fig. 2.4. Above and to the left of the solid curve, E_5 is asymptotically stable. Crossing the solid curve violates the third Jury condition and destabilizes E_5 via a Neimark–Sacker bifurcation. For the explicit form of the curves for the third

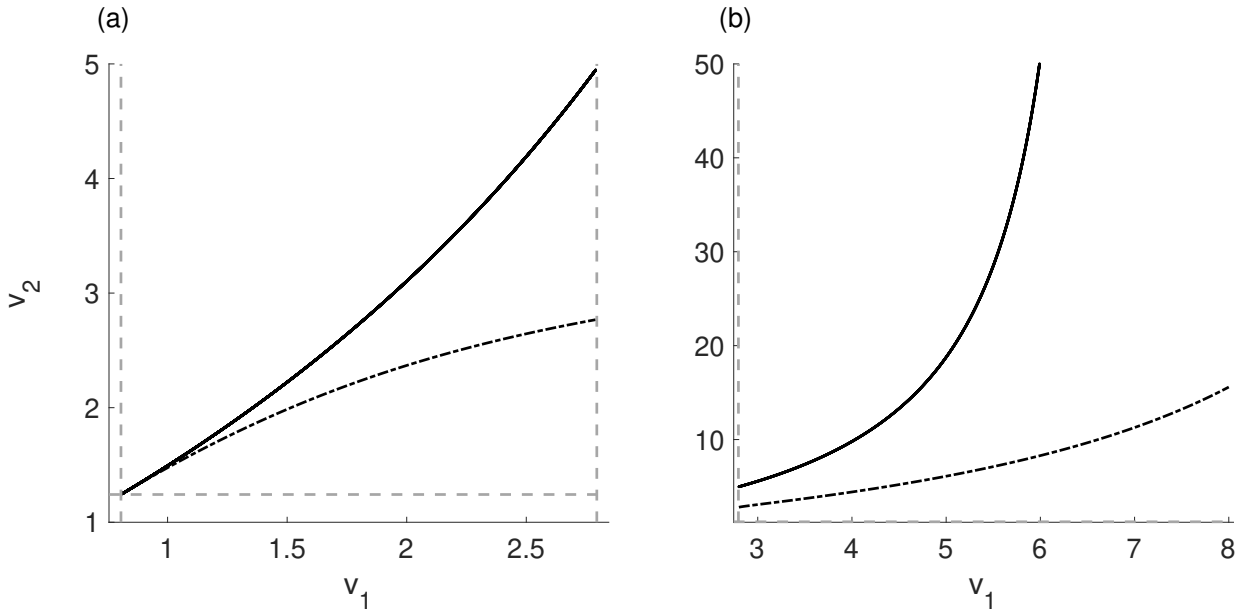

Fig. 2.4 Stability region for equilibrium E_5, defined by the curves in (v_1, v_2) parameter space where bifurcations occur. In both cases, E_5 is stable for parameter values above and to the left of the solid curve given by $\Delta = 1$; crossing this curve results in a loss of stability via a Neimark–Sacker bifurcation and the birth of an invariant circle. The lower dashed-dotted curves are the boundaries at which the global bifurcations occur; crossing the dashed-dotted curve results in the abrupt disappearance of the invariant circle. **a**, the first case corresponding to fig. 2.3a with a heteroclinic bifurcation. The global-bifurcation curve was found by using the bisection method to calculate, for a given v_1, the v_2 value for which a trajectory starting on the unstable manifold of E_2 ended at, or very near to, E_3, such that the unstable manifold of E_2 connected with the stable manifold of E_3. **b**, the second case corresponding to fig. 2.3e with a homoclinic bifurcation. The global-bifurcation curve for this case was found by using the bisection method to determine, for a given v_1, the v_2 value for which a trajectory starting on the unstable manifold of E_6 returned to E_6, such that the unstable and stable manifolds of E_6 connected to form a homoclinic connection. The dashed gray lines in each panel indicate the boundaries on v_1 and v_2 such that we are in the appropriate geometric case, i.e., that the isoclines intersect in the appropriate configuration. Parameter values for both cases are $R_1 = 1.2$, $R_2 = 0.8$, $a = 0.3$, $b_1 = 0.6$, $b_2 = 0.2$.

Jury condition, as well as a full stability analysis of the interior fixed-points, see appendix C.2.

In all, four of the six cases with interior equilibria have an asymptotically-stable coexistence-state for at least some parameter values. In two of these cases, equilibrium E_6 is always asymptoti-

cally stable. The other two have limited parameter regions where equilibrium E_5 is asymptotically stable (fig. 2.4). Even after E_5 has become unstable in these two cases, an attracting invariant circle is born from the Neimark–Sacker bifurcation that destabilized E_5. We will now examine this local bifurcation in more detail.

2.5 Neimark–Sacker bifurcation

In two geometric cases we violate the third Jury condition for equilibrium E_5 by having a pair of complex-conjugate eigenvalues exit the unit circle. These cases correspond to fig. 2.3a and 2.3e. For the remainder of this section and the next (section 2.6), we will refer to them as the first case and the second case.

In both cases, for parameter values above and to the left of the curve $\Delta = 1$, equilibrium E_5 is asymptotically stable (fig. 2.4). As v_2 decreases and crosses this boundary, the equilibrium point loses stability via a Neimark–Sacker bifurcation and an attracting quasiperiodic solution, commonly known as an invariant circle, emerges. As v_2 continues to decrease, the invariant circle grows larger. The attracting invariant circle for a variety of v_2 values can be seen in fig. 2.5 for the first case and in fig. 2.6 for the second case.

As we have noted, loss of stability via a Neimark–Sacker bifurcation for fixed point E_5 occurs as the relative competition-coefficient v_2 decreases for fixed v_1. Thus, as intraspecific competition in the climax species grows stronger relative to the competitive effect of the climax species on the pioneer species, the equilibrium destabilizes. Equivalently, if v_2 were fixed, the equilibrium loses stability as v_1 increases. Biologically, this situation corresponds to the competitive effect of the pioneer species on the climax species increasing relative to the competitive effect of the pioneer species on itself. In either context, v_1 increasing or v_2 decreasing, the fixed point E_5 is destabilized when a species' competitive effect on the climax species grows stronger relative to its competitive effect on the pioneer species. In place of the fixed point, an attracting quasiperiodic solution arises, resulting in stable population fluctuations.

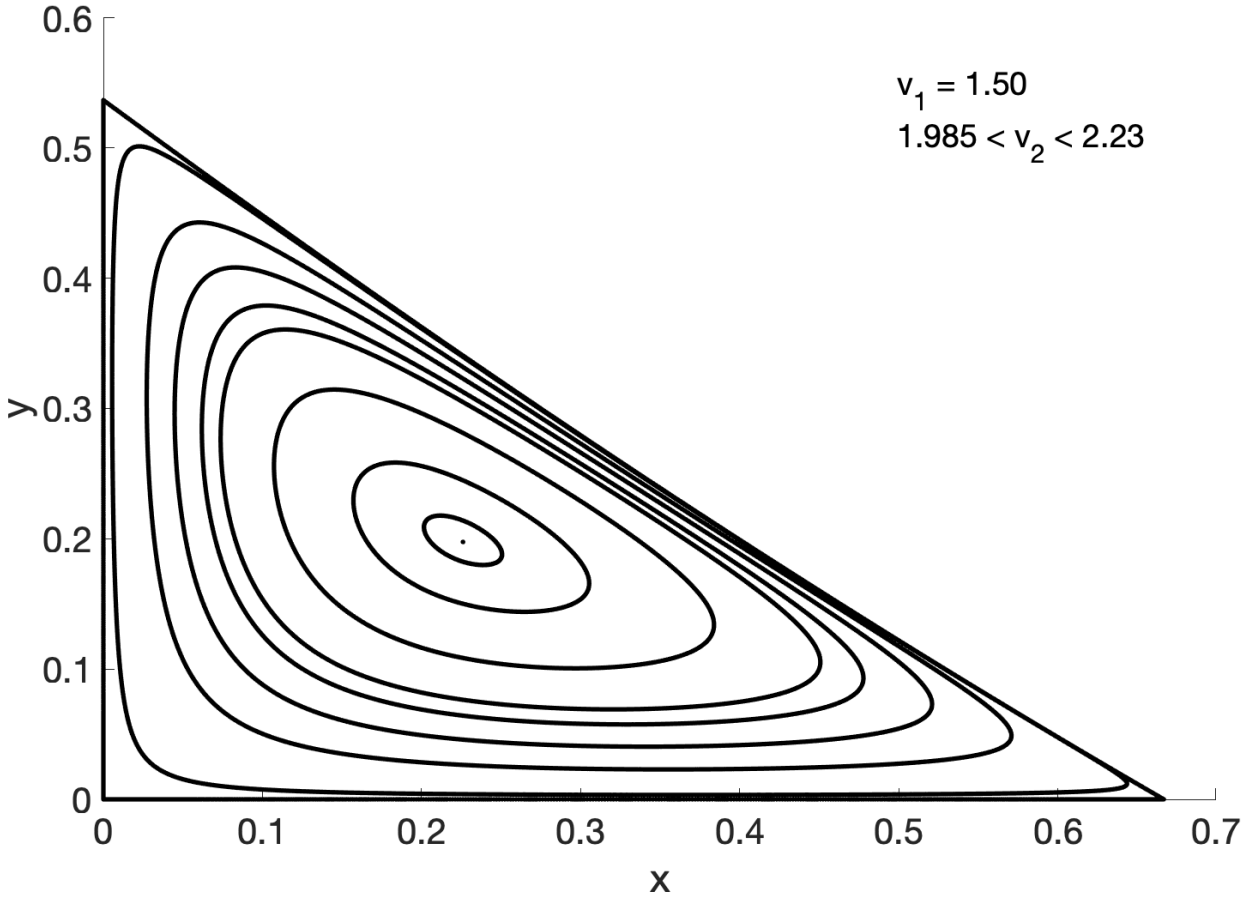

Fig. 2.5 Growth of the invariant circle as v_2 decreases from 2.23 to just above 1.985 in the first case with a Neimark–Sacker bifurcation. The point in the middle of the invariant circles is E_5 for $v_2 = 2.23$, when E_5 is asymptotically stable. We ran the system for 50,000 iterations; the final 15,000 iterations were plotted for ten v_2 values. Parameter values are $R_1 = 1.2$, $R_2 = 0.8$, $a = 0.3$, $b_1 = 0.6$, $b_2 = 0.2$.

To fully characterize the Neimark–Sacker bifurcation, we must consider the possibility of resonance. Resonance cases occur when the complex-conjugate eigenvalues λ, $\overline{\lambda}$ of our Jacobian exit the unit circle through a root of unity such that $\lambda = e^{2\pi ip/q}$ and $\overline{\lambda} = e^{-2\pi ip/q}$, where p and q are both positive integers and p/q is known as the rotation number [6, 149]. This phenomenon is called strong resonance if $q \leq 4$ and weak resonance for $q \geq 5$ [149, 70]. The bifurcation that

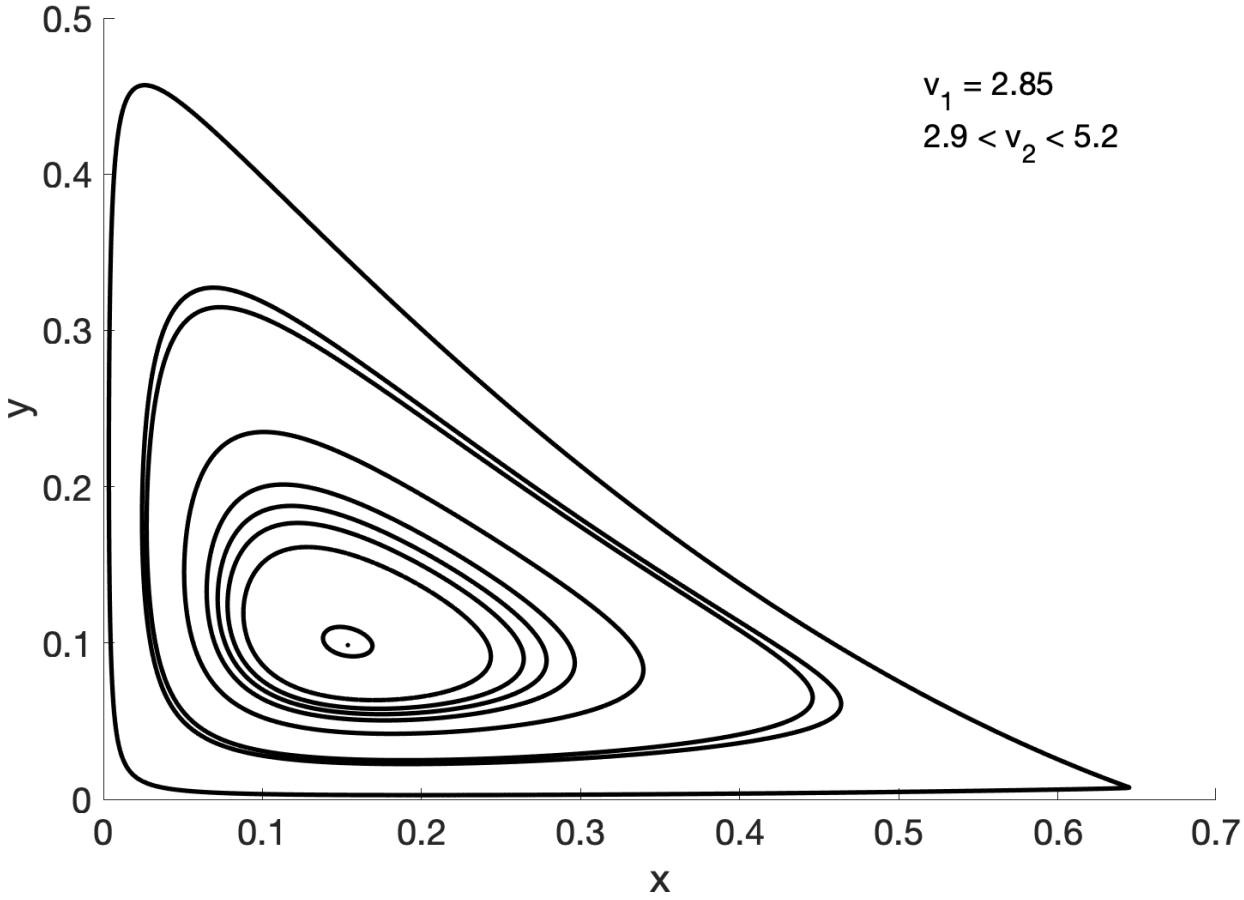

Fig. 2.6 Growth of the invariant circle in the second case as v_2 decreases from 5.2 to 2.9. The single point in the middle of the invariant circles is E_5 for $v_2 = 5.2$, when E_5 is asymptotically stable. The system was run for 1,000,000 iterations; the final 200,000 iterations were plotted for ten v_2 values. This number of iterations was necessary to fill in the invariant circle for some v_2 values for which the system had nearly-rational rotation numbers. Other parameter values are $R_1 = 1.2$, $R_2 = 0.8$, $a = 0.3$, $b_1 = 0.6$, $b_2 = 0.2$.

occurs in a resonance case does not lead to the birth of an invariant circle; phase-locked periodic solutions or more complicated behaviors arise instead [5, 70, 68].

In both cases with the Neimark–Sacker bifurcation, the eigenvalues of the Jacobian are precisely on the unit circle for any (v_1, v_2) pair that lies on the curve $\Delta = 1$ (fig. 2.4). Thus, if the eigenvalues are located at roots of unity for any such (v_1, v_2) pair, resonance occurs for those pa-

rameter values. To check for cases of resonance, we numerically calculate the eigenvalues of the Jacobian for all (v_1, v_2) pairs on the curve $\Delta = 1$, i.e., parameters for which the eigenvalues lie on the unit circle, and isolate the rotation number p/q. If the rotation number is rational, we have a p/q resonance [6].

In both cases with a Neimark–Sacker bifurcation, the rotation numbers as our eigenvalues pass through the unit circle are very small. This small size precludes the possibility of strong resonance, as the smallest rotation number that would lead to strong resonance is $p/q = 1/4$.

There is no solid evidence for weak resonance either, although this absence could be due to numerical inaccuracy in calculating the rotation numbers. For some parameter values, particularly in the second case with a Neimark–Sacker bifurcation, it takes many thousands of iterations to densely fill the invariant circle. This situation indicates we may have rotation numbers that are very close to, but not quite, rational. Weak resonance cases give rise to phase-locked periodic orbits, but there is no evidence of periodic solutions in a bifurcation diagram. Instead, the bifurcation diagram shows only densely filled invariant circles or fixed points (fig. 2.7, fig. 2.8). Thus, if phase-locking occurs, it is likely for an orbit of extremely high period that is unnoticeable in numerical calculations.

In a discrete-time system, it is not uncommon after a Neimark–Sacker bifurcation for the invariant circle to eventually deform or for further bifurcations to occur, leading to a strange attractor [27, 6, 121, 97, 122]. Such behavior has been shown specifically in pioneer–climax discrete-time models [121, 122], as well as in a continuous-time pioneer–climax model [118]. We do not observe such behavior here. Instead, in both cases with a Neimark–Sacker bifurcation, a global bifurcation occurs as the invariant circle grows larger. We now turn to investigate these global bifurcations.

2.6 Global bifurcations

As can be seen in fig. 2.5 and fig. 2.6, in both cases with a Neimark–Sacker bifurcation the invariant circle grows closer and closer to the axes as v_2 decreases. Additionally, the invariant circle appears

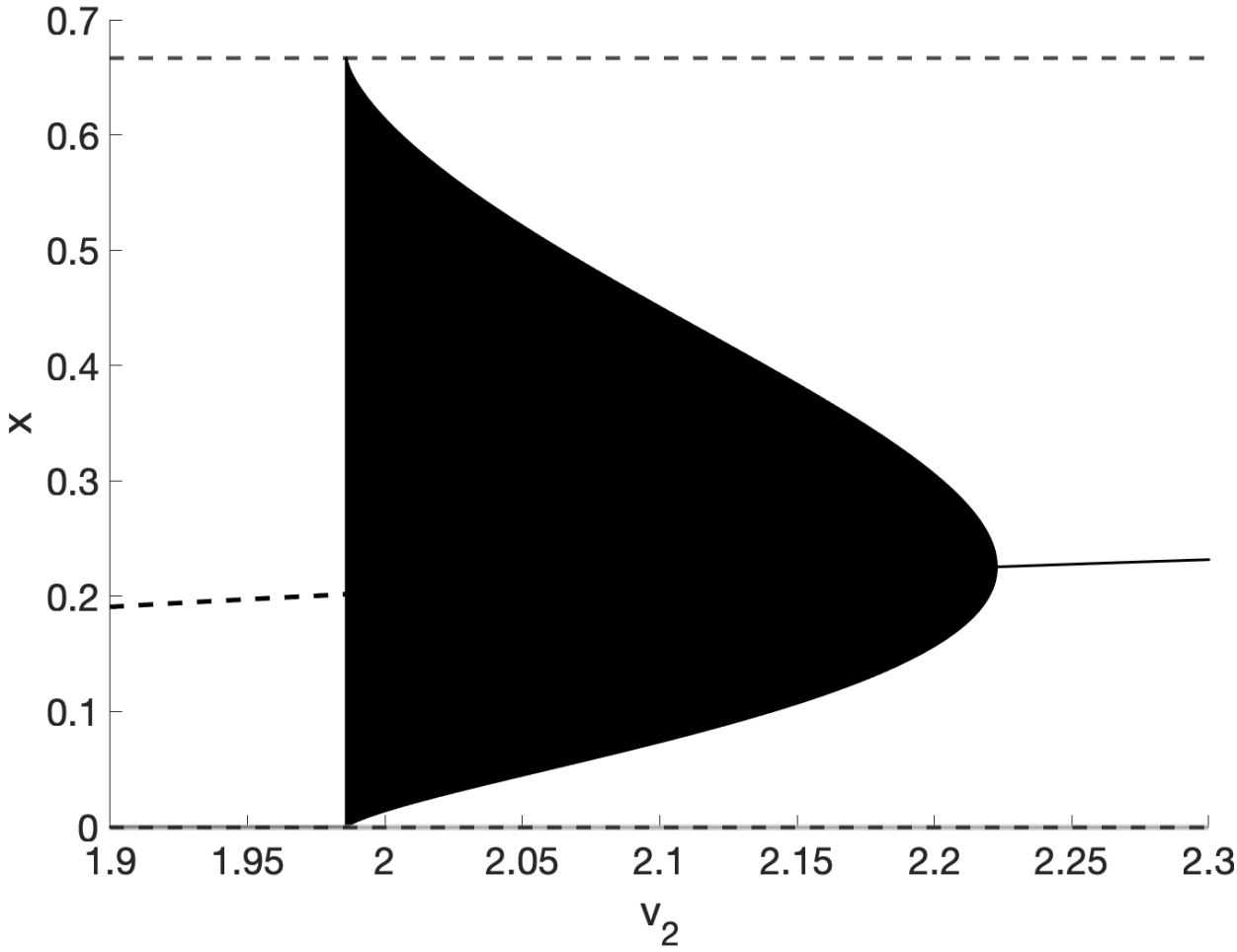

Fig. 2.7 Bifurcation diagram for the first case with bifurcations, showing the x coordinates of the attractors and other fixed points. Dashed lines represent saddle points or other unstable fixed-points; solid lines represent asymptotically-stable fixed-points. The black dashed line on top of the gray solid line at $x = 0$ is included to show there are both stable and unstable fixed-points with coordinate $x = 0$. As v_2 decreases, we see the birth of an invariant circle due to a Neimark–Sacker bifurcation. All x values on the invariant circle are mapped, such that for a single v_2 value there are many values of x. The invariant circle grows as v_2 decreases further until its sudden disappearance in a global bifurcation as the invariant circle runs into a heteroclinic cycle between the three saddle points of this case. Parameter values are $R_1 = 1.2$, $R_2 = 0.8$, $a = 0.3$, $b_1 = 0.6$, $b_2 = 0.2$, $v_1 = 1.5$.

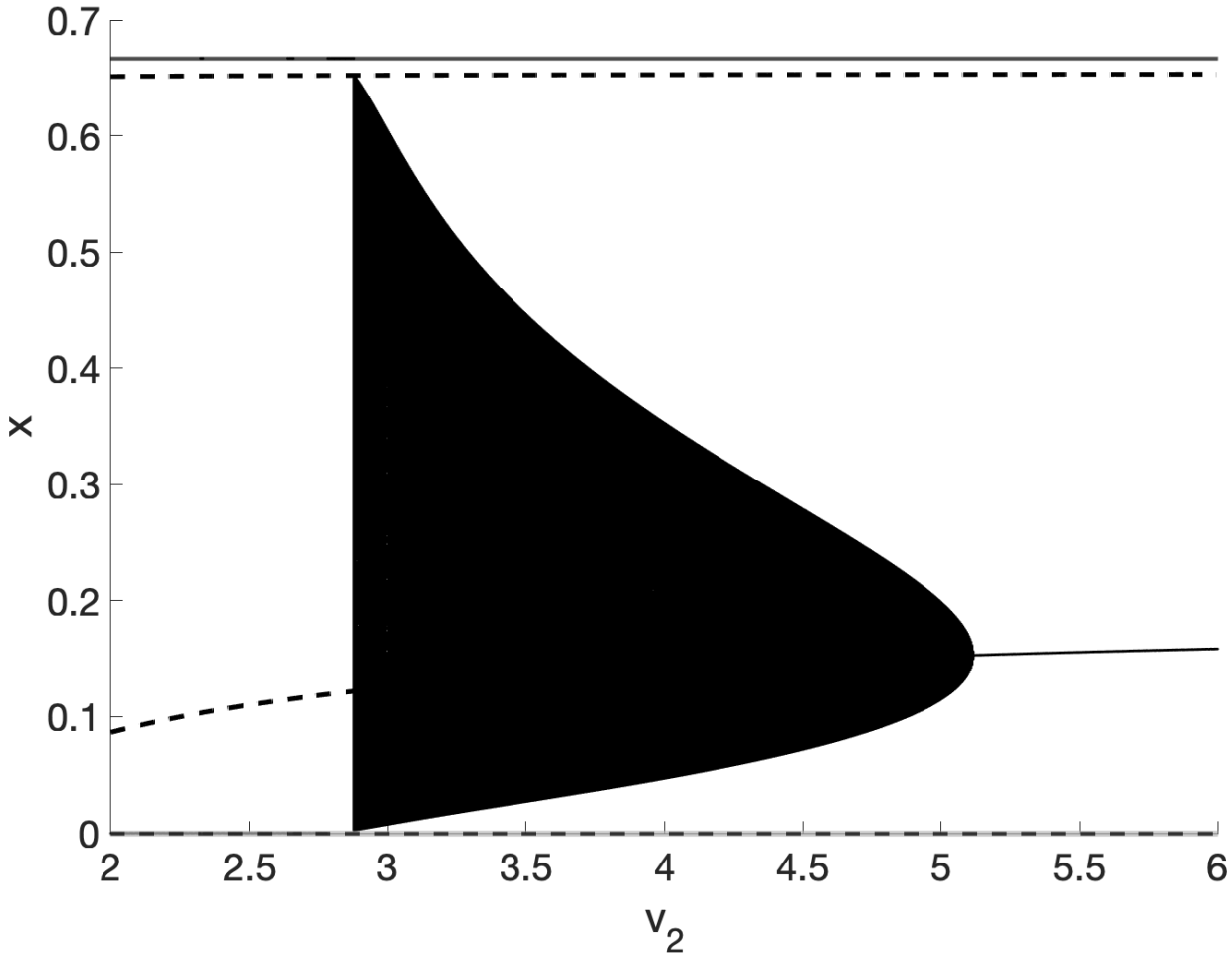

Fig. 2.8 Bifurcation diagram of the second case showing the x coordinates of the attractors and other fixed points. Dashed lines show saddle points or other unstable fixed-points; solid lines represent asymptotically-stable fixed-points. The black dashed line on top of the solid gray line at $x = 0$ shows there are both stable and unstable fixed-points at $x = 0$. As with the first case, as v_2 decreases an invariant circle is born via a Neimark–Sacker bifurcation, eventually abruptly vanishing in a global bifurcation. Parameter values are $R_1 = 1.2$, $R_2 = 0.8$, $a = 0.3$, $b_1 = 0.6$, $b_2 = 0.2$, $v_1 = 2.85$.

to approach some limiting curve with negative slope within the first quadrant. For a critical v_2 value, the invariant circle abruptly vanishes, leaving no attractor in the interior at all, in what is known as a dangerous global bifurcation [135]. The mechanism by which this disappearance of

the invariant circle occurs is different in the two bifurcation cases, and we have two types of global bifurcation resulting in the blue-sky disappearance of an invariant circle.

2.6.1 Heteroclinic bifurcation

Recall that in the first case (fig. 2.3a, fig. 2.5), three saddle points are on the boundaries. These saddle points occur at E_1 at the origin, E_2 on the x-axis, and E_3, the lower fixed-point on the y-axis. In this case, for a critical v_2 value, a heteroclinic cycle forms between the three saddle points. The invariant circle runs into the heteroclinic cycle and instantaneously vanishes. Thus, we have the blue-sky disappearance of an invariant circle due to a heteroclinic bifurcation.

The heteroclinic cycle that forms is relatively simple and is shown in fig. 2.9b. The y axis is the unstable manifold of E_3 and the stable manifold of E_1, so a heteroclinic connection is formed moving from E_3 into E_1 along the y axis. Similarly, the x axis is the unstable manifold of E_1 and the stable manifold of E_2; so the portion of the x axis between E_1 and E_2 forms a heteroclinic connection as well. Finally, the unstable manifold of E_2 connects with the stable manifold of E_3, finishing off a triangular heteroclinic cycle between E_1, E_2 and E_3. Prior to and after the global bifurcation, the invariant manifolds of E_2 and E_3 do not intersect (fig. 2.9a, 2.9c).

Numerically, this last heteroclinic connection between E_2 and E_3 appears to be a linear or near-linear connection (fig. 2.9), suggesting these manifolds may coincide, or at the very least are nearly indistinguishable from one another. Kim and Marlin [62] found in a differential-equation pioneer–climax model that, for the same geometric zero-growth isocline configuration, there was a critical parameter value for which the unstable manifold of E_2 and the stable manifold of E_3 coincided. While their continuous-time model was different from our discrete-time model, it offers support to the idea that these manifolds may indeed coincide; however, we leave an analytic proof for the future.

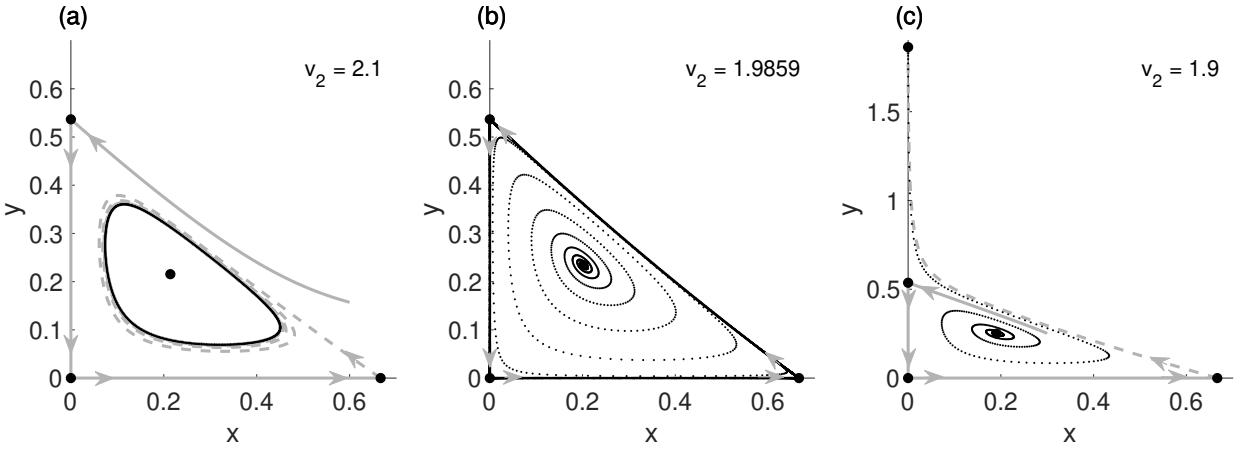

Fig. 2.9 Behavior of the system before, at, and after the heteroclinic bifurcation in the first case with bifurcations. Solid gray lines are stable manifolds, dashed gray lines are unstable manifolds. The axes are also invariant manifolds and form heteroclinic connections between E_1 and E_2 on the x axis and E_1 and E_3 on the y axis. Large black points are equilibria, trajectories of the system with an initial condition near E_5 are shown with smaller black points. The arrows indicate the direction of travel along the manifold. **a**, prior to the global bifurcation, the unstable manifold from E_2 passes below the stable manifold of E_3 and winds onto the attracting invariant circle. **b**, at the point of global bifurcation, a heteroclinic cycle forms and the unstable and stable manifolds of E_2 and E_3 link together to complete the cycle. **c**, after the global bifurcation, the heteroclinic connection is broken and no stable coexistence-state exists. Almost all trajectories go to E_4 on the y axis, save for solutions starting on the stable manifold of E_3 or on the axes between E_1 and E_2 or between E_1 and E_3. Parameter values are $R_1 = 1.2$, $R_2 = 0.8$, $a = 0.3$, $b_1 = 0.6$, $b_2 = 0.2$, $v_1 = 1.5$.

2.6.2 Homoclinic bifurcation

Three saddle points are also in the second case (fig. 2.3e, fig. 2.6), two on the boundaries at E_1 (the origin) and E_3 (the y-axis) and one just off of the x-axis at E_6. However, a heteroclinic cycle does not form between these three saddle points as in the first case; a homoclinic connection forms between the stable and unstable manifolds of the coexistence equilibrium E_6 instead (fig. 2.10b, fig. 2.11). The invariant circle runs into the homoclinic connection for a particular v_2 value, resulting in the blue-sky disappearance of an invariant circle due to a homoclinic bifurcation.

The stable manifold of the interior equilibrium E_6 winds very close to the x and y axes but never

intersects either axis, precluding a heteroclinic connection between E_6 and the origin (fig. 2.11). Nevertheless, due to this closeness, we see the invariant circle grow very near to both axes. The invariant circle does not come close to the lower equilibrium on the y axis E_3, however, even very close to the point at which the global bifurcation occurs. This distance can be seen by noting that the maximum height, or y coordinate, of the largest invariant circle is significantly lower in fig. 2.6 than in fig. 2.5. In addition to the fact that the manifolds of E_6 do not intersect the manifolds of E_1 or E_3, this behavior is further indicative of the differences between the heteroclinic cycle of the first case and the homoclinic connection in this second case.

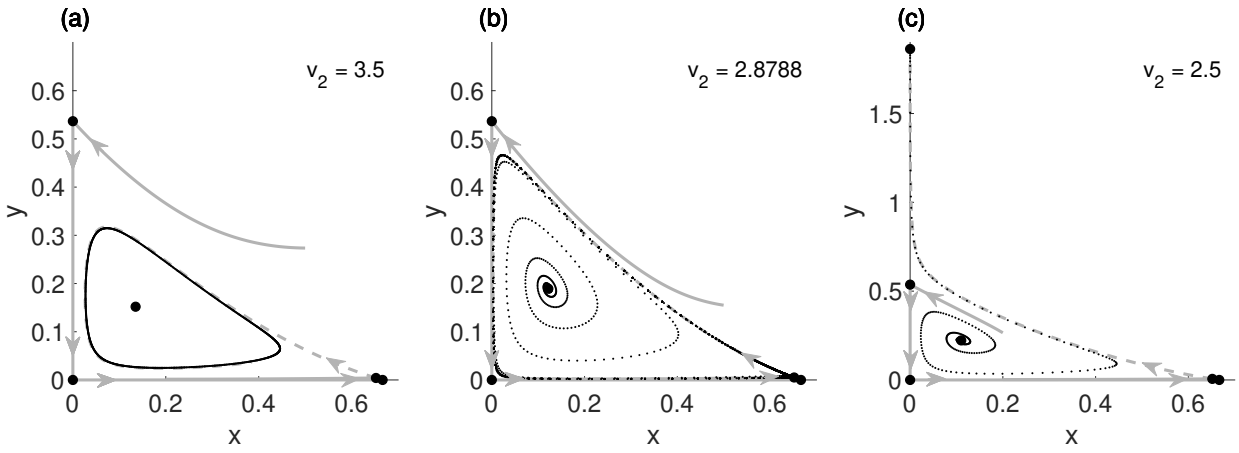

Fig. 2.10 Behavior of the system before, at, and after the homoclinic bifurcation in the second case with bifurcations. Solid gray lines are stable manifolds, dashed gray lines are unstable manifolds. The axes are again invariant manifolds with heteroclinic connections between E_1 and E_2 on the x axis and E_1 and E_3 on the y axis. Large black points represent equilibria, trajectories of the system starting near E_5 are shown with smaller black points. Arrows indicate direction of travel along the manifolds. **a**, prior to the global bifurcation, the unstable manifold from interior equilibrium E_6 passes below the stable manifold from E_3 on the y axis and winds onto the attracting invariant circle. **b**, at the point of global bifurcation, a homoclinic connection forms between the stable and unstable manifolds of E_6, passing very close to the invariant manifolds on the axes. **c**, after the global bifurcation, no stable coexistence-state exists and the homoclinic connection has been broken. Almost all trajectories go either to E_4 on the y axis (shown here) or E_2 on the x axis. Parameter values are $R_1 = 1.2$, $R_2 = 0.8$, $a = 0.3$, $b_1 = 0.6$, $b_2 = 0.2$, $v_1 = 2.85$.

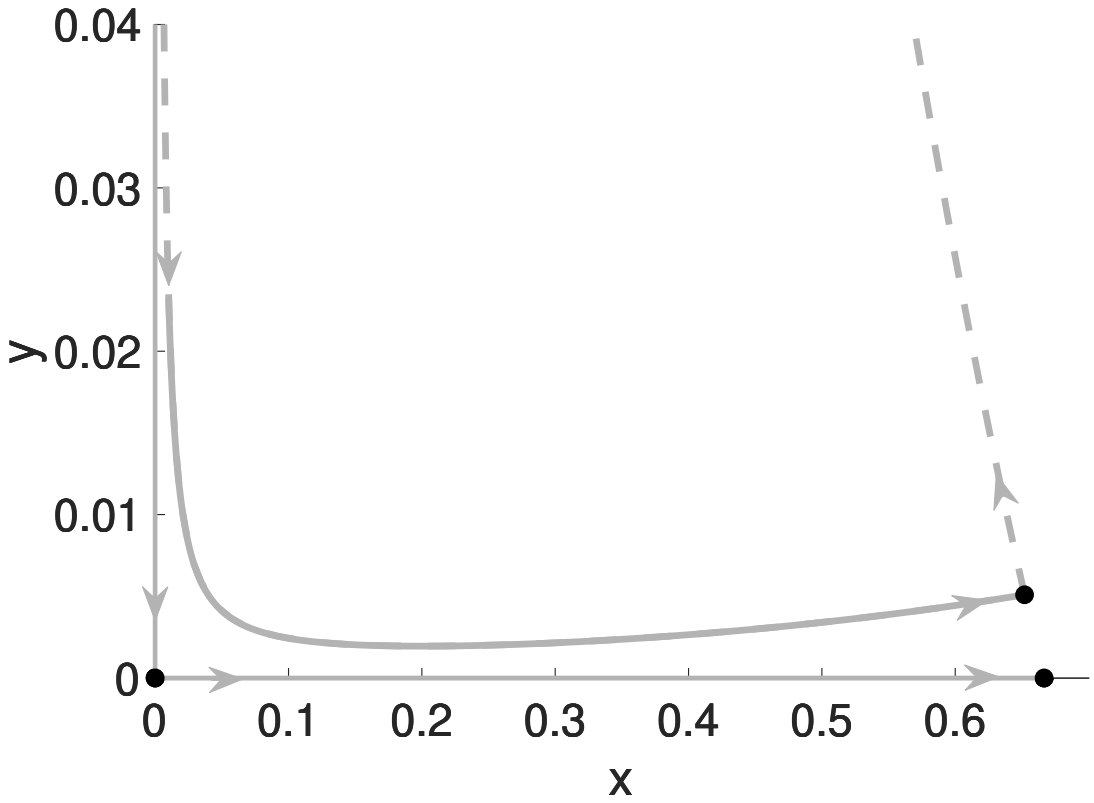

Fig. 2.11 A magnified view of the lower part of the homoclinic connection in the second case with bifurcations. Here, the loop between the stable and unstable manifolds of E_6 is clear, and we more easily see that the invariant manifolds of E_6 do not intersect the manifolds on the axes of E_1 or E_2. Solid gray lines are stable manifolds, dashed gray lines are unstable manifolds, and points are equilibria. Arrows indicate direction of travel along the manifolds. Parameter values are $R_1 = 1.2$, $R_2 = 0.8$, $a = 0.3$, $b_1 = 0.6$, $b_2 = 0.2$, $v_1 = 2.85$, and $v_2 = 2.878800266186866$.

2.6.3 Behavior near the global bifurcations

In both cases, as v_2 decreases the invariant circle grows larger until it is pushed up against the heteroclinic cycle or homoclinic connection (fig. 2.5, fig. 2.6). At a critical v_2 value, the circle can grow no more, constrained by the invariant manifolds that have formed a heteroclinic cycle or homoclinic connection (fig. 2.9b, fig. 2.10b), and the invariant circle vanishes into thin air. The disappearance of the invariant circle corresponds to crossing the dashed-dotted line from above in

fig. 2.4. We see in fig. 2.4 that for fixed v_1 an invariant circle exists only in the space between the solid line, when the invariant circle appears due to a Neimark–Sacker bifurcation, and the dashed-dotted line, which shows the point of global bifurcation when the invariant circle vanishes.

The disappearance of the invariant circle due to a global bifurcation is starkly apparent in a bifurcation diagram (fig. 2.7, fig. 2.8). In both cases, we see the edges of the invariant circle, represented by the minimum and maximum x-values of the invariant circle, run into the saddle point at E_2 or E_6, depending on the case, and the two saddle points E_1 and E_3 with coordinate $x = 0$.

The blue-sky disappearance of an invariant circle due to a heteroclinic bifurcation is a global bifurcation not previously observed in a discrete-time pioneer–climax model, though Kim and Marlin [62] noted this bifurcation for the first case in continuous time. This research is, however, the first time that anyone has observed the disappearance of an invariant circle due to a homoclinic bifurcation in a pioneer–climax system, whether in discrete or continuous time.

We have already noted that in both cases with bifurcations, E_5 was destabilized and an attracting quasiperiodic solution arose as a species' competitive effect on the climax species grew stronger relative to its effect on the pioneer species. Now, we see that if this competitive effect on the climax species becomes stronger still, the attracting orbit vanishes entirely, leaving no stable coexistence state at all. This result is, perhaps, a ready conclusion to draw from observing the growth of the invariant circle. As v_2 decreases and competitive effect on the climax species becomes stronger, populations are regularly driven very close to either $x = 0$ or $y = 0$, such that a small stochastic effect on the populations may easily drive one species to extinction.

2.7 Discussion

As climate change affects ecosystems, causing effects from range shifts to increased habitat-disturbances, successional communities are likely to become more common [72, 19, 117]. In this chapter, we introduced a simple discrete-time pioneer–climax model where the species' inter-

action dynamics are built upon principles of ecological succession. We characterized the long-term dynamics of the model in the first in-depth analytical stability analysis of a discrete-time pioneer–climax system, and the stability results were supported by numerical simulations. Our analysis is organized around nine geometric cases that are distinguished by different parameter regimes, corresponding to limits on the relative competition-coefficients v_1 and v_2. The model results in a diverse set of long-term behaviors among the nine different cases, some of which are novel to a discrete-time pioneer–climax model. These behaviors were robust to other parameter sets.

Of these nine geometric configurations, six cases have an asymptotically-stable climax-exclusion state in which the pioneer survives (fig. 2.2a, 2.2c, fig. 2.3b, 2.3c, 2.3e, and 2.3f). For a long time, researchers assumed the asymptotic result of an undisturbed pioneer–climax system was pioneer exclusion [46, 120]. Many pioneer–climax models have since shown that pioneer exclusion is not the only possible long-term behavior, but this analysis was done primarily through proofs of the stabilities of coexistence states (e.g., [122, 131, 62]). The existence of asymptotically-stable climax-exclusion states was largely ignored in these analyses.

It is interesting, however, that in a majority of the nine parameter regimes the system does indeed have an asymptotically-stable climax-exclusion state. This result tells us that even in an undisturbed environment, under some (perhaps limited) circumstances the pioneer species could not just coexist with the climax species, but it could even outcompete the climax species. The only cases in which a stable pioneer-only state was not present was for moderate values of v_1, i.e., when the effect of the pioneer on the climax species is relatively close to the effect of the pioneer species on itself.

Five of the six cases with an asymptotically-stable climax-exclusion state also have other asymptotically-stable states (fig. 2.2a, fig. 2.3b, 2.3c, 2.3e, and 2.3f). In addition to these five, the first case with bifurcations has multiple stable states for parameter values prior to the heteroclinic bifurcation (fig. 2.3a). We therefore have six cases in total with multiple stable states that the system may tend to, depending on initial conditions and parameter values.

While the existence of multiple stable states is an ongoing debate in ecological theory, increasing evidence suggests that multiple stable states may indeed exist in nature [9, 115, 38, 116, 101]. Being able to determine conditions under which an ecosystem may tend toward one stable state or another may be of particular interest in conservation and ecosystem management. Using this model, we provide a framework for understanding such conditions.

In all, the model presents four different cases, fig. 2.3a, 2.3d, 2.3e, and 2.3f, with stable coexistence-states. In two of these cases, the interior fixed-point is asymptotically stable for all relevant parameter values. In each of the other two cases, however, two bifurcations, one local and one global, change the nature of the coexistence state. For some parameter values, the coexistence state is an asymptotically-stable fixed-point. The Neimark–Sacker bifurcation that occurs in both cases destabilizes the interior fixed-point and gives rise to an attracting quasiperiodic invariant circle, and a global bifurcation later causes the attractor to vanish entirely.

While many studies of pioneer–climax models have shown the existence and stability of the attractor that arises after a Hopf (or Neimark–Sacker) bifurcation [120, 122, 131, 132], only one considered the persistence of the attractor. One continuous-time system noted the abrupt disappearance of the attractor [62], but in only one geometric case. This disappearance corresponds to our first case with bifurcations and the associated heteroclinic bifurcation. In the second case with bifurcations, two coexistence states occur. We discovered that the formation of a homoclinic connection between the invariant manifolds of one coexistence equilibrium (E_6) can result in the blue-sky disappearance of the attracting invariant circle that arose after the other coexistence equilibrium E_5 was destabilized. Thus, there are two cases for which the behavior of the system can change precipitously, causing a loss of any stable coexistence-state and a sudden transition of the system to a new exclusion state. Knowledge of the conditions under which an attracting coexistence-state vanishes may be important for ecosystem management.

While the structure of our model is simple, with rational fitness-functions, we believe that this model captures the major dynamics of a pioneer–climax system and provides valuable insight into

an inherently successional system. However, two species do not exist in a vacuum, and many more layers of interaction dynamics could be taken into account, as in Joshi and Blackmore's [58] higher-dimensional model. To confirm the realism of this two-dimensional model, in the future it would be beneficial to compare our model predictions with data from pioneer–climax systems. Such data may be challenging to gather, given the long timescales involved in ecological succession. Additionally, the number of parameters in this model may make parameter estimation difficult.

A limitation of our model stems from a lack of survival from one generation to the next, despite many pioneer and climax plants living longer than a single generation. One simple way of accounting for survivorship is to add small positive linear terms, $s_1 x_t$ or $s_2 y_t$, to our model, where s_1 and s_2 represent the probability of surviving to the next generation. This addition would shift our per-capita replacement rates (fig. 2.1) upwards by a constant amount. Based on preliminary analytical and numerical exploration, the additional terms will not significantly change the behavior of our model, though some restrictions on the relative strength of survivorship may be necessary to ensure stability.

Spatiotemporal dynamics of successional communities are increasingly relevant in both conservation and invasion ecology. Through spatiotemporal modeling of a pioneer-climax system, we can approach problems like determining the critical patch-size for population persistence or quantifying the rate of invasion into a new habitat by calculation of a species' spreading speed. Additionally, moving-habitat models can inform us whether or not populations can keep pace with climate-induced range shifts. With such germane and interesting problems, future work should focus on incorporating spatial components into our model.

After the many initial studies into the basic dynamics of pioneer–climax models and the potential for reversing bifurcations and restoring stability in those models (e.g., [120, 131, 123, 62]), research on pioneer–climax systems has indeed made the shift to spatiotemporal models, but it has largely focused on reaction-diffusion models. Much of this research has focused on proving the existence of traveling waves [13, 16, 152, 51, 151, 18]. Other studies have looked at Turing

and Hopf bifurcations in reaction-diffusion systems [14, 81]. Two isolated studies have examined spreading speed within a reaction-diffusion context [147, 18].

These studies provide a valuable starting point in the analysis of spatiotemporal dynamics of pioneer–climax systems. However, the problems mentioned above on critical patch-size and moving-habitat models are wholly unexamined, and only two studies have examined spreading speed [147, 18]. Furthermore, reaction-diffusion models are limited in their ecological realism, as dispersal is often non-diffusive and growth, particularly in plants, is frequently seasonal [76, 84].

Using the discrete-time model presented here, however, we can develop a more ecologically-realistic spatiotemporal integrodifference-equation model to examine the same problems. These models have the benefit of separating growth and dispersal, and they take long-distance dispersal into account in a way reaction-diffusion models do not. With flexible dispersal kernels and separation of growth and dispersal phases, a common feature in plant populations, integrodifference equations provide a more ecologically realistic method of examining some of these spatial issues in invasions and conservation [64, 76, 84].

Before moving to these more complex questions, it is critical that we understand the dynamics of the underlying foundational models, like the one analyzed here. Our work in analyzing this discrete-time system not only advances our knowledge of stationary pioneer–climax dynamics, but also paves the way for situating our model within a spatial context. With this framework, we have the ability to examine how these species will persist, invade new habitat, and survive in an ever-changing environment.

Appendices

A.2 Preliminary organization and derivatives for the Jacobian

Throughout all appendices, we will refer to the fixed points as E_1–E_6, and their individual components as x_1–x_6 and y_1–y_6. Equation (2.13)–eq. (2.18) provide the explicit forms of the equilibria, which are used only in rare cases. We now drop all time-dependent notation, as we are analyz-

ing fixed points (x, y) that, by definition, do not change over time. In all of our calculations, we consider only nonnegative x and y, and therefore nonnegative m and n. All parameters are positive.

We first recall that there are nine different geometric cases (illustrated in fig. 2.2 and fig. 2.3) for this system, and up to six equilibria that exist in each case. The parameter restrictions bounding each of the nine cases are summarized in table 2.2. In three cases, only boundary fixed-points exist. In the other six cases, one or both interior fixed-points occur in addition to the boundary equilibria. Stability analyses for the boundary fixed-points are relatively straightforward, and each boundary fixed-point can be analyzed individually and its stability classified for each case based on the parameter restrictions from table 2.2. The interior fixed-points present more of a challenge, and are examined on a case-by-case basis. The inequalities presented in table 2.2 are also heavily used in classifying the stabilities for the interior fixed-points. The stabilities of the fixed points for all nine cases are summarized in table 2.3.

To begin our stability analyses, we first present some general results that we will use extensively. After this initial setup is complete, we proceed to the boundary fixed-points and classify the stability of each boundary fixed-point for all nine cases by examining the magnitudes of the eigenvalues of Jacobian (2.19). We finally move to the interior fixed-points and lay out a few general results that are specific to the interior fixed-points and the eigenvalues of Jacobian (2.19) evaluated at the interior fixed-points. Our stability analyses for the interior fixed-points proceed on a case-by-case basis, and for each case, we use the Jury conditions (eq. (2.20)) and Descartes' Rule of Signs [29] to bound the eigenvalues of the Jacobian evaluated at the given interior fixed-point.

A.2.1 Derivatives for the Jacobian

Recall that a fixed point is asymptotically stable if both eigenvalues of Jacobian (2.19) evaluated at the fixed point are less than 1 in magnitude. If stability of a fixed point is classified through use of the Jury conditions, the trace τ and determinant Δ of the Jacobian are important quantities for consideration. When evaluated at a fixed point, our Jacobian matrix (2.19) has elements con-

Table 2.2 Parameter restrictions for each of the nine geometric cases. For the six parameter regimes with at least one interior fixed-point, these conditions are the same as those for existence of the interior fixed-point(s) in the first quadrant. A dash in the "Case" column indicates that no specific label has been assigned to that case. A dash in the "Interior fixed-point" column indicates no interior fixed-point exists for that parameter regime. There is no Condition 3 for the three parameter regimes with no interior equilibria, as that condition was derived by restricting an interior fixed-point to be within the first quadrant.

Figure	Case	Interior fixed-point	Condition 1	Condition 2	Condition 3
fig. 2.2a	–	–	$v_1 < n_1^*/m^*$	$v_2 > m^*/n_1^*$	–
fig. 2.2b	–	–	$n_1^*/m^* < v_1 < n_2^*/m^*$	$m^*/n_2^* < v_2 < m^*/n_1^*$	–
fig. 2.2c	–	–	$v_1 > n_2^*/m^*$	$v_2 < m^*/n_2^*$	–
fig. 2.3a	a	E_5	$n_1^*/m^* < v_1 < n_2^*/m^*$	$v_2 > m^*/n_1^*$	$1 < v_1 v_2$
fig. 2.3b	b	E_5	$v_1 < n_1^*/m^*$	$m^*/n_2^* < v_2 < m^*/n_1^*$	$v_1 v_2 < 1$
fig. 2.3c	c	E_6	$v_1 > n_2^*/m^*$	$m^*/n_2^* < v_2 < m^*/n_1^*$	$1 < v_1 v_2$
fig. 2.3d	d	E_6	$n_1^*/m^* < v_1 < n_2^*/m^*$	$v_2 < m^*/n_2^*$	$v_1 v_2 < 1$
fig. 2.3e	e	E_5 and E_6	$v_1 > n_2^*/m^*$	$v_2 > m^*/n_1^*$	$1 < v_1 v_2$
fig. 2.3f	f	E_5 and E_6	$v_1 < n_1^*/m^*$	$v_2 < m^*/n_2^*$	$v_1 v_2 < 1$

taining the derivatives of the fitness functions, including the particular quantities $1 + x_i f'(m_i)$ and $1 + y_i g'(n_i)$, where x_i and y_i are the coordinates of the fixed point and m_i and n_i are also evaluated at that fixed point. Before beginning our stability analyses, it is useful to present some general results pertaining to the derivatives of the fitness functions and these key quantities.

First, we explicitly calculate the forms of the derivatives $f'(m)$ and $g'(n)$, where

$$f'(m) = \frac{-aR_1}{(1+am)^2} < 0 \tag{A1}$$

for all m. We will write $g'(n)$ in a way that is particularly useful by first considering the expression

Table 2.3 Stability of each equilibrium point in the nine different cases. A dash indicates the fixed point does not exist in the first quadrant for that parameter regime.

Figure	E_1	E_2	E_3	E_4	E_5	E_6
fig. 2.2a	saddle point	stable node	saddle point	stable node	–	–
fig. 2.2b	saddle point	saddle point	unstable node	stable node	–	–
fig. 2.2c	saddle point	stable node	unstable node	saddle point	–	–
fig. 2.3a	saddle point	saddle point	saddle point	stable node	bifurcations	–
fig. 2.3b	saddle point	stable node	unstable node	stable node	saddle point	–
fig. 2.3c	saddle point	stable node	unstable node	stable node	–	saddle point
fig. 2.3d	saddle point	saddle point	unstable node	saddle point	–	stable node
fig. 2.3e	saddle point	stable node	saddle point	stable node	bifurcations	saddle point
fig. 2.3f	saddle point	stable node	unstable node	saddle point	saddle point	stable node

$$\begin{aligned} 1-g(n) &= \frac{1+b_2n^2-R_2(1+b_1n)}{1+b_2n^2} \\ &= \frac{b_2(n-n_1^*)(n-n_2^*)}{1+b_2n^2}, \end{aligned} \tag{A2}$$

where we factored the numerator to obtain the second equality. Differentiating both sides with respect to n, we find

$$g'(n) = \frac{-b_2[(n-n_1^*)+(n-n_2^*)]}{1+b_2n^2} + \frac{2b_2^2n(n-n_1^*)(n-n_2^*)}{(1+b_2n^2)^2}, \tag{A3}$$

which may be either positive or negative. In particular, note that for $n=n_1^*$, $g'(n)>0$, and when $n=n_2^*$, $g'(n)<0$.

Next, note that

$$\frac{\partial}{\partial x}[f(m)x] = f(m)+xf'(m)\frac{\partial m}{\partial x} = f(m)+xf'(m), \tag{A4}$$

which is the upper-left entry in Jacobian matrix (2.19) for this system. Explicitly calculating this quantity, we find

$$\frac{\partial}{\partial x}\left[f(m)\,x\right] = \frac{R_1\left(1+a\,v_2\,y\right)}{\left[1+a\left(x+v_2\,y\right)\right]^2} > 0. \tag{A5}$$

Thus, for all nonnegative x and y,

$$f\left(m\right)+x\,f'\left(m\right) > 0. \tag{A6}$$

At fixed points E_2, E_5, and E_6, $f\left(m\right)=1$, and so eq. (A6) simplifies even further to

$$1+x_i\,f'\left(m_i\right) > 0 \tag{A7}$$

for $i=2,5,6$, $m_i = x_i + v_2\,y_i$.

We now consider the lower-right entry of the Jacobian matrix. As above,

$$\frac{\partial}{\partial y}\left[g(n)\,y\right] = g\left(n\right)+y\,g'\left(n\right)\frac{\partial n}{\partial y} = g\left(n\right)+y\,g'\left(n\right). \tag{A8}$$

Unlike eq. (A6), we do not prove this quantity is positive in general. However, it is positive at each of the four equilibria E_3–E_6 for which $y\neq 0$ and $g\left(n\right)=1$. We now prove this statement for each of the four fixed points individually.

At E_3, recall that $y=n=n_1^*$. Substituting this relation into eq. (A8) and using eq. (A3) to simplify the derivative, we obtain

$$g\left(n\right)+y\,g'\left(n\right) = 1+\frac{b_2 n_1^*\left(n_2^*-n_1^*\right)}{1+b_2\left(n_1^*\right)^2} > 0, \tag{A9}$$

as $n_2^* > n_1^*$.

Similarly, at E_4, $y=n=n_2^*$. Again substituting this relation into eq. (A8), we find

$$g\left(n\right)+y\,g'\left(n\right) = 1-\frac{b_2 n_2^*\left(n_2^*-n_1^*\right)}{1+b_2\left(n_2^*\right)^2} = \frac{1+b_2 n_1^* n_2^*}{1+b_2\left(n_2^*\right)^2} > 0, \tag{A10}$$

after finding a common denominator and simplifying.

For E_5, we have $y = y_5$ and $n = v_1 x_5 + y_5 = n_1^*$. Using the same process as above,

$$g(n) + y g'(n) = 1 + \frac{b_2 y_5 (n_2^* - n_1^*)}{1 + b_2 (n_1^*)^2} > 0. \tag{A11}$$

Finally, at E_6, $y = y_6$ and $n = v_1 x_6 + y_6 = n_2^*$. Instead of using the fact that $g(n_2^*) = 1$, we substitute the explicit form of $g(n_2^*)$, which has the same denominator as that of $g'(n_2^*)$. We find that

$$g(n) + y g'(n) = \frac{R_2(1 + b_1 n_2^*) - b_2 y_6 (n_2^* - n_1^*)}{1 + b_2 (n_2^*)^2}. \tag{A12}$$

The denominator is positive, so if the numerator is positive then eq. (A12) is positive as desired. Considering the numerator of eq. (A12), we begin by substituting for $n_2^* - n_1^*$, yielding

$$\begin{aligned} &R_2 (1 + b_1 n_2^*) - b_2 y_6 (n_2^* - n_1^*) \\ &= R_2 (1 + b_1 n_2^*) - y_6 \sqrt{R_2^2 b_1^2 - 4 b_2 (1 - R_2)}. \end{aligned} \tag{A13}$$

For convenience, denote

$$c = \sqrt{R_2^2 b_1^2 - 4 b_2 (1 - R_2)} \tag{A14}$$

and substitute $n_2^* = v_1 x_6 + y_6$ into eq. (A13) to obtain

$$\begin{aligned} &R_2 [1 + b_1 (v_1 x_6 + y_6)] - c y_6 \\ &= R_2 (1 + b_1 v_1 x_6) + y_6 (R_2 b_1 - c). \end{aligned} \tag{A15}$$

Finally, using

$$\begin{aligned} n_1^* &= \frac{R_2 b_1 - c}{2 b_2} \\ \implies 2 b_2 n_1^* &= R_2 b_1 - c, \end{aligned} \tag{A16}$$

we can rewrite eq. (A15) as

$$\begin{aligned} &R_2 (1 + b_1 v_1 x_6) + y_6 (R_2 b_1 - c) \\ &= R_2 (1 + b_1 v_1 x_6) + y_6 (2 b_2 n_1^*). \end{aligned} \tag{A17}$$

which is clearly positive. Thus, the numerator of eq. (A12) is positive and therefore eq. (A12) is positive.

We have just shown that $g(n) + y\,g'(n) > 0$ when evaluated at each of the fixed points E_3–E_6, i.e.,

$$1 + y_i\,g'(n_i) > 0 \tag{A18}$$

for $i = 3,4,5,6$, $n_i = v_1 x_i + y_i$.

B.2 Stability of boundary fixed-points

With these general quantities and inequalities laid out, we now establish the stability of the four boundary fixed-points for all nine parameter regimes. Refer to table 2.1 for the eigenvalues for each fixed point E_1–E_4.

First, note that all eigenvalues are positive and real for the boundary fixed-points. It is clear that the eigenvalues for E_1 are positive and real, as the eigenvalues are the populations' net reproductive rates, which must be positive. Furthermore, as the fitness functions $f(m)$ and $g(n)$ are always real and greater than zero, it is evident that $\lambda_1 > 0$ and is real for E_2–E_4. Next, consider λ_2 as given in table 2.1. As demonstrated in appendix A.2 by eq. (A7), eq. (A9), and eq. (A10), we see that $\lambda_2 > 0$ for E_2–E_4. Thus, both eigenvalues are positive for all four boundary fixed-points. To prove stability of E_1–E_4, it is therefore sufficient to show whether each eigenvalue λ_1 and λ_2 is greater or less than $+1$.

With the knowledge that $f'(m) < 0$ always, $g'(n_1^*) > 0$, $g'(n_2^*) < 0$, and the results shown in appendix A.2, we may continue with proving the stability of the boundary fixed-points for the nine cases shown in fig. 2.2 and fig. 2.3.

B.2.1 Stability of trivial extinction-state E_1

As mentioned in section 2.4.1, the equilibrium E_1 at the origin is always a saddle point, as the associated eigenvalues of the Jacobian are $R_1 > 1$ and $0 < R_2 < 1$.

B.2.2 Stability of climax-exclusion state E_2

By construction of the climax fitness function $g(n)$, there are two roots n, n_1^* and n_2^*, where $g(n) = 1$. For values of n below and above those roots, $g(n) < 1$, and for values of n between the roots, $g(n) > 1$ (see fig. 2.1b).

Consider $n = v_1 x$. Then, $g(n) = g(v_1 x)$. The two roots where $g(v_1 x) = 1$ are given by

$$v_1 x_\alpha = n_1^* \implies x_\alpha = n_1^*/v_1, \tag{A19a}$$

$$v_1 x_\beta = n_2^* \implies x_\beta = n_2^*/v_1. \tag{A19b}$$

Thus, the value of $\lambda_1 = g(v_1 x_2)$ depends on where x_2 falls in relation to x_α and x_β from eq. (A19). Let $n_2 = v_1 x_2$. We see that

$$x_2 < x_\alpha \implies n_2 < n_1^* \implies \lambda_1 = g(n_2) < 1, \tag{A20a}$$

$$x_2 > x_\beta \implies n_2 > n_1^* \implies \lambda_1 = g(n_2) < 1, \tag{A20b}$$

$$x_\alpha < x_2 < x_\beta \implies n_1^* < n_2 < n_2^* \implies \lambda_1 = g(n_2) > 1. \tag{A20c}$$

Observe that x_α and x_β are the x-intercepts of the two zero-growth isoclines where $g(n) = 1$, while x_2 is the x-intercept of the zero-growth isocline $f(m) = 1$. Thus, we can read off the magnitude of λ_1 straight from the configuration of the zero-growth isoclines for a particular case.

Recall that $\lambda_2 = f(x_2) + x_2 f'(x_2) = 1 + x_2 f'(x_2)$. By eq. (A7), $\lambda_2 > 0$. As $f'(m) < 0$ for all m, $\lambda_2 < 1$.

Combining our analysis for both eigenvalues, we see that stability depends on λ_1, as $0 < \lambda_2 < 1$. E_2 will be a stable node if the nontrivial pioneer zero-growth isocline intercepts the x-axis to the left or right of both nontrivial climax zero-growth isoclines ($x_2 < x_\alpha$ or $x_2 > x_\beta$). It will be a saddle point if the nontrivial pioneer zero-growth isocline intercepts the x-axis between the two nontrivial climax zero-growth isoclines ($x_\alpha < x_2 < x_\beta$). See fig. 2.2 and fig. 2.3 for details. The stability of E_2 for each of the nine cases is summarized in table 2.3.

B.2.3 Stability of pioneer-exclusion states E_3 and E_4

Now, consider the construction of the pioneer fitness function. There is one root m where $f(m) = 1$. For values of m below this root, $f(m) > 1$, and for values of m above this root, $f(m) < 1$ (see fig. 2.1a).

Take $m = v_2 y$. Then $f(m) = f(v_2 y)$. The root where $f(v_2 y) = 1$ is

$$v_2 y_\alpha = \frac{R_1 - 1}{a} = m^* \implies y_\alpha = m^*/v_2. \tag{A21}$$

As with E_2, for E_3 the value of $\lambda_1 = f(v_2 y_3)$ depends on the size of y_3 relative to y_α. Similarly, for E_4 the value of $\lambda_1 = f(v_2 y_4)$ depends on the size of y_4 relative to y_α. Let $m_3 = v_2 y_3$ and $m_4 = v_2 y_4$.

For E_3,

$$y_3 < y_\alpha \implies m_3 < m^* \implies \lambda_1 = f(m_3) > 1, \tag{A22a}$$

$$y_3 > y_\alpha \implies m_3 > m^* \implies \lambda_1 = f(m_3) < 1. \tag{A22b}$$

For E_4,

$$y_4 < y_\alpha \implies m_4 < m^* \implies \lambda_1 = f(m_4) > 1, \tag{A23a}$$

$$y_4 > y_\alpha \implies m_4 > m^* \implies \lambda_1 = f(m_4) < 1. \tag{A23b}$$

As in our analysis for E_2, note that y_α is the y-intercept of the zero-growth isocline $f(m) = 1$, while y_3 and y_4 are the y-intercepts of the two zero-growth isoclines where $g(n) = 1$. We can again obtain the magnitude of λ_1 for both E_3 and E_4 directly from the configuration of the zero-growth isoclines for a particular case.

Turning to $\lambda_2 = 1 + y_i g'(y_i)$, $i = 3$ or 4, we have shown that $\lambda_2 > 0$ for E_3 (eq. (A9)) and E_4 (eq. (A10)). At E_3, $y = n_1^*$ and $g'(n_1^*) > 0$. Thus, $\lambda_2 > 1$ at E_3. Conversely, at E_4, $y = n_2^*$ and $g'(n_2^*) < 0$, so $\lambda_2 < 1$ at E_4.

The natures of the equilibrium points E_3 and E_4 depend on their respective λ_1. For E_3, $\lambda_2 > 1$, so E_3 is an unstable node if the lower nontrivial climax zero-growth isocline intercepts the y-axis

below the nontrivial pioneer zero-growth isocline ($y_3 < y_\alpha$), and is a saddle point if the lower nontrivial climax zero-growth isocline intercepts the y-axis above the nontrivial pioneer zero-growth isocline ($y_3 > y_\alpha$).

For E_4, $0 < \lambda_2 < 1$, so E_4 is a saddle point if the upper nontrivial climax zero-growth isocline intercepts the y-axis below the nontrivial pioneer zero-growth isocline ($y_4 < y_\alpha$), and is a stable node if the upper nontrivial climax zero-growth isocline intercepts the y-axis above the nontrivial pioneer zero-growth isocline ($y_4 > y_\alpha$). See fig. 2.2 and fig. 2.3 for illustration. The stability of E_3 and E_4 for each of the nine cases is summarized in table 2.3.

C.2 Stability of interior fixed-points

We now turn to the stability of the two interior fixed-points E_5 and E_6, given by eq. (2.17) and eq. (2.18). Rather than examining each fixed-point separately and handling all cases for a particular fixed-point at once, as in appendix B.2, it is simpler to organize this section by individual case. The stability analyses proceed by checking the three Jury conditions (eq. (2.20)) for each of the six cases in which one or both interior fixed-points occur. We also frequently use Descartes' Rule of Signs [29] to bound the eigenvalues of the Jacobian. For convenience, we will refer to these six cases by the letter of their corresponding subfigure in fig. 2.3, e.g., case *a* corresponds to fig. 2.3a. Before beginning on a case-by-case basis, we present several results that simplify the overall analysis.

C.2.1 Conditions for existence of interior fixed-points

For each of the six cases *a–f*, three conditions on v_1 and v_2 must be satisfied to guarantee existence of an interior fixed-point in the first quadrant. The conditions are easily derived by ensuring that both numerator and denominator are of the same sign for the pairs (x_5, y_5) and (x_6, y_6) – one condition comes from setting the numerator of the x-coordinate to be positive (negative), one condition from setting the numerator of the y-coordinate to be positive (negative), and one condition from setting the shared denominator $1 - v_1 v_2$ to be positive (negative). These conditions are pre-

sented in table 2.2 and will be heavily used in proving stability of the interior fixed-points. From now on, when we say that an interior fixed-point exists, we are specifically referring to an interior fixed-point that exists inside the first quadrant, i.e., $x > 0$ and $y > 0$.

C.2.2 Descartes' rule of signs

In addition to the conditions from table 2.2, we make liberal use of Descartes' Rule of Signs [29] throughout our analyses, and provide a brief refresher on this useful technique here. Consider the characteristic polynomial for the Jacobian given by

$$\chi(\lambda) = \lambda^2 - \tau\lambda + \Delta, \tag{A24}$$

whose roots are the eigenvalues of Jacobian (2.19) and where the coefficients τ and Δ are the trace and determinant of the Jacobian. According to Descartes' Rule of Signs, the number of positive real roots of eq. (A24) — and therefore positive real eigenvalues of the Jacobian — is equal to the number of sign changes between consecutive coefficients of the polynomial, or less than it by some even number [29]. Thus, if there are two sign changes, we have either two or zero positive roots.

In addition, we can find the number of negative real roots of the characteristic polynomial by counting the number of sign changes in the coefficients of

$$\chi(-\lambda) = \lambda^2 + \tau\lambda + \Delta, \tag{A25}$$

Again, the number of negative roots is equivalent to the number of sign changes or less by an even number, so if there are two sign changes in eq. (A25), there are two or zero negative roots.

By introducing a change of variable, we can use Descartes' Rule of Signs once more to check how many roots are greater than $+1$, simplifying the stability analysis for several cases. To analyze eigenvalues around $+1$, we introduce the shift

$$\mu = \lambda - 1 \implies \lambda = 1 + \mu. \tag{A26}$$

Substituting this into eq. (A24), we obtain

$$\chi(\mu) = \mu^2 + (2-\tau)\mu + (1-\tau+\Delta), \tag{A27}$$

and note that the constant term is the same as the left-hand side of the first Jury condition (eq. (2.20a)). Thus, any roots $\mu > 0$ correspond to $\lambda > 1$.

C.2.3 General results for τ and Δ

Finally, we present a few useful quantities and relationships pertaining to the interior fixed-points. These are summarized in table 2.4. In particular, we examine the trace τ and determinant Δ of Jacobian (2.19), and use the results of our examination to simplify the first and second Jury conditions as well as to bound the eigenvalues of the Jacobian for both interior fixed-points.

Recall that for both interior fixed-points E_5 and E_6, $f(m) = 1$, $g(n) = 1$, and $m = m^*$ after substituting in the explicit forms of the equilibria. For E_5, $n = n_1^*$ and for E_6, $n = n_2^*$ after substitution of the equilibria.

We can write the trace of the Jacobian, τ, as

$$\tau = 2 + x f'(m) + y g'(n). \tag{A28}$$

Note that τ is positive for the Jacobian evaluated at both E_5 and E_6, as we have shown that both $1 + x f'(m) > 0$ and $1 + y g'(n) > 0$ for E_5 and E_6 (eq. (A7), eq. (A11), eq. (A12)).

The determinant of the Jacobian, Δ, can be written as

$$\Delta = \left[1 + x f'(m)\right]\left[1 + y g'(n)\right] - v_1 v_2 x y f'(m) g'(n) \tag{A29}$$

for $(x, y) = (x_5, y_5)$ or (x_6, y_6).

It is clear that $\Delta > 0$ when the Jacobian is evaluated at E_5. By the results of eq. (A7) and eq. (A11), the first two terms of eq. (A29) are positive, and therefore their product is positive. At E_5, $g'(n) > 0$, and thus the entire third term of eq. (A29), $[-v_1 v_2 x y f'(m) g'(n)]$, is positive. Therefore, $\Delta > 0$ at E_5.

Table 2.4 Quantities and relationships frequently used in Descartes' Rule of Signs or in checking the Jury conditions.

Fixed point	m	n	$f(m)$	$g(n)$	$f'(m)$	$g'(n)$	τ	Δ	Sign changes in $\chi(\lambda)$	Sign changes in $\chi(-\lambda)$
E_5	m^*	n_1^*	1	1	<0	>0	>0	>0	2	0
E_6	m^*	n_2^*	1	1	<0	<0	>0	>0	2	0

It is not as straightforward to show that $\Delta > 0$ when the Jacobian is evaluated at E_6, but this statement is indeed true for all four cases *c*–*f* in which E_6 exists. We rewrite the determinant from eq. (A29), plugging in the explicit fixed-point coordinates given in eq. (2.18) and simplified derivatives from eq. (A1) and eq. (A3). After expanding and finding a common denominator, then rearranging and grouping like terms, we obtain the very long expression

$$\begin{aligned}\Delta = &\frac{(v_1 v_2 - 1) + b_2 n_1^* (m^* v_1 - n_2^*) + b_2 v_1 n_2^* (v_2 n_2^* - m^*)}{(1 + a m^*)\left[1 + b_2 \left(n_2^*\right)^2\right](v_1 v_2 - 1)} \\ &+ \frac{a v_2 (m^* v_1 - n_2^*) + a b_2 n_1^* n_2^* v_2 (v_1 m^* - n_2^*)}{(1 + a m^*)\left[1 + b_2 \left(n_2^*\right)^2\right](v_1 v_2 - 1)}.\end{aligned} \tag{A30}$$

In cases *c* and *e*, we see from condition three in table 2.2 that the denominator of eq. (A30) is positive. Thus, we require the numerator be positive in these two cases for $\Delta > 0$. First, note that all quantities multiplying each parenthetical term are positive (this statement is true for all four cases *c*–*f*). Each parenthetical quantity in the numerator is in fact a condition from table 2.2, and so we know the signs of these quantities. From the first condition for cases *c* and *e*, $m^* v_1 - n_2^* > 0$, from the second, $v_2 n_2^* - m^* > 0$, and we have already used the third condition. Thus, the numerator is also positive, and $\Delta > 0$ for the Jacobian evaluated at E_6 in cases *c* and *e*.

For cases *d* and *f*, the third condition from table 2.2 shows that the denominator of eq. (A30) is negative, so we would like to show that the numerator is negative for $\Delta > 0$. As with cases *c* and *e*, each parenthetical quantity corresponds to a condition from table 2.2, and we now know $m^* v_1 - n_2^* < 0$ and $v_2 n_2^* - m^* < 0$, in addition to the third condition we have already used. Thus, the numerator is a sum of negative quantities, and is therefore negative. Once again, $\Delta > 0$ for the Jacobian evaluated at E_6 in cases *d* and *f*.

Given that $\tau > 0$ and $\Delta > 0$ for the Jacobian evaluated at both E_5 and E_6, the second Jury condition $1 + \tau + \Delta > 0$ will clearly always be satisfied for both interior fixed-points for all cases *a*–*f* (assuming the interior fixed-point exists).

Additionally, observe that $\tau > 0$ and $\Delta > 0$ means there are two sign changes between coeffi-

cients in eq. (A24) and zero sign changes in eq. (A25). Therefore, by Descartes' Rule of Signs, there are zero negative eigenvalues and either two or zero positive eigenvalues of the Jacobian. Thus, for both interior fixed-points in all cases *a* through *f* (assuming the interior fixed-point exists), all real eigenvalues are positive. Furthermore, we either have two real, positive eigenvalues, or a pair of complex-conjugate eigenvalues for both interior fixed-points in all cases.

Finally, we simplify the expression for the first Jury condition using our knowledge of τ and Δ. After substituting eq. (A28) and eq. (A29) into the left-hand side of the first Jury condition (eq. (2.20a)), we obtain

$$1-\tau+\Delta = x\,y\,f'(m)\,g'(n)\,(1-v_1v_2) \tag{A31}$$

for $(x, y) = (x_5, y_5)$ or (x_6, y_6). As already stated, we consider only positive equilibria (see section 2.4.2 for a discussion of the border cases where an interior fixed-point hits an axis as a parameter is varied). We know that $f'(m) < 0$ always. Thus, ascertaining whether the first Jury condition is satisfied comes down to the sign of $g'(n)$, which is positive at E_5 and negative at E_6, and the sign of $1 - v_1v_2$, which is given by condition three in table 2.2. We now proceed to a case-by-case stability analysis, recalling that a summary of the general results presented in this section are found in table 2.4. This information will be particularly useful when examining cases *e* and *f*.

C.2.4 Case A

In case *a*, we have one interior fixed-point E_5. The first Jury condition

$$1-\tau+\Delta = x_5\,y_5\,f'(m_5)\,g'(n_5)\,(1-v_1v_2) > 0 \tag{A32}$$

by condition three in table 2.2. Thus, the first Jury condition is always satisfied. We already know that the second Jury condition is always satisfied.

The third Jury condition is $\Delta < 1$. After expanding the expression for Δ from eq. (A29) we see that the third Jury condition $\Delta < 1$ is equivalent to

$$x\,f'(m) + y\,g'(n) + x\,y\,f'(m)\,g'(n)\,(1-v_1\,v_2) < 0. \tag{A33}$$

This expression does not simplify further in a useful manner. Instead, we look to express the left-hand side of eq. (A33) in terms of our relative competition-coefficients v_1 and v_2, and find the curve in v_1–v_2 space where $\Delta = 1$ (or eq. (A33) is equal to zero). In other words, we want to find the boundary where we violate the third Jury condition, such that crossing that boundary causes a change of stability of E_5 in case a.

To find this boundary in v_1–v_2 space, we will substitute the explicit forms of x_5 and y_5 into the left-hand side of eq. (A33). Recall from table 2.4 that $m_5 = m^*$ and $n_5 = n_1^*$. As the derivatives $f'(m^*)$ and $g'(n_1^*)$ do not have v_1 or v_2 dependence, we can leave them in their general form. After this substitution and minor simplification, the boundary where we violate the third Jury condition is given by

$$\begin{aligned} 0 \;=\; & \frac{(m^* - v_2 n_1^*) f'(m^*)}{1 - v_1 v_2} + \frac{(n_1^* - v_1 m^*) g'(n_1^*)}{1 - v_1 v_2} \\ & + \frac{(m^* - v_2 n_1^*)(n_1^* - v_1 m^*) f'(m^*) g'(n_1^*)}{1 - v_1 v_2}. \end{aligned} \tag{A34}$$

From condition three in table 2.2, we know $1 - v_1 v_2 \neq 0$ while in this case, and so we safely multiply both sides by $1 - v_1 v_2$ to obtain

$$0 = (m^* - v_2 n_1^*) f'(m^*) + (n_1^* - v_1 m^*) g'(n_1^*) + (m^* - v_2 n_1^*)(n_1^* - v_1 m^*) f'(m^*) g'(n_1^*). \tag{A35}$$

Rearranging and solving for v_2 as a function of v_1 gives us the curve

$$\begin{aligned} v_2 = h(v_1) = & \frac{v_1 \left[m^* g'(n_1^*) + (m^*)^2 f'(m^*) g'(n_1^*) \right]}{n_1^* f'(m^*) \left[v_1 m^* g'(n_1^*) - n_1^* g'(n_1^*) - 1 \right]} \\ & - \frac{m^* f'(m^*) + n_1^* g'(n_1^*) + m^* n_1^* f'(m^*) g'(n_1^*)}{n_1^* f'(m^*) \left[v_1 m^* g'(n_1^*) - n_1^* g'(n_1^*) - 1 \right]}. \end{aligned} \tag{A36}$$

While eq. (A36) does not simplify further, it should be noted that all quantities are constants except for v_1 and v_2, assuming that all other parameters are held constant. Thus, $v_2 = h(v_1)$ from eq. (A36) gives us the boundary of the region in v_1–v_2 space where E_5 satisfies the third Jury condition (see fig. 2.4a).

We will briefly note that this curve does yield both a vertical and horizontal asymptote. The vertical asymptote occurs at

$$v_1 = v_1^* = \frac{n_1^* g'(n_1^*) + 1}{m^* g'(n_1^*)} \tag{A37}$$

and the horizontal asymptote at

$$v_2 = v_2^* = \frac{m^* f'(m^*) + 1}{n_1^* f'(m^*)}. \tag{A38}$$

Equation (A36) therefore has two branches. The left branch is valid for $v_1 < v_1^*$ and $v_2 > v_2^*$, and the right branch is valid for $v_1 > v_1^*$ and $v_2 < v_2^*$, with v_1^* and v_2^* given by eq. (A37) and eq. (A38). However, note that

$$v_2^* = \frac{m^* f'(m^*) + 1}{n_1^* f'(m^*)} = \frac{m^*}{n_1^*} + \frac{1}{n_1^* f'(m^*)} < \frac{m^*}{n_1^*}. \tag{A39}$$

Recall by condition two from table 2.2 that case *a* requires $v_2 > \frac{m^*}{n_1^*}$. Therefore, the right branch of eq. (A36), for which $v_2 < v_2^* < \frac{m^*}{n_1^*}$ is not a valid solution for this parameter regime, and so we only consider the left branch of eq. (A36) when determining the region of stability for E_5. On one side of the left branch of $v_2 = h(v_1)$, E_5 is stable, and on the other side of the curve E_5 is unstable.

C.2.5 Case B

In case *b*, we have the same interior fixed-point E_5 as in case *a*. For the first Jury condition, we see that the third condition from table 2.2 is reversed, and

$$1 - \tau + \Delta = x_5\, y_5\, f'(m_5)\, g'(n_5)\,(1 - v_1 v_2) < 0. \tag{A40}$$

The first Jury condition is never satisfied. By failing the first Jury condition, we know there must be at least one eigenvalue $\lambda_1 > 1$. We can confirm this fact by examining the shifted characteristic polynomial in eq. (A27). By our above analysis, we know the constant term $1 - \tau + \Delta < 0$, so no matter the sign of $2 - \tau$, the coefficient of the linear term, there will be one sign change between consecutive coefficients in eq. (A27). Therefore we have one positive real root μ_1, and thus only one eigenvalue $\lambda_1 > 1$.

We have already demonstrated that in general, if the eigenvalues associated with an interior fixed-point are real, they will both be positive. As we have one real λ, both must be real, as complex eigenvalues come in pairs. We therefore have $\lambda_1 > 1$, $0 < \lambda_2 < 1$, and thus E_5 is a saddle point in case *b*.

C.2.6 Case C

In case *c*, we have one interior fixed-point E_6. As in case *b*, the first Jury condition is never satisfied as

$$1 - \tau + \Delta = x_6\, y_6\, f'(m_6)\, g'(n_6)\,(1 - v_1 v_2) < 0 \tag{A41}$$

using the third condition from table 2.2. Precisely as before, we will use Descartes' Rule of Signs to bound our eigenvalues. We have at least one eigenvalue $\lambda_1 > 1$, by the results of the first Jury condition. To determine if both eigenvalues are larger than $+1$, we examine the shifted characteristic polynomial (eq. (A27)). As before, we know the constant term $1 - \tau + \Delta < 0$, so no matter the sign of $2 - \tau$, there is one sign change between the polynomial coefficients. Thus, there is one positive real root μ_1, and therefore only one root $\lambda_1 > 1$. Given one real λ, the other eigenvalue must be real as well, and we know all real eigenvalues are positive for the interior fixed-points. Thus, $\lambda_1 > 1$, $0 < \lambda_2 < 1$, and E_6 is a saddle point for case *c*.

C.2.7 Case D

In case *d*, we have the same interior fixed-point E_6 as in case *c*. Using the third condition from table 2.2, we now see

$$1 - \tau + \Delta = x_6\, y_6\, f'(m_6)\, g'(n_6)\,(1 - v_1 v_2) > 0, \tag{A42}$$

and the first Jury condition is always satisfied in this case. The second Jury condition is also always satisfied.

Rather than checking the third Jury condition $\Delta < 1$, we instead show that both eigenvalues are real and bounded between 0 and $+1$. This statement is evidently sufficient to classify the fixed point, and proving realness eliminates the need to check the third Jury condition, which tests complex eigenvalues.

Consider the generalized eigenvalues of the Jacobian matrix evaluated at E_6, which are the roots of the characteristic polynomial eq. (A24):

$$\lambda_{1,2} = \frac{\tau \pm \sqrt{\tau^2 - 4\Delta}}{2}. \tag{A43}$$

If $\tau^2 - 4\Delta > 0$, then both eigenvalues are real. Using the trace from eq. (A28) and the expanded form of the determinant in eq. (A29), after combining like terms we find

$$\begin{aligned} \tau^2 - 4\Delta &= \left[x_6 f'(m_6)\right]^2 + \left[y_6 g'(n_6)\right]^2 - 2x_6 y_6 f'(m_6) g'(n_6) \\ &\quad + 4v_1 v_2 x_6 y_6 f'(m_6) g'(n_6) \\ &= \left[x_6 f'(m_6) - y_6 g'(n_6)\right]^2 + 4v_1 v_2 x_6 y_6 f'(m_6) g'(n_6) > 0, \end{aligned} \tag{A44}$$

as both terms are clearly positive under the conditions of this case. In fact, this statement holds for E_6 for any parameter regime, as we are not using conditions pertaining to a particular case, only conditions that are true at E_6. Thus, both eigenvalues are real for all cases where E_6 exists.

Having proved the eigenvalues are real, we again use Descartes' Rule of Signs to bound the eigenvalues. By our earlier result from section C.2.3, since our eigenvalues are real we must have two positive eigenvalues, $\lambda_{1,2} > 0$.

We will use the shifted characteristic polynomial (eq. (A27)) to determine if $\lambda_{1,2} > 1$. By the first Jury condition, we know the constant term $1 - \tau + \Delta > 0$. The coefficient of the linear term

$$2 - \tau = -x_6 f'(m_6) - y_6 g'(n_6) > 0, \tag{A45}$$

as both derivatives are negative at E_6. All coefficients of eq. (A27) are therefore positive, so there are zero sign changes and zero roots $\mu > 0$, meaning there are no eigenvalues $\lambda > 1$ (by eq. (A26)). Thus, $0 < \lambda_{1,2} < 1$, and E_6 is a stable node in case *d*.

C.2.8 Case E

In case e, we have both interior fixed-points E_5 and E_6. We will first consider E_5. It is clear that

$$1-\tau+\Delta = x_5\, y_5\, f'(m_5)\, g'(n_5)\,(1-v_1 v_2) > 0 \tag{A46}$$

by the conditions from table 2.2 and table 2.4, so the first Jury condition is always satisfied for E_5 in case e. The second Jury condition is also always satisfied for E_5 in case e.

The third Jury condition is $\Delta < 1$. The expression for the third Jury condition is precisely the same as eq. (A33) from section C.2.4, and indeed the entirety of the analysis is identical to analysis of the third Jury condition for E_5 from case a. We do not repeat it here, and refer the reader back to section C.2.4 for details. Instead, we will simply recall that we can express the boundary of the region of stability for E_5 in terms of v_1 and v_2. This boundary yields a rational function, given by eq. (A36), with two branches. As the bounds on v_2 are the same between case a and case e (see table 2.2), only the left branch is valid for determining the boundary of the region of stability in case e. To one side of this branch, E_5 is stable, and on the other side E_5 is unstable. See fig. 2.4b for illustration of the region of stability for E_5 in case e.

We now turn to the second interior fixed-point, E_6. We see that

$$1-\tau+\Delta = x_6\, y_6\, f'(m_6)\, g'(n_6)\,(1-v_1 v_2) < 0, \tag{A47}$$

by the conditions from table 2.2 and table 2.4, so the first Jury condition is never satisfied for E_6 in case e.

As should now be familiar, we will use Descartes' Rule of Signs to bound the eigenvalues. By the results of analyzing the first Jury condition, at least one eigenvalue is larger than $+1$. Examining the shifted characteristic polynomial (eq. (A27)), we see there is only one sign change between the polynomial's coefficients no matter the sign of $2-\tau$, as the constant term $1-\tau+\Delta < 0$. There is one positive real root μ_1, and thus only one eigenvalue $\lambda_1 > 1$. The other eigenvalue λ_2 must also be real, and as all real eigenvalues are positive for interior fixed-points, we know $\lambda_1 > 1$, $0 < \lambda_2 < 1$. Therefore, E_6 is a saddle point for case e.

C.2.9 Case F

In case *f*, we again have both interior fixed-points E_5 and E_6. We first consider E_5.

Using the conditions and relationships in table 2.2 and table 2.4,

$$1-\tau+\Delta = x_5\, y_5\, f'(m_5)\, g'(n_5)\,(1-v_1 v_2) < 0. \tag{A48}$$

The first Jury condition is never satisfied for E_5 in case *f*. Considering the shifted polynomial eq. (A27), there is one sign change between coefficients of the polynomial and therefore one root $\mu_1 > 0$. Thus, we have only one eigenvalue $\lambda_1 > 1$. As before, the second eigenvalue λ_2 must be real given that λ_1 is real, and we know all real eigenvalues of the interior fixed-points are positive. We find that $\lambda_1 > 1$, $0 < \lambda_2 < 1$, and E_5 is a saddle point for case *f*.

Finally, we consider E_6 for this final case. The first Jury condition is obviously always satisfied as

$$1-\tau+\Delta = x_6\, y_6\, f'(m_6)\, g'(n_6)\,(1-v_1 v_2) > 0 \tag{A49}$$

for E_6 in case *f*, by the conditions from table 2.2 and table 2.4. The second Jury condition is always satisfied.

As with case *d*, we will bound the eigenvalues between 0 and +1 rather than checking the third Jury condition. Recall that in the stability analysis for case *d*, we demonstrated that both eigenvalues associated with E_6 are real for all cases where E_6 exists. Thus, we already know our eigenvalues to be real for E_6 in case *f*.

Employing the oft-used result a final time, we know that since the eigenvalues for E_6 are real, we have $\lambda_{1,2} > 0$. Identically to the analysis for case *d*, we consider the shifted characteristic polynomial eq. (A27). As the first Jury condition is always satisfied for E_6 in this case, the constant term $1-\tau+\Delta > 0$. It is evident that the coefficient of the linear term

$$2-\tau = -x_6 f'(m_6) - y_6 g'(n_6) > 0 \tag{A50}$$

as well. There are zero sign changes between coefficients and therefore zero roots $\mu > 0$. Thus,

there are no eigenvalues $\lambda > 1$ (by eq. (A26)). With this result, we see that $0 < \lambda_{1,2} < 1$, and E_6 is a stable node in case *f*.

The results of the above stability analyses for all six cases with one or more interior fixed-point in the first quadrant are summarized in table 2.3. This appendix completes our analytic stability analysis; analyses of the global bifurcations present in cases *a* and *e* were performed numerically.

Chapter 3

BLOCK-PULSE INTEGRODIFFERENCE EQUATIONS

3.1 Introduction

In recent decades, integrodifference equations (IDEs) have become a popular tool for analyzing the spatial dynamics of biological populations. They have been used to explore many problems in spatial ecology, including estimating speeds of invasion (e.g., Kot et al. [65], Wang et al. [143], Gagnon et al. [41]), population persistence on a finite habitat-patch (e.g., Kot and Schaffer [64], Van Kirk and Lewis [139], Reimer et al. [110]), and critical speeds of climate-change-driven range-shifts (e.g., Zhou and Kot [153], Harsch et al. [47], Cobbold and Stana [23]).

IDEs are spatially nonlocal models [71] that are discrete in time and continuous in space. They are especially useful for modeling the dynamics of species that have non-overlapping generations and distinct growth and dispersal stages [64, 84]. The basic IDE for a population with discrete and nonoverlapping generations is

$$n_{t+1}(x) = \int_{\Omega} k(x,y)\, g[n_t(y)]\, dy, \tag{3.1}$$

where $n_t(x)$ is the population density in generation t at a spatial location x, Ω is the spatial domain, $k(x,y)$ is the dispersal kernel, and $g[n_t(y)]$ is the growth or recruitment function. Population density is mapped from the current generation to the next in two distinct phases. First, the population grows, while remaining fixed in space. In particular, $g[n_t(y)]$ gives the new population-density at location y after growth has occurred. After growth, individuals disperse, relocating from starting location y to new location x with probability governed by $k(x,y)$. The dispersal kernel is a probability density function for the final location x of the individuals.

In contrast to reaction-diffusion models, which are continuous in both time and space, IDE

models account for seasonal growth and can incorporate a variety of dispersal patterns, including long-distance dispersal [76]. The ability to choose a dispersal kernel that best fits the population being modeled is a key feature of IDEs. As a result, IDE models have the advantage of increased ecological realism, as many species possess the features of seasonal growth and long-distance dispersal [98, 3, 65, 84].

Despite the advantages of IDEs, these models have drawbacks as well. IDEs can be computationally expensive since, as for most spatially nonlocal models, individuals may disperse long distances [84]. At the extreme end of this spatial complexity, under certain conditions, a propagule may start from any location in the spatial domain of the model and disperse to any other location in that domain.

In addition, it is often difficult to write down exact solutions for the equilibria or to perform general analytical explorations, except in certain special cases [64, 153, 12, 84]. This analytic difficulty arises because finding equilibria amounts to finding functions that are fixed points of nonlinear integral equations. Finally, most analyses of IDEs lack information about unstable equilibria, as unstable equilibria do not show up in standard numerical experiments. While an argument may be made that it is more relevant to focus on (asymptotically) stable equilibria, in the interest of a complete characterization of the model it would be useful to observe all equilibria.

In order to circumvent some of these difficulties in analyzing IDE models, a number of tools have been developed to approximate or simplify the original model. Special cases, such as an IDE model with a separable kernel or with the Laplace kernel, may allow for analytical results [64, 153, 12, 84]. Other tools for analyzing IDE models involve various approximations of the dispersal kernel, which can be used to approximate steady states and eigenvalues of IDEs, and may be employed for models with one or more species. These methods include average dispersal-success [139, 140, 35], modified average dispersal-success [110], and geometric symmetrization [63, 102, 113, 114, 89].

In this chapter, we present a new method for analyzing the population dynamics of a single

species confined to a finite spatial domain. In contrast to the methods discussed above, which approximate the dispersal kernel, we develop a complementary approach by approximating the growth function. Drawing inspiration from early work by Mark Lewis on the infinite-domain problem [65] and more recent developments by Otto [99] and Nestor and Li [96], we use a piecewise-constant function to approximate the growth function. We refer to the IDE with this approximated growth as a block-pulse IDE. An m-step block-pulse IDE has m terms, or steps, in the block-pulse approximation. This terminology does not preclude using block-pulse approximations for the dispersal kernel as well; indeed, many applications of block-pulse methods for solving other integral problems involve approximating the entire integrand rather than a single component [56, 7].

The piecewise-constant nature of the growth function makes the block-pulse IDE simple and analytically tractable. This formulation of the IDE removes many of the analytical barriers mentioned earlier and also offers numerical advantages. Furthermore, this method is applicable to a broad set of growth functions, including growth functions with Allee effects. An Allee effect, or depensation, occurs when a population's per-capita recruitment increases, with density, at low densities [1, 74]. Integrodifference equations with Allee effects have, historically, been challenging to analyze [84]. However, the block-pulse method allows us to analyze both simple forms of growth, like compensatory growth, as well as challenging forms of growth, such as depensatory growth.

In section 3.2, we present an overview of block-pulse series and how they are used to approximate a growth function. In section 3.3, we lay out the block-pulse IDE model and discuss assumptions and characteristics of the model, including a general closed-form analytic expression for the iterates of the spatial population-distributions. In section 3.4, we perform formal analyses of one-, two-, and three-step block-pulse IDEs, with explicit expressions for the equilibrium solutions, stability and bifurcation analyses, and exploration of parameter space. In section 3.5, we generalize the analytic results of section 3.4 to explore an m-step block-pulse IDE subject first to compensatory Beverton-Holt dynamics and then to growth with a depensatory Allee effect. Section 3.5 is the most applied section and the applied reader may find it useful to look at this section

before returning to section 3.4. In section 3.6, we describe the implications of our results and discuss future research.

While this work began as a way to analyze population dynamics on a finite domain, and particularly with an Allee effect, the dynamics inherent in the models proved to be compelling on their own. In scenarios with a larger number of steps in the block-pulse series, we find that the block-pulse IDE model offers a good approximation to the original model. Furthermore, the block-pulse IDE model also brings significant analytical advantages and an improvement in numerical efficiency for a reasonable number of steps. The framework outlined here provides a simple, effective means of exploring population dynamics in a finite-domain IDE, and offers a novel way to investigate the impact of Allee effects.

3.2 Block-pulse series

3.2.1 Block-pulse functions, series, and properties

Block-pulse functions are an orthogonal set of disjoint functions that have piecewise-constant values. These functions have traditionally been used for a variety of problems in engineering, in particular in systems science and control [109, 56]. Block-pulse functions have been extensively applied to developing numerical and analytical methods for solving a number of integral problems [7, 88, 33, 8]. Block-pulse functions have simple operations and a number of useful properties that make a series of these functions highly useful in studying problems with integrals or derivatives [56].

A set of block-pulse functions $\phi_i(n_t), i = 1,2,...,m$ is conventionally defined on the interval $n_t \in [0,N)$ as

$$\phi_i(n_t) = \begin{cases} 1, & (i-1)h \leq n_t < ih \\ 0, & \text{otherwise,} \end{cases} \tag{3.2}$$

where $h = N/m$ and m is some positive number corresponding to the total number of steps in the block-pulse series. Block-pulse functions are disjoint and orthogonal with each other, and

they form a complete basis for real, bounded, square-integrable functions on the interval $[0,N)$ as $m \to \infty$ [109, 56].

Based on these properties, we can expand any real, bounded, continuous function $g(n_t)$ that is square integrable over the domain $n_t \in [0,N)$ into a block-pulse series. The functions $g(n_t)$ that we consider describe population growth, and so we choose the upper domain-limit N to be a population limit governed by the carrying capacity of the population. An m-step block-pulse series for the function $g(n_t)$ is

$$g(n_t) \approx \sum_{i=1}^{m} g_i \phi_i(n_t), \quad i = 1,2,...,m, \tag{3.3}$$

where g_i is the block-pulse coefficient for the ith block-pulse function $\phi_i(n_t)$. Each coefficient g_i is simply the average value of the function $g(n_t)$ over the ith subinterval, so that

$$g_i = \frac{1}{h} \int_{(i-1)h}^{ih} g(n_t)\, dn_t. \tag{3.4}$$

As each function $\phi_i(n_t)$ is disjoint from the others, the series in eq. (3.3) is thus a piecewise-constant approximation to the original function $g(n_t)$, with the value of the constants governed by the original function. The block-pulse series will converge pointwise to the original function as the number of steps $m \to \infty$ [56].

3.2.2 Block-pulse approximations to a growth function

To illustrate the block-pulse approximation method, consider a strictly-increasing growth-function,

$$g(n_t) = \frac{\left[\left(1+\rho^2\right)/K\right] n_t^2}{1+(\rho/K)^2 n_t^2}, \tag{3.5}$$

with an Allee effect, defined on the interval $n_t \in [0,N)$ with growth parameter ρ and carrying capacity K, where $N = K = 1$. In the nonspatial model with this growth function, there are three equilibria $n_{t+1} = n_t = n$, two stable fixed-points at $n = 0$ and $n = K$ and one unstable fixed-point, the Allee threshold, at $n = K/\rho^2$.

To compare the original growth-function with its block-pulse series, we choose five steps for our approximation. The five-step block-pulse series is given by

$$g(n_t) \approx \begin{cases} g_1, & 0 \leq n_t < N/5 \\ g_2, & N/5 \leq n_t < 2N/5 \\ g_3, & 2N/5 \leq n_t < 3N/5 \\ g_4, & 3N/5 \leq n_t < 4N/5 \\ g_5, & 4N/5 \leq n_t < N, \end{cases} \tag{3.6}$$

with $g_i < g_{i+1}$ for $i = 1,2,3,4$. Each coefficient g_i is the density of recruits or the growth level when the population density n_t is within the given limits. The population densities $iN/5$ are density thresholds. Passing through each threshold leads to a change in the level of recruitment.

Figure 3.1 shows the Allee growth-function along with its five-step block-pulse approximation. At each of the density thresholds, we see that the growth function jumps to the next level of recruitment. With this illustration of the block-pulse method in place, we now turn to the block-pulse IDE itself.

3.3 Block-pulse IDE

We begin by examining the model from eq. (3.1), where the population is confined to a finite, stationary, one-dimensional patch of habitat of length L such that $\Omega = [-L/2,\ L/2]$. We assume that habitat outside the patch is hostile and that individuals that disperse outside of the patch do not reproduce. For subsequent mathematical simplicity, we assume that the growth function $g[n_t(y)]$ is strictly increasing. We also assume that dispersal is homogeneous and isotropic. Thus, the dispersal kernel is symmetric and can be rewritten as a difference kernel, $k(x,y) = k(x-y)$. This difference kernel may be interpreted as a probability density function for the displacement of individuals in the population.

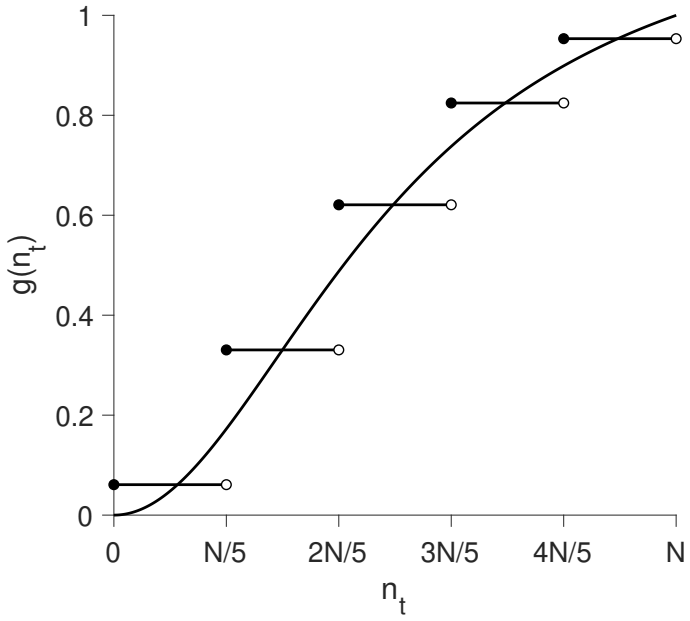

Fig. 3.1 The Allee growth-function from eq. (3.5) with the five-step block-pulse approximation from eq. (3.6). Parameters are $\rho = 2$, $K = 1$, $N = 1$, and the five growth-levels are $g_1 \approx 0.06$, $g_2 \approx 0.33$, $g_3 \approx 0.62$, $g_4 \approx 0.82$, $g_5 \approx 0.95$.

Under these assumptions, the model from eq. (3.1) can be written as

$$n_{t+1}(x) = \int_{-L/2}^{L/2} k(x-y)\, g[n_t(y)]\, dy. \tag{3.7}$$

The population density at location x in the next generation $t+1$, $n_{t+1}(x)$, is thus given by the convolution of a growth function with a dispersal kernel. We primarily use the Laplace distribution for our dispersal kernel as it accounts for some long-distance dispersal and possesses a number of useful properties. At the same time, our approach is not limited to this distribution (see section 3.5.2).

We assume that our initial population-distribution is symmetric and unimodal. Though we recognize that such an assumption may not be true in general in nature, for the time being we make this assumption for mathematical simplicity. Applying an increasing growth-function to a symmetric and unimodal distribution will result in a symmetric and unimodal population-distribution after growth. We also assume that the dispersal kernel is unimodal. Thus, we are taking the con-

volution of two symmetric, unimodal distributions, which will also be symmetric and unimodal [150, 30, 105]. Many dispersal kernels satisfy the conditions of being symmetric and unimodal, including the popular Gaussian, Laplace, and Cauchy kernels. Using these assumptions, the population distributions given by the model will always be symmetric and unimodal, with the maximum population-density occurring at the center of the patch at $x = 0$ and the minimum population-density occurring at the edges of the patch at $x = \pm L/2$.

With these assumptions in hand, we consider an m-step block-pulse IDE. This IDE, with its growth function given by a block-pulse series, may be written as

$$\begin{aligned} n_{t+1}(x) &= \int_{-L/2}^{L/2} k(x-y) \sum_{i=1}^{m} g_i \phi_i [n_t(y)] \, dy \\ &= \sum_{i=1}^{m} g_i \int_{-L/2}^{L/2} k(x-y) \, \phi_i [n_t(y)] \, dy. \end{aligned} \tag{3.8}$$

As mentioned in section 3.2.2, the coefficients g_i are different growth levels. As we have assumed our growth function to be strictly increasing, we have $g_i < g_{i+1}$ for $i = 1, 2, ..., m-1$.

Recall that each block-pulse function ϕ_i is nonzero only over a limited spatial region where it is equal to one. We may expand eq. (3.8) into a sum of at most $2m-1$ integrals, where each integral is defined only over the spatial region(s) where $\phi_i \neq 0$ for each i. The boundaries of each region, $x = \pm r_{i,t}$, are the spatial thresholds where the population threshold is reached, such that $n_t(\pm r_{i,t}) = ih$. After expanding eq. (3.8), using a change of variables $u = x - y$, and rewriting the resulting integrals in terms of cumulative distribution functions, we obtain the simple expression

$$\begin{aligned} n_{t+1}(x) = {} & g_1 [F(x + L/2) - F(x - L/2)] \\ & + (g_2 - g_1) [F(x + r_{1,t}) - F(x - r_{1,t})] + ... \\ & + (g_m - g_{m-1}) [F(x + r_{m-1,t}) - F(x - r_{m-1,t})], \end{aligned} \tag{3.9}$$

or

$$n_{t+1}(x) = g_1 \left[F(x+L/2) - F(x-L/2)\right] + \sum_{i=1}^{m-1} (g_{i+1} - g_i) \left[F(x+r_{i,t}) - F(x-r_{i,t})\right], \tag{3.10}$$

where $F(x)$ is the cumulative distribution function (CDF) of a probability density function $k(z)$, defined as

$$F(x) = \int_{-\infty}^{x} k(z)\, dz. \tag{3.11}$$

We note that reducing our IDE model to eq. (3.9) or eq. (3.10) amounts to approximating a Riemann–Stieltjes integral with a Riemann–Stieltjes sum. Due to Arzelà's (or Osgood's) bounded convergence theorem [49, 87, 4, 93, 94], this series has nice convergence properties as $m \to \infty$ (see appendix D.3 for details).

The symmetry of the spatial thresholds $x = \pm r_{i,t}$ occurs because we have assumed our population distributions to be symmetric and unimodal. Thus, each spatial threshold where the population passes through a density threshold will occur twice in a symmetric fashion, if it occurs at all. We have $r_{i,t} > r_{i+1,t}$, with the t subscript denoting the time dependence of the spatial thresholds.

For this general example, we have assumed that the population passes through all density thresholds inside of the patch $[-L/2, L/2]$ and sees all m growth levels. Note that the population may fail to pass through a density threshold or may pass through it at a spatial threshold outside of the patch, in which case eq. (3.10) has fewer terms.

We now have a model that is expressed entirely in terms of cumulative distribution functions, so that we have explicit analytic expressions for the entire spatial population-distribution in the next generation. This makes the block-pulse IDE analytically and numerically approachable, and the CDF form of the IDE is immensely useful. We now turn to a formal analysis of one-, two-, and three-step block-pulse IDEs.

3.4 Analytical results

As seen above, the block-pulse IDE may be rewritten into a remarkably simple form. Given the assumptions laid out in section 3.3, block-pulse IDEs are a class of models with much more analytical tractability than most IDE models. We will now explore explicit equilibrium solutions and their regions of validity in parameter space, stability of equilibria, and bifurcations in one-, two-, and three-step block-pulse IDEs.

Throughout the rest of this chapter, we will illustrate examples using the Laplace kernel and its CDF, though the general trends we observe hold for other dispersal kernels satisfying our assumptions as well (see section 3.5.2). The probability density function for the Laplace distribution is

$$k(z) = \frac{1}{2}\alpha e^{-\alpha|z|}, \tag{3.12}$$

and the cumulative distribution function is

$$F(z) = \begin{cases} \frac{1}{2}e^{\alpha z}, & z < 0 \\ 1 - \frac{1}{2}e^{-\alpha z}, & z \geq 0, \end{cases} \tag{3.13}$$

where $1/\alpha$ is the average dispersal-distance of the population.

3.4.1 One-step block-pulse IDE

The one-step block-pulse IDE has a growth function approximated by the single constant

$$g(n_t) \approx g_1, \quad 0 \leq n_t < N. \tag{3.14}$$

The corresponding block-pulse IDE is

$$\begin{aligned} n_{t+1}(x) &= g_1 \int_{-L/2}^{L/2} k(x-y)\, dy \\ &= g_1 \left[F(x+L/2) - F(x-L/2)\right], \end{aligned} \tag{3.15}$$

where the second equality is obtained after using the same change of variables, $u = x - y$, and method of rewriting the integral in terms of cumulative distribution functions as in section 3.3.

It is clear from eq. (3.15) that the population reaches its carrying capacity in one generation and stays there for all time t, regardless of the initial density of the population. We thus have a stable equilibrium at

$$n(x) = g_1 \left[F(x + L/2) - F(x - L/2) \right]. \tag{3.16}$$

The shape of the equilibrium distribution is simply the difference between two shifted cumulative distribution functions, as shown in fig. 3.2.

This equilibrium is valid for $n(x) < N$. Since the maximum population-density occurs at $x = 0$ we thus require $n(0) < N$ for existence of the equilibrium. Substituting $x = 0$ into eq. (3.16) and rearranging, we thus need

$$g_1 < \frac{N}{F(L/2) - F(-L/2)}. \tag{3.17}$$

3.4.2 Two-step block-pulse IDE

The growth-function approximation for the two-step block-pulse IDE is

$$g(n_t) \approx \begin{cases} g_1, & 0 \leq n_t < N/2 \\ g_2, & N/2 \leq n_t < N, \end{cases} \tag{3.18}$$

with $g_1 < g_2$. The population density $n_t = N/2$ is a density threshold. Below the threshold, the population grows to g_1, and above it, recruitment jumps to g_2. This growth function is illustrated in fig. 3.3a.

We expect three equilibrium solutions of the block-pulse IDE – one with a low growth-level everywhere in the patch, one with a high growth-level everywhere in the patch, and one with both growth-levels in the patch. We suspect initially that the two one-growth-level equilibria, those with a single growth-level in the patch, should be stable.

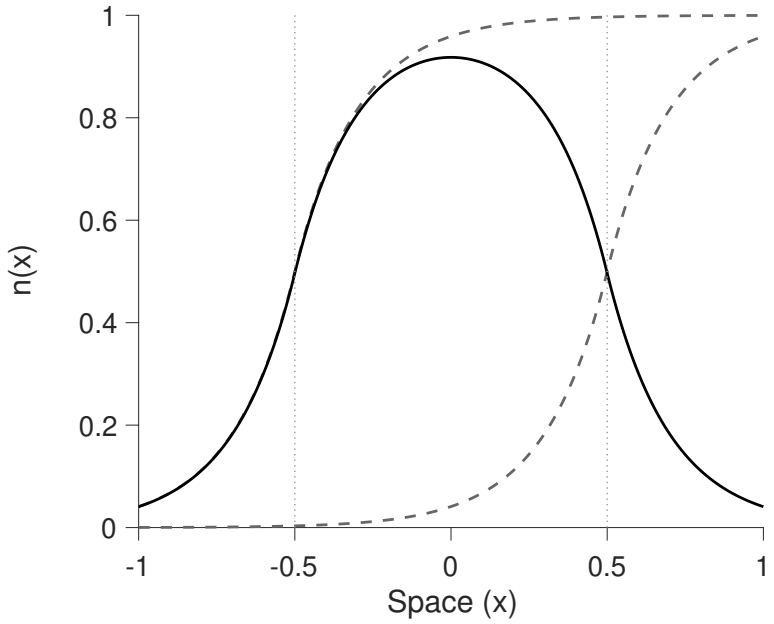

Fig. 3.2 The equilibrium distribution from eq. (3.16) (solid) along with the two component cumulative distribution functions (dashed). The left dashed distribution is the first term $F(x+L/2)$, the right dashed distribution is the second term $F(x-L/2)$. Vertical dotted lines indicate the spatial domain $x \in [-L/2, L/2]$. Parameters are $L = 1$, $N = 1$, $g_1 = 1$, $\alpha = 5$.

While the analysis for the one-step model was trivial, the two-step model contains more interesting dynamics. Depending on the location and existence of the spatial-threshold points $x = \pm r_{1,t}$ where $n(\pm r_{1,t}) = N/2$, the equilibrium solution to the two-step block-pulse IDE may take on one of three different forms, matching our initial intuition. These three cases are addressed separately in the following sections.

Low equilibrium

In the first case, the population never attains the density threshold of $N/2$. The population grows at the low level g_1 everywhere and the spatial thresholds do not exist. The corresponding IDE can

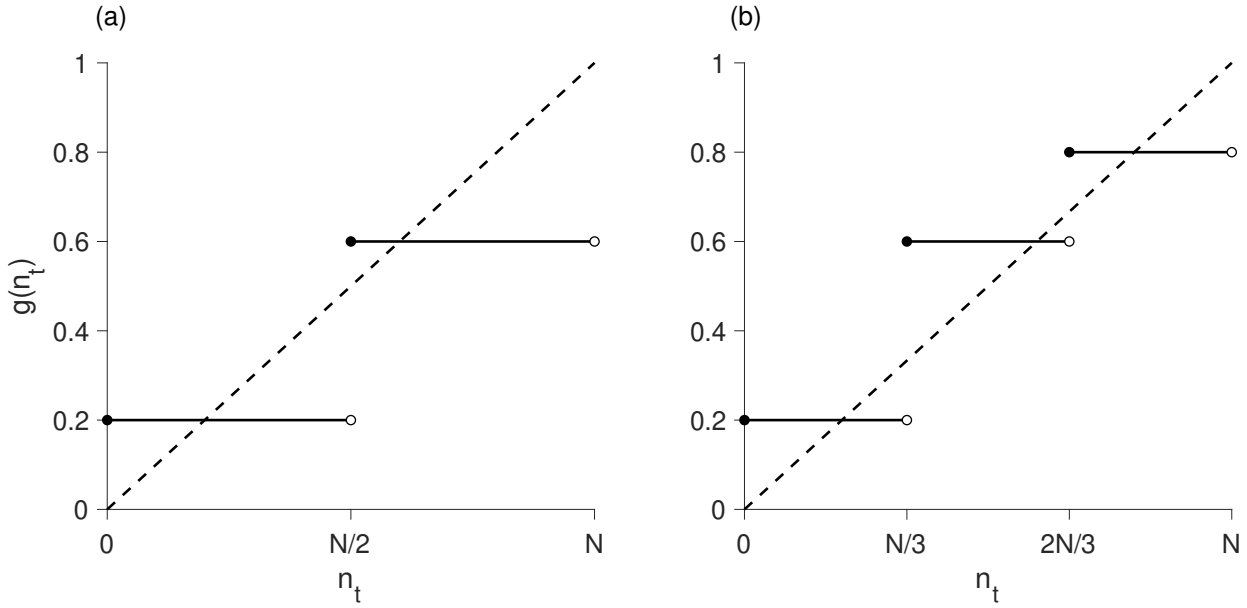

Fig. 3.3 Block-pulse growth-functions with **a** two steps and **b** three steps. The growth functions (solid) are overlaid on the line of equality (dashed). Parameter values are $N = 1$, $g_1 = 0.2$, $g_2 = 0.6$, $g_3 = 0.8$.

be written as

$$\begin{aligned} n_{t+1}(x) &= g_1 \int_{x-L/2}^{x+L/2} k(z)\, dz \\ &= g_1 \left[F(x+L/2) - F(x-L/2) \right]. \end{aligned} \tag{3.19}$$

It is clear that the population distribution in eq. (3.19) is always the same regardless of t. Thus, there is a stable equilibrium, which we call the low equilibrium, at

$$n(x) = g_1 \left[F(x+L/2) - F(x-L/2) \right]. \tag{3.20}$$

This is a valid equilibrium so long as $n(0) < N/2$, at which point we would transition into a bridge equilibrium (section 3.4.2). Substituting $x = 0$ into eq. (3.20) and rearranging to solve for the growth level gives a condition of

$$g_1 < \frac{N/2}{F(L/2) - F(-L/2)} = g_a. \tag{3.21}$$

Figure 3.4 illustrates the region in parameter space where this equilibrium is valid.

High equilibrium

In the second case, the population is above $N/2$ everywhere in the patch and grows at high level g_2 inside the patch. The spatial thresholds exist outside the patch, so that

$$-r_{1,t} < -L/2 < L/2 < r_{1,t}. \tag{3.22}$$

The IDE in this case is

$$\begin{aligned} n_{t+1}(x) &= g_2 \int_{x-L/2}^{x+L/2} k(z)\, dz \\ &= g_2 \left[F(x+L/2) - F(x-L/2)\right]. \end{aligned} \tag{3.23}$$

The only difference between this mapping and the mapping in eq. (3.19) is replacing g_1 with g_2.

The population distribution does not change regardless of t. There is a stable equilibrium, called the high equilibrium, given by

$$n(x) = g_2 \left[F(x+L/2) - F(x-L/2)\right]. \tag{3.24}$$

In order for this to be a valid equilibrium, it must be above $N/2$ everywhere in the patch, or $n(L/2) > N/2$. Substituting $x = L/2$ into eq. (3.24) and simplifying, we require

$$g_2 > \frac{N/2}{F(L) - F(0)} = g_b. \tag{3.25}$$

We also require $n(0) < N$, or

$$g_2 < \frac{N}{F(L/2) - F(-L/2)} = g_c. \tag{3.26}$$

Thus, for $g_b < g_2 < g_c$ there is a stable high-equilibrium. See fig. 3.4 for an illustration of the region of validity.

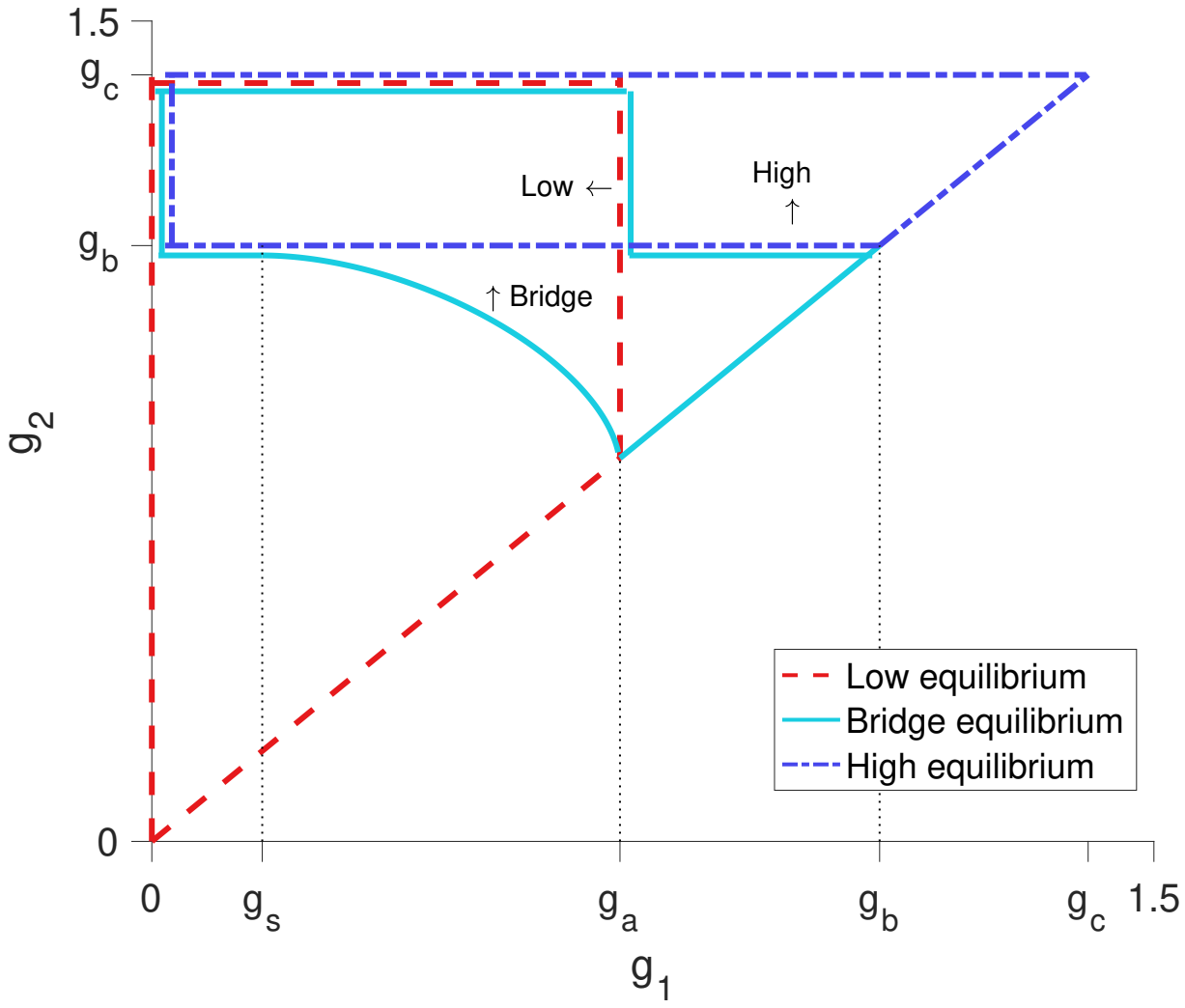

Fig. 3.4 Regions of validity in parameter space for the three equilibrium forms. All equilibria are invalid for $g_1 \geq g_2$. The low equilibrium is valid inside the dashed region, the high equilibrium is valid inside the dashed-dotted region, and the bridge equilibrium is valid inside the solid region. Vertical dotted lines indicate the boundaries in g_1 that lead to different behaviors of the bridge equilibrium. For $g_s < g_1 < g_a$, as g_2 increases through the lower boundary for the bridge-equilibrium region, a fold bifurcation occurs, resulting in two bridge equilibria for g_2 values above the boundary and below g_b. At g_b, the upper bridge-equilibrium becomes a high equilibrium. Parameter values are $L = 0.5$, $N = 1$, $\alpha = 5$, $g_s \approx 0.17$, $g_a \approx 0.7$, $g_b \approx 1.1$, $g_c \approx 1.4$.

Bridge equilibrium

The third case occurs when the population distribution inside the patch is both above and below $N/2$, so that the population sees both growth levels inside the patch. The spatial thresholds are inside the patch, with

$$-L/2 < -r_{1,t} < r_{1,t} < L/2. \tag{3.27}$$

The IDE now takes the form

$$n_{t+1}(x) = g_1 \int_{x+r_{1,t}}^{x+L/2} k(z)\,dz + g_2 \int_{x-r_{1,t}}^{x+r_{1,t}} k(z)\,dz + g_1 \int_{x-L/2}^{x-r_{1,t}} k(z)\,dz, \tag{3.28}$$

which simplifies to the mapping

$$\begin{aligned} n_{t+1}(x) =& g_1 \left[F(x+L/2) - F(x-L/2)\right] \\ &+ (g_2 - g_1)\left[F(x+r_{1,t}) - F(x-r_{1,t})\right]. \end{aligned} \tag{3.29}$$

Given $n_{t+1}(x)$, we can compute the next spatial threshold $r_{1,t+1}$. That is, we have an implicit $r_{1,t}$ mapping from $r_{1,t}$ to $r_{1,t+1}$ given by

$$\begin{aligned} n_{t+1}(r_{1,t+1}) =& g_1 \left[F(r_{1,t+1}+L/2) - F(r_{1,t+1}-L/2)\right] \\ &+ (g_2 - g_1)\left[F(r_{1,t+1}+r_{1,t}) - F(r_{1,t+1}-r_{1,t})\right] = N/2, \end{aligned} \tag{3.30}$$

where we have used the fact that $n_{t+1}(r_{1,t+1}) = N/2$. This map is illustrated in fig. 3.5.

The fixed points of this map occur when $r_{1,t+1} = r_{1,t} = r_1$, so that

$$g_1 \left[F(r_1+L/2) - F(r_1-L/2)\right] + (g_2 - g_1)\left[F(2r_1) - F(0)\right] = N/2. \tag{3.31}$$

These fixed points are evident in fig. 3.5 as the intersections of the $r_{1,t}$ mapping with the line of equality. When the spatial threshold is at a fixed point r_1, the entire population-distribution is at equilibrium so that $n_{t+1}(x) = n_t(x) = n(x)$. Substituting the fixed point r_1 into eq. (3.29), we therefore have an equilibrium population-distribution, which we call the bridge equilibrium, at

$$\begin{aligned} n(x) =& g_1 \left[F(x+L/2) - F(x-L/2)\right] + (g_2 - g_1)\left[F(x+r_1) - F(x-r_1)\right]. \end{aligned} \tag{3.32}$$

The number of spatial-threshold fixed-points and their stability corresponds to the number and stability of the bridge equilibria.

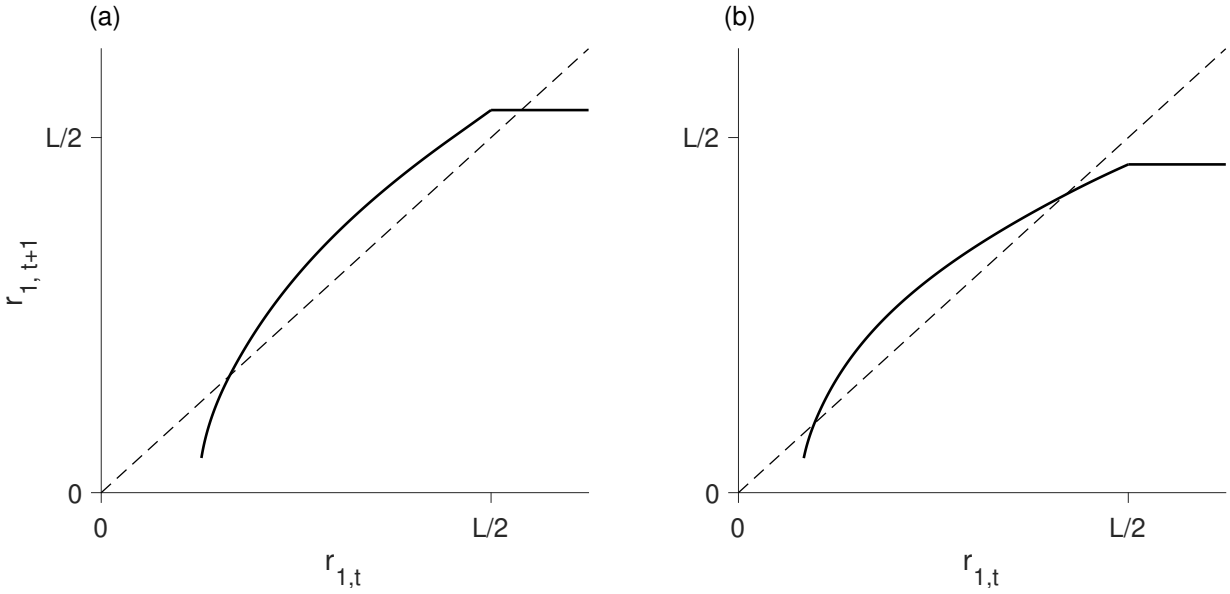

Fig. 3.5 Spatial-threshold mapping from eq. (3.30) (solid curve for $r_{1,t} < L/2$) for two different parameter sets with **a** one fixed point and **b** two fixed points. The solid horizontal line for $r_{1,t} > L/2$ is an equivalent $r_{1,t} - r_{1,t+1}$ mapping for the high map; as the high map does not depend on $r_{1,t}$ the corresponding $r_{1,t+1}$ is constant regardless of $r_{1,t}$. Using stability of the spatial-threshold fixed-points as a proxy for stability of the full equilibrium distributions, in **a**, the high equilibrium is stable and the bridge equilibrium is unstable; in **b** the lower bridge-equilibrium is unstable and the upper bridge-equilibrium is stable. Given a particular $r_{1,t}$ in the implicit map from eq. (3.30), $r_{1,t+1}$ was computed with the bisection method. Parameter values are $L = 0.5$, $N = 1$, $\alpha = 5$, **a** $g_1 = 0.4$, $g_2 = 1.2$; **b** $g_1 = 0.6$, $g_2 = 1$.

The bridge equilibrium will be valid for $n(L/2) < N/2 < n(0) < N$. To facilitate analysis of the bridge equilibrium, we solve for g_2 in eq. (3.31) to obtain

$$g_2 = \frac{N/2 - g_1 \left[F\left(r_1 + L/2\right) - F\left(r_1 - L/2\right) - F\left(2r_1\right) + F\left(0\right)\right]}{F\left(2r_1\right) - F\left(0\right)}. \tag{3.33}$$

The bridge equilibrium may be characterized based on the behavior of this function for g_2. In particular, we will focus on the range of g_2 for which the bridge equilibrium is valid, as well as

the number of bridge equilibria. The number of bridge equilibria corresponds to the number of solutions r_1 for a given g_2 in eq. (3.33), i.e., the number of fixed points r_1 for a given g_2.

To classify the range of valid g_2 values for the bridge equilibrium, we first observe that the bridge equilibrium meets the low equilibrium at $r_1 = 0$. Using eq. (3.33), we see that g_2 will then go to $\pm\infty$ depending on the value of g_1. In particular, for $g_1 < g_a$, $g_2 \to \infty$ while, for $g_1 > g_a$, $g_2 \to -\infty$. Next, we observe that the bridge equilibrium meets the high equilibrium at $r_1 = L/2$ and $g_2 = g_b$ (see eq. (3.25) and fig. 3.4). These two observations make it clear that eq. (3.33) may have one or two branches (see fig. 3.6). As a result, there may be either one or two bridge-equilibria. Whether eq. (3.33) is single- or multi-valued also depends on the relative size of g_1. Combined with the behavior of g_2 in eq. (3.33) as $r_1 \to 0$, there are three distinct parameter regimes with differing behavior of the bridge equilibria, summarized in table 3.1.

For small g_1, the function for g_2 is single-valued, with $g_2 \to \infty$ as mentioned above (see fig. 3.6a,b). Thus, there is a single bridge-equilibrium that is valid for $g_2 > g_b$.

The function for g_2 becomes multivalued as g_1 increases through the limit

$$g_1 = \frac{Nk(L)}{[F(L) - F(0)][k(L) + k(0)]} = g_s. \tag{3.34}$$

As this is a switching point of the bridge equilibrium, rather than a point where two equilibria meet, we use the subscript s for 'switch.' We still have $g_2 \to \infty$, but there are two solutions r_1 for some $g_2 < g_b$ and a single solution for $g_2 > g_b$ (see fig. 3.6c,d). Therefore we have two bridge-equilibria with distinct spatial thresholds for some $g_2 < g_b$; for $g_2 > g_b$ only one bridge equilibrium remains. For both prior cases in which $g_2 \to \infty$, to guarantee that $n(0) < N$ the true upper limit in g_2 is g_c.

As g_1 increases further through g_a, the function becomes single-valued, but now $g_2 \to -\infty$ (see fig. 3.6e,f). In practice, the lower bound on g_2 is g_1. There is once again a single bridge-equilibrium valid for $g_1 < g_2 < g_b$.

These parameter regimes for the bridge equilibrium are illustrated in fig. 3.4. These limits also encompass the restrictions that $n(L/2) < N/2 < n(0) < N$. In fig. 3.4, note that for $g_s < g_1 < g_a$, increasing g_2 through the lower boundary of validity corresponds to a fold bifurcation leading to

the emergence of two bridge-equilibria. The three behaviors of the bridge equilibrium are further demonstrated in the bifurcation diagrams of fig. 3.6, showing both the maximum and minimum densities of the equilibria as g_2 varies for different g_1 values.

Table 3.1 Number of bridge equilibria in different parameter regions. If there is no entry in a particular row or column, there is no valid solution to eq. (3.33) and therefore no bridge equilibrium in that region.

	$g_1 < g_2 < g_b$	$g_b < g_2 < g_c$
$0 < g_1 < g_s$		One bridge-equilibrium
$g_s < g_1 < g_a$	Two bridge-equilibria for some $g_2 < g_b$[1]	One bridge-equilibrium
$g_a < g_1 < g_2$	One bridge-equilibrium	

[1] We have no analytical expression for the lower bound in g_2 when g_2 has two branches. There is, however, a numerically calculable lower bound in g_2. See fig. 3.4 for a graphical representation of this lower bound.

To complete the characterization of the bridge equilibria, we would like to classify their stability. To accomplish this, we return to the spatial-threshold map given by eq. (3.30). As noted earlier, the stability of the spatial-threshold fixed-point corresponds to the stability of the entire spatial equilibrium. Using the spatial-threshold map, we can classify stability as with any difference equation. We differentiate the map with respect to $r_{1,t}$. Denoting $r_1' = dr_{1,t+1}/dr_{1,t}$, after evaluating the derivative at the fixed point r_1 we obtain

$$r_1' = \frac{(g_1 - g_2)\,[k(2r_1) + k(0)]}{g_1\,[k(r_1 + L/2) - k(r_1 - L/2)] + (g_2 - g_1)\,[k(2r_1) - k(0)]}. \tag{3.35}$$

If the magnitude of the derivative is smaller than $+1$, the equilibrium distribution is stable, otherwise it is unstable.

In general, we find that when $g_1 < g_s$, the bridge equilibrium is unstable. This scenario is shown in the bifurcation diagrams in fig. 3.6a,b, where there is a single branch of bridge equilibria for $g_b < g_2 < g_c$. In contrast, when $g_1 > g_a$ the bridge equilibrium is stable (fig. 3.6e,f).

For $g_s < g_1 < g_a$, there is a fold bifurcation at some critical g_2 value, corresponding to the r_1 value where $r_1' = 1$ (fig. 3.6c,d). In particular, the lower boundary for the bridge equilibrium

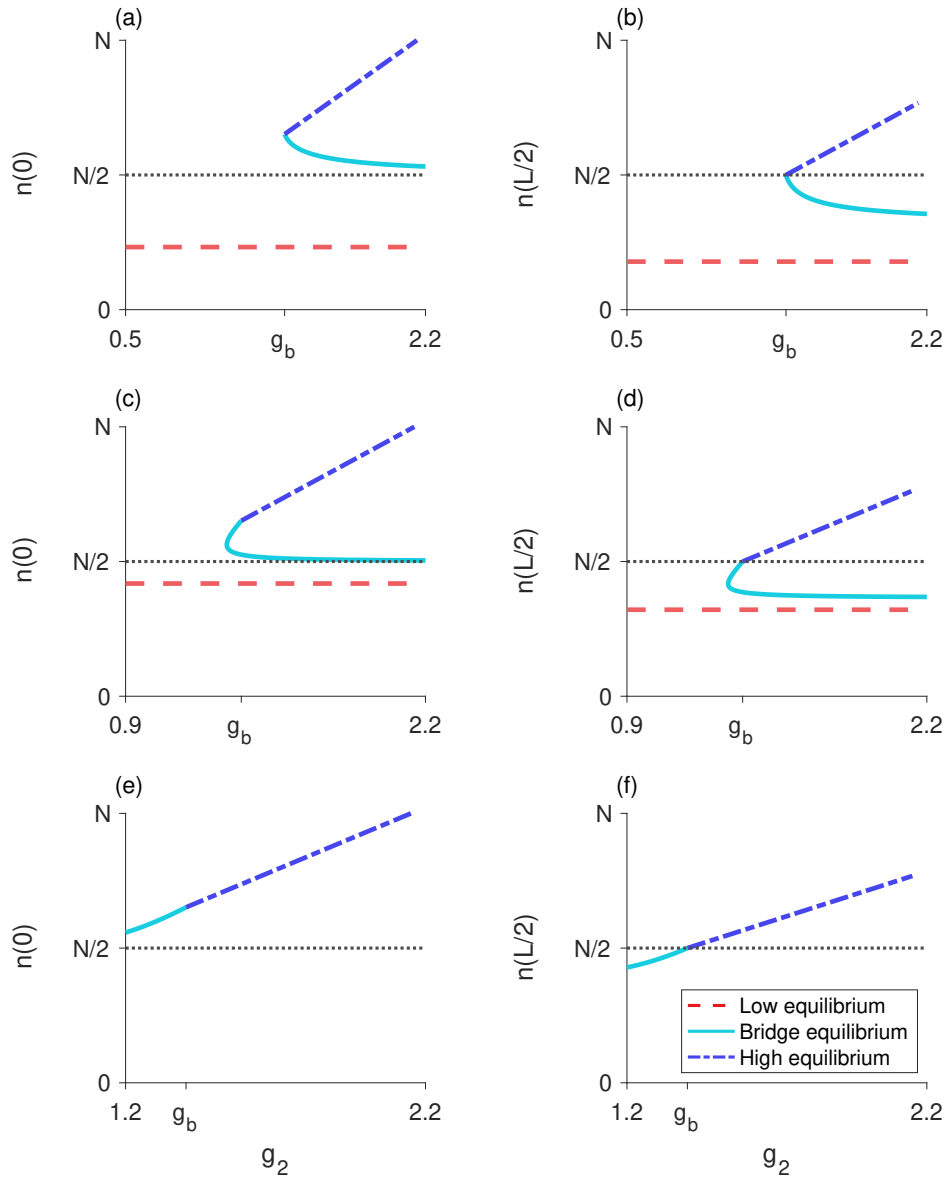

Fig. 3.6 Bifurcation diagram as g_2 varies for three different values of g_1. The left column (**a, c, e**) plots the maximum population-density $n(0)$ and the right column (**b, d, f**) plots the minimum population-density $n(L/2)$. The horizontal dotted line is the density-threshold value $N/2$. (**a, b**), $g_1 = 0.5$ and $g_1 < g_s$; there is a single unstable bridge-equilibrium valid for $g_b < g_2 < g_c$. (**c, d**), $g_1 = 0.9$ and $g_s < g_1 < g_a$; the upper branch of bridge equilibria are stable and the lower branch of bridge equilibria are unstable. (**e, f**), $g_1 = 1.2$ and $g_a < g_1 < g_2$; there is a single stable bridge-equilibrium valid for $g_1 < g_2 < g_b$. Both the low and high equilibria are stable. Parameter values are $L = 0.25$, $N = 1$, $\alpha = 5$, $g_s \approx 0.6$, $g_a \approx 1.1$, $g_b \approx 1.4$, $g_c \approx 2.2$.

when $g_s < g_1 < g_a$ shown in fig. 3.4 demarcates this fold bifurcation. For g_2 below the boundary, there is no bridge equilibrium; for g_2 above this boundary and below g_b, there are two bridge-equilibria. The bridge equilibrium with the larger r_1 fixed point, corresponding to the upper branch in the bifurcation diagram (fig. 3.6c,d), is stable. This upper branch terminates at $g_2 = g_b$, where it becomes a stable high-equilibrium. The bridge equilibrium with the smaller r_1 fixed point, or the lower branch in the bifurcation diagram (fig. 3.6c,d), is unstable. This behavior is also evident in fig. 3.5b where there are two bridge-equilibria. For details of these stability calculations, see appendix A.3.

Two-step block-pulse IDE: conclusions

In general, we see in fig. 3.4 that there are regions in parameter space for which we might have only a single equilibrium, whether low, high, or bridge, as well as regions where two or all three equilibria coexist. With two possible bridge-equilibria, there are four distinct equilibrium-distributions, though only three may ever coexist for a single set of parameters. Bifurcation diagrams for the equilibria with fixed g_1 and varying g_2 are presented in fig. 3.6, showing how the equilibrium distributions meet at the density-threshold values.

The three g_1 values illustrate the different behaviors that the bridge equilibria may exhibit. For small g_1 ($g_1 < g_s$), all three equilibria may coexist. In this scenario, there is something like a fold bifurcation as g_2 increases, leading to the simultaneous emergence of a high equilibrium and a bridge equilibrium (fig. 3.6a,b).

For moderate g_1 ($g_s < g_1 < g_a$), a fold bifurcation results in two bridge-equilibria appearing as g_2 increases. As g_2 increases through g_b, the upper bridge-equilibrium turns into the high equilibrium as the edges of the population distribution rise above the density threshold $N/2$ (fig. 3.6c,d).

For larger g_1 ($g_a < g_1 < g_2$), the low equilibrium does not exist. There is a single branch of equilibria, beginning as a bridge equilibrium and turning into the high equilibrium as g_2 increases (fig. 3.6e,f).

The stability of the different equilibria in this model follows the typical pattern of alternating stability observed in difference equations. That is, stable equilibria never exist next to each other, nor do unstable equilibria. Both of the one-growth-level equilibria, where the growth function crosses the line of equality in fig. 3.3a along a flat constant, are stable. Thus, the analytical stability results for the bridge equilibria from section 3.4.2 can also be inferred from the structure of the equilibria shown in fig. 3.6.

3.4.3 Three-step block-pulse IDE

We perform the same analysis for the three-step model, searching for any patterns that emerge among the three block-pulse models. We will use similar terminology as in section 3.4.2, with the understanding that any repeated notation now refers to the new parameters and points in the three-step model, and not the analogous points from the two-step model. The three-step block-pulse IDE has growth function

$$g(n_t) \approx \begin{cases} g_1, & 0 \leq n_t < N/3 \\ g_2, & N/3 \leq n_t < 2N/3 \\ g_3, & 2N/3 \leq n_t < N, \end{cases} \tag{3.36}$$

with $g_1 < g_2 < g_3$. This growth function is illustrated in fig. 3.3b.

There are two density thresholds, $n_t(x) = N/3$ and $n_t(x) = 2N/3$, with corresponding spatial-threshold points $x = \pm r_{1,t}$ and $x = \pm r_{2,t}$. Depending on the location and existence of these spatial thresholds, there may be six different forms of the analytic map for the three-step block-pulse IDE (and therefore six different forms of equilibrium distributions). Table 3.2 illustrates the six possible orientations of the spatial-threshold points. The population may have a single growth-level in the patch, for three distinct forms, may see two growth-levels in the patch, for two more forms, or may see all three growth-levels inside the patch, for one final form of the IDE.

When discussing the equilibrium distributions for these different forms of the IDE, in general, we refer to an equilibrium solution where the population sees p growth-levels inside the patch as a

p-growth-level equilibrium, or a p-level equilibrium for succinctness. We have $1 \leq p \leq m$, with m the total number of steps in the block-pulse approximation. In the three-step model, $m = 3$, and so we have one-level, two-level, and three-level equilibria.

We will address the one-level, two-level, and three-level equilibria individually at first, before summarizing the overarching dynamics and patterns of the three-step model. As in the two-step model, there are a number of critical threshold-values for the growth levels g_i that correspond to changes in equilibrium behavior. These thresholds are summarized in table 3.3.

Table 3.2 Orientations of the spatial thresholds in the three-step block-pulse IDE, and their corresponding equilibrium type. The configurations are based on if each threshold exists and, if it does, whether it exists inside the patch or outside the patch. If there is no entry, that configuration of thresholds is not possible.

	no $r_{2,t}$	$r_{2,t}$ inside	$r_{2,t}$ outside
no $r_{1,t}$	Low		
$r_{1,t}$ inside	Low bridge	Full bridge	
$r_{1,t}$ outside	Middle	High bridge	High

One-level equilibria: low, middle, and high equilibria

For populations with a single growth-level g_i, $i = 1,2,3$, within the patch, the densities in the patch lie between $(i-1)N/3 < n_t < iN/3$. The corresponding IDEs are

$$\begin{aligned} n_{t+1}(x) &= g_i \int_{x-L/2}^{x+L/2} k(z)\,dz \\ &= g_i \left[F(x+L/2) - F(x-L/2)\right]. \end{aligned} \tag{3.37}$$

Each of these three maps generates a stable equilibrium. These one-level equilibria occur at

$$n(x) = g_i \left[F(x+L/2) - F(x-L/2)\right]. \tag{3.38}$$

For $i = 1,2,3$, we call these the low, middle, and high equilibria.

The low equilibrium is valid so long as the maximum population-density does not exceed $N/3$, where the equilibrium transitions to a low-bridge equilibrium (section 3.4.3). We thus require $n(0) < N/3$, or $g_1 < g_a$, where g_a is given in table 3.3. Figure 3.7a shows the region in parameter space where this equilibrium is valid.

The middle equilibrium is valid if $N/3 < n(L/2) < n(0) < 2N/3$ (see fig. 3.7), or when $g_b < g_2 < g_c$, with g_b and g_c as in table 3.3. Violating the lower boundary pushes the population below $N/3$ at the boundaries and the equilibrium becomes a low-bridge equilibrium (section 3.4.3). Violating the upper boundary moves the population above $2N/3$ at the middle of the habitat and the equilibrium shifts to a high-bridge equilibrium (section 3.4.3).

The high equilibrium is valid when $n(L/2) > 2N/3$ (see fig. 3.7b), so that $g_3 > g_d$. Violating this condition leads to the equilibrium shifting to a high-bridge equilibrium (section 3.4.3). We also require $n(0) < N$, or $g_3 < g_e$. See table 3.3 for the values of g_d and g_e.

Though it may initially seem counterintuitive, the requirement that $g_d < g_3 < g_e$ can only be satisfied for small patch-lengths L. For larger L, $g_e < g_d$, and guaranteeing that the population is above $2N/3$ everywhere also corresponds to the population being larger than the domain of population size N. Adjusting N does not affect this issue, as N is involved in both g_d and g_e. This suggests that for larger patch-lengths, populations with large maximum densities are more likely to vary in density over the patch so that the equilibrium distributions have more than one growth-level inside the patch.

Two-level equilibria: low-bridge and high-bridge equilibria

In the next two cases, the population satisfies $(i-1)N/3 < n_t(L/2) < iN/3$ and $iN/3 < n_t(0) < (i+1)N/3$ for $i = 1,2$. The population will see the two growth-levels g_i and g_{i+1} inside the patch. Using the general expression from eq. (3.10), our population

Table 3.3 Critical values of the growth levels g_i for the three-step block-pulse IDE where equilibria meet or equilibrium behavior changes.

$g_a = \frac{N/3}{F(L/2)-F(-L/2)}$	$g_{s_1} = \frac{\frac{2N}{3}k(L)}{[F(L)-F(0)][k(L)+k(0)]}$
$g_b = \frac{N/3}{F(L)-F(0)}$	$g_{s_2} = \frac{\frac{4N}{3}k(L)}{[F(L)-F(0)][k(L)+k(0)]}$
$g_c = \frac{2N/3}{F(L/2)-F(-L/2)}$	
$g_d = \frac{2N/3}{F(L)-F(0)}$	
$g_e = \frac{N}{F(L/2)-F(-L/2)}$	

distributions in these scenarios will be

$$\begin{aligned} n_{t+1}(x) =& g_i\left[F\left(x+L/2\right)-F\left(x-L/2\right)\right] \\ &+\left(g_{i+1}-g_i\right)\left[F\left(x+r_{i,t}\right)-F\left(x-r_{i,t}\right)\right]. \end{aligned} \tag{3.39}$$

As with the bridge map in section 3.4.2, we can define an implicit map to find the next spatial threshold $r_{i,t+1}$, and use this map to find the spatial-threshold fixed-points $r_{i,t+1} = r_{i,t} = r_i$. With the fixed points r_i, we may then use eq. (3.39) to find the equilibrium distribution where $n_{t+1}(x) = n_t(x) = n(x)$. The two-level equilibrium that results is given by

$$n(x) = g_i\left[F\left(x+L/2\right)-F\left(x-L/2\right)\right]+\left(g_{i+1}-g_i\right)\left[F\left(x+r_i\right)-F\left(x-r_i\right)\right]. \tag{3.40}$$

We call this the low-bridge equilibrium for $i = 1$, and the high-bridge equilibrium for $i = 2$.

For both the low-bridge and high-bridge equilibria, we seek to characterize the equilibria through the behavior of g_2. For the low-bridge equilibrium, utilizing eq. (3.40) with $i = 1$, fixing g_1 and using $n(r_1) = N/3$, we obtain an expression for g_2,

$$g_2 = \frac{N/3 - g_1\left[F\left(r_1+L/2\right)-F\left(r_1-L/2\right)-F\left(2r_1\right)+F\left(0\right)\right]}{F\left(2r_1\right)-F\left(0\right)}, \tag{3.41}$$

in terms of r_1.

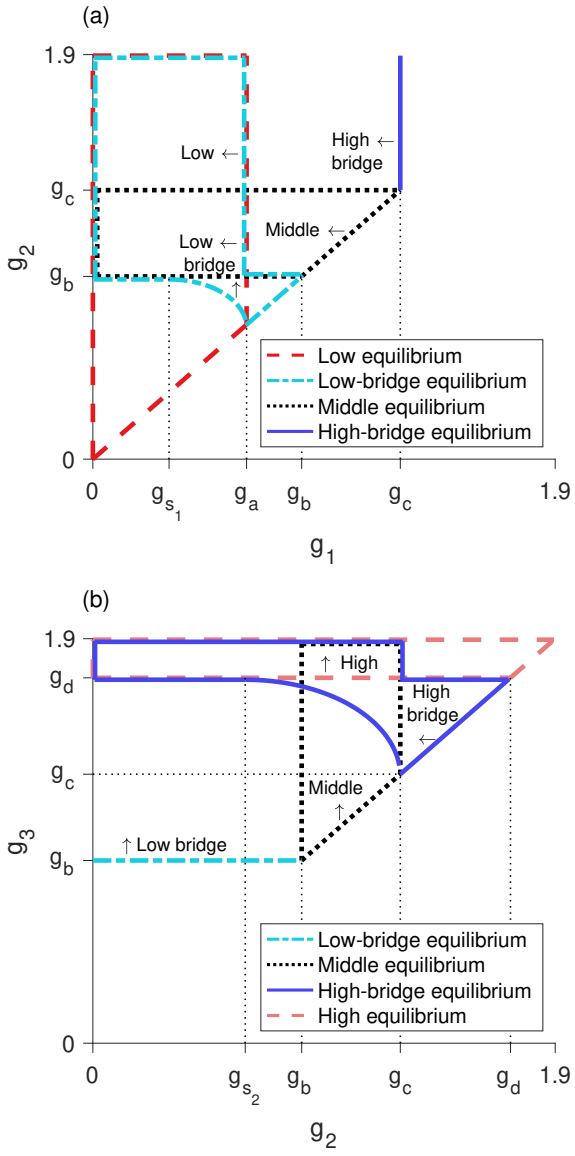

Fig. 3.7 Regions of validity in **a** $g_1 - g_2$ space and **b** $g_2 - g_3$ space for five of the six equilibrium types of the three-step model. All equilibria are invalid for $g_1 \geq g_2$ and $g_2 \geq g_3$. **a**, region of validity is inside: the dashed region for the low equilibrium, the dotted region for the middle equilibrium, and the dashed-dotted region for the low-bridge equilibrium. The high-bridge equilibrium is valid to the left of the vertical solid line. For $g_{s_1} < g_1 < g_a$, as g_2 increases through the lower border of the region for the low-bridge equilibrium, a fold bifurcation occurs leading to two new low-bridge equilibria. **b**, region of validity is inside: the dotted region for the middle equilibrium, the dashed region for the high equilibrium, and the solid region for the high-bridge equilibrium. The low-bridge equilibrium is valid above the horizontal dashed-dotted line. For $g_c < g_3 < g_d$, as g_2 increases through the left boundary of the region for the high-bridge equilibrium, a fold bifurcation occurs leading to two new high-bridge equilibria. Parameter values are $L = 0.3$, $N = 1$, $\alpha = 5$, $g_{s_1} \approx 0.3$, $g_{s_2} \approx 0.6$, $g_a \approx 0.6$, $g_b \approx 0.9$, $g_c \approx 1.3$, $g_d \approx 1.7$, $g_e \approx 1.9$.

The behavior of this function for g_2 is nearly identical to the equivalent eq. (3.33) for the bridge equilibrium in the two-step model. There are again three different parameter regimes leading to different behaviors of eq. (3.41), and therefore different behaviors of the low-bridge equilibria. These parameter regimes for the low-bridge equilibria are summarized in table 3.4 and displayed in parameter space in fig. 3.7. Figures 3.8 to 3.11 show bifurcation diagrams of the maximum and minimum population-densities as g_2 varies, demonstrating the different behaviors of the low-bridge equilibria for different parameter sets. See section C.3.1 for details of the behavior of eq. (3.41) in the different parameter regimes.

The parameter limits in table 3.4 encompass the restrictions $n(L/2) < N/3 < n(0)$. At the point where the first inequality is violated, the low-bridge equilibrium meets the middle equilibrium. When the second inequality is violated, the low-bridge equilibrium meets the low equilibrium. There is a third restriction, $n(0) < 2N/3$, to guarantee we have a low-bridge equilibrium. Violating this condition would result in the low-bridge equilibrium becoming a full-bridge equilibrium (section 3.4.3). Given the other parameter restrictions for the low-bridge equilibrium to exist, this condition is always satisfied so that the low-bridge and full-bridge equilibria never meet.

Table 3.4 Number of low-bridge equilibria in different parameter regions. If there is no entry in a particular row or column, there is no valid solution to eq. (3.41) and therefore no low-bridge equilibrium in that region.

	$g_1 < g_2 < g_b$	$g_b < g_2$
$0 < g_1 < g_{s_1}$ [1]		One low-bridge equilibrium
$g_{s_1} < g_1 < g_a$	Two low-bridge equilibria for some $g_2 < g_b$ [2]	One low-bridge equilibrium
$g_a < g_1 < g_b$	One low-bridge equilibrium	

[1] See table 3.3 for the value of g_{s_1}.

[2] There is a numerically calculable lower bound in g_2 for this region, shown in fig. 3.7a, but no analytical expression for this lower bound.

We now shift to examine what values of g_2 yield a valid high-bridge equilibrium, and the

number of high-bridge equilibria. Utilizing eq. (3.40) with $i = 2$, fixing g_3 and using $n(r_2) = 2N/3$, we express g_2 as

$$g_2 = \frac{2N/3 - g_3 [F(2r_2) - F(0)]}{F(r_2 + L/2) - F(r_2 - L/2) - F(2r_2) + F(0)} \tag{3.42}$$

in terms of r_2.

This function behaves similarly to the function for g_2 in the low-bridge equilibrium, though there are only two parameter regions that yield a valid high-bridge equilibrium. A summary of these parameter regimes is given in table 3.5 and the regions are illustrated in fig. 3.7. The bifurcation diagrams in figs. 3.8 to 3.11 illustrate the behavior of the high-bridge equilibrium in these different parameter regions. The limits in table 3.5 encompass the restrictions that $n(L/2) < 2N/3 < n(0) < N$. As in the other bridge equilibria, when the function for g_2 is multivalued, increasing g_2 through the lower boundary of validity for the high-bridge equilibrium corresponds to a fold bifurcation. See section C.3.2 for a more detailed description of the behavior of eq. (3.42) in each parameter region.

Table 3.5 High-bridge equilibria in different parameter regions. If there is no entry in a particular row or column, there is no valid solution to eq. (3.42) and therefore no high-bridge equilibrium in that region.

	$g_c < g_3 < g_d$	$g_d < g_3$
$0 < g_2 < g_{s_2}$ [1]		One high-bridge equilibrium
$g_{s_2} < g_2 < g_c$	Two high-bridge equilibria for some g_2 [2]	One high-bridge equilibrium
$g_c < g_2 < g_d$	One high-bridge equilibrium	

[1] See table 3.3 for the value of g_{s_2}.

[2] A numerically calculable lower bound in g_2 exists for this region, shown in fig. 3.7b, but there is no analytical expression for this lower bound.

In addition to meeting the middle and high equilibria, the high-bridge equilibrium may also meet the full-bridge equilibrium if $N/3 < n(L/2)$ is violated. Earlier, we noted that the low-bridge

and full-bridge equilibria do not meet. This is not true for the high-bridge equilibrium, and it is possible that $n(L/2) = N/3$ for $r_1 = L/2$ and some r_2 value.

There are two main ways in which the high-bridge and full-bridge equilibria may interact, depending on whether there are one or two high-bridge equilibria. In both cases, it is possible that the full-bridge equilibrium is not valid so that the high-bridge and full-bridge equilibria do not meet. If the full-bridge equilibrium does exist, when there are two high-bridge equilibria there will be two r_2 values where $n(L/2) = N/3$ and the full-bridge equilibrium is spliced into the high-bridge equilibrium (figs. 3.9 and 3.10). When there is a single high-bridge equilibrium, there may either be one (fig. 3.11) or two r_2 values where $n(L/2) = N/3$. We will return to these interactions in the next part of section 3.4.3.

To complete analysis of the low-bridge and high-bridge equilibria, we take the same approach to analyzing the stability of the equilibria as in section 3.4.2, by considering the stability of the spatial-threshold fixed-points r_i, $i = 1,2$. The derivative of the spatial-threshold map, evaluated at r_i, is

$$r_i' = \frac{(g_i - g_{i+1})\left[k(2r_i) + k(0)\right]}{g_i\left[k(r_i + L/2) - k(r_i - L/2)\right] + (g_{i+1} - g_i)\left[k(2r_i) - k(0)\right]}, \tag{3.43}$$

where $r_i' = dr_{i,t+1}/dr_{i,t}$. The equilibrium will be stable if $|r_i'| < 1$. Note this is the same general form of the derivative in eq. (3.35) from section 3.4.2.

When $g_1 < g_{s_1}$, the low-bridge equilibrium is unstable (fig. 3.11). When $g_1 > g_a$, this equilibrium is stable (fig. 3.10). For $g_{s_1} < g_1 < g_a$, there is a fold bifurcation for some g_2 value, corresponding to a critical r_1 value for which $r_1' = 1$. This bifurcation point in g_2 corresponds to the lower boundary for the low-bridge equilibrium in fig. 3.7a when g_1 is within the given limits. As g_2 increases through this boundary, two low-bridge equilibria appear. The low-bridge equilibrium with the larger r_1 fixed point is stable, while the low-bridge equilibrium with the smaller r_1 fixed point is unstable. These correspond to the upper and lower branches of the low-bridge equilibria, as shown in figs. 3.8 and 3.9.

For the high-bridge equilibrium, when $g_c < g_3 < g_d$, there is a fold bifurcation when $r_2' = 1$

(figs. 3.8 and 3.9). This bifurcation point in g_2 corresponds to the left high-bridge boundary in fig. 3.7b when g_3 is within the stated limits. As g_2 increases through the boundary, the fold bifurcation results in the appearance of two high-bridge equilibria. We note that for larger L, the fold bifurcation may occur in the full-bridge equilibrium instead, which also leads to two high-bridge equilibria (fig. 3.10).

The high-bridge equilibrium with the larger r_2 fixed point, corresponding to the upper branch of the high-bridge equilibrium shown in figs. 3.8 to 3.10, is stable. The high-bridge equilibrium with the smaller r_2 fixed point, or the lower branch of the high-bridge equilibrium in figs. 3.8 to 3.10, is unstable. This lower branch terminates at $g_2 = g_c$ where it collides with the middle equilibrium.

For $g_3 > g_d$, the high-bridge equilibrium is unstable (fig. 3.11). For details of the stability analysis for both two-level equilibria, see appendix A.3.

Full-bridge equilibrium

In the sixth and final case, the population is below $N/3$ at the edges of the patch, above $2N/3$ at the center of the patch, and between $N/3$ and $2N/3$ in some interval between the edges and middle of the patch. The population sees all three growth-levels g_1, g_2, and g_3. The population distribution is

$$\begin{aligned} n_{t+1}(x) =& g_1 \left[F(x+L/2) - F(x-L/2)\right] \\ &+ (g_2 - g_1)\left[F(x+r_{1,t}) - F(x-r_{1,t})\right] \\ &+ (g_3 - g_2)\left[F(x+r_{2,t}) - F(x-r_{2,t})\right]. \end{aligned} \tag{3.44}$$

We may use eq. (3.44) to construct a two-dimensional map for the spatial thresholds $r_{1,t}$ and $r_{2,t}$. We can use the map to find the spatial-threshold fixed-points where both $r_{1,t+1} = r_{1,t} = r_1$ and $r_{2,t+1} = r_{2,t} = r_2$ are satisfied, and then use these fixed points to find the full equilibrium-

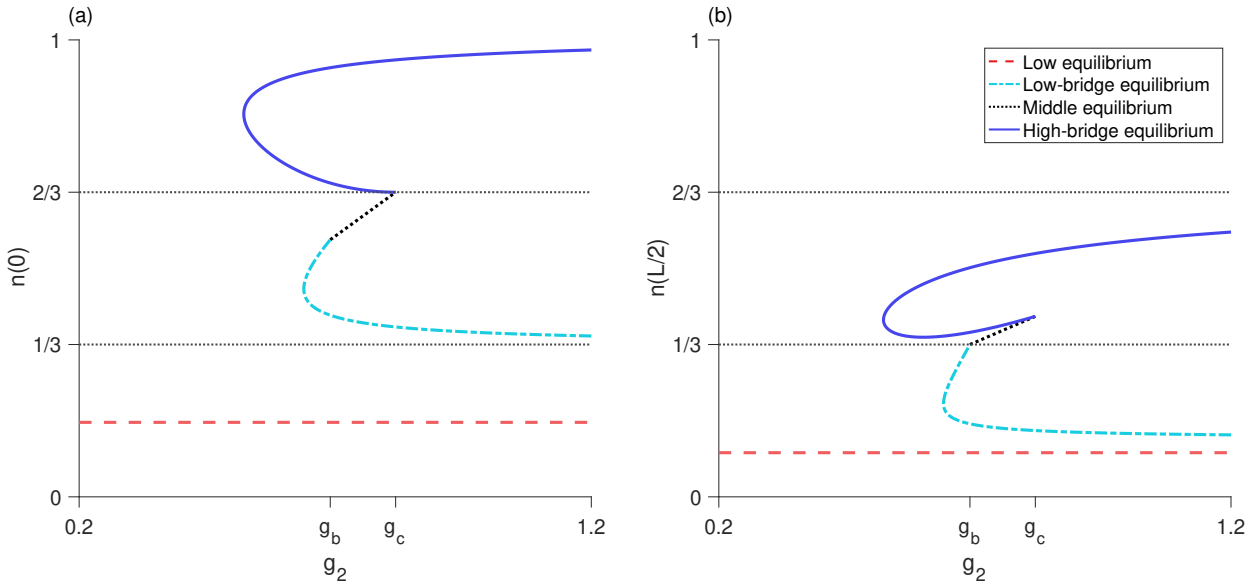

Fig. 3.8 Bifurcation diagram as g_2 varies for the three-step model. **a**, the maximum amplitude $n(0)$ of the equilibrium distributions. **b**, the minimum amplitude $n(L/2)$ of the equilibria. Neither the full-bridge nor high equilibria exist for this parameter set, while both the low-bridge and high-bridge equilibria have a fold bifurcation leading to two branches of equilibria. The low and middle equilibria, as well as the upper branches of both low-bridge and high-bridge equilibria, are stable. The lower branches of the low-bridge and high-bridge equilibria are unstable. Parameter values are $L = 0.675$, $N = 1$, $\alpha = 5$, $g_1 = 0.2$, $g_3 = 1.2$, $g_{s_1} \approx 0.046$, $g_a \approx 0.41$, $g_b \approx 0.69$, $g_c \approx 0.82$, $g_d \approx 1.38$.

distribution. This is the full-bridge equilibrium, given by

$$\begin{aligned} n(x) =& g_1 \left[F(x+L/2) - F(x-L/2)\right] \\ &+ (g_2 - g_1)\left[F(x+r_1) - F(x-r_1)\right] \\ &+ (g_3 - g_2)\left[F(x+r_2) - F(x-r_2)\right], \end{aligned} \tag{3.45}$$

which is valid for $n(L/2) < N/3 < 2N/3 < n(0)$.

As the full-bridge equilibrium depends on three growth-levels and two spatial thresholds, analysis becomes more challenging. It is more intuitive to understand the full-bridge equilibrium based on how it interacts with the high-bridge equilibrium. The full-bridge and high-bridge equilibria

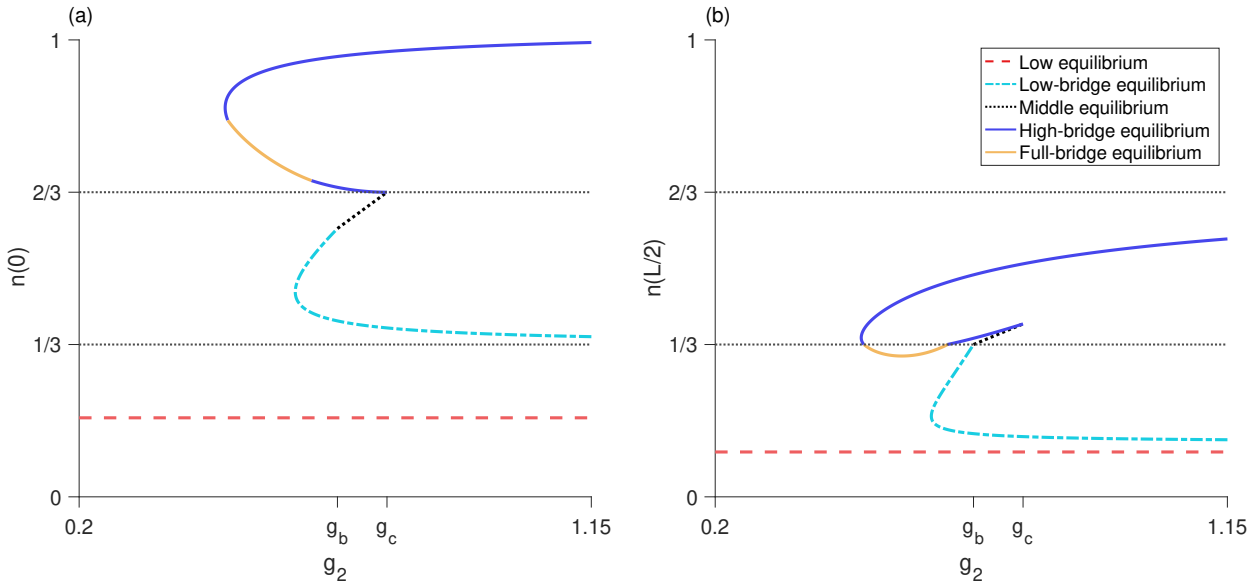

Fig. 3.9 Bifurcation diagram as g_2 varies for the three-step model. **a**, the maximum amplitude $n(0)$ of the equilibrium distributions. **b**, the minimum amplitude $n(L/2)$ of the equilibria. The high equilibrium does not exist for this parameter set, while both the low-bridge and high-bridge equilibria have a fold bifurcation leading to two branches of equilibria. Now, the full-bridge equilibrium is also valid. It exists as a single piece between two segments of the lower branch of the high-bridge equilibrium, where $n(L/2) < N/3$. The low and middle equilibria, as well as the upper branches of both low-bridge and high-bridge equilibria, are stable. The full-bridge equilibrium and lower branches of the low-bridge and high-bridge equilibria are unstable. Parameters are $L = 0.8$, $N = 1$, $\alpha = 5$, $g_1 = 0.2$, $g_3 = 1.15$, $g_{s_1} \approx 0.024$, $g_a \approx 0.39$, $g_b \approx 0.68$, $g_c \approx 0.77$, $g_d \approx 1.36$.

meet when $n(r_1 = L/2) = N/3$, so that the high-bridge equilibrium transitions to the full-bridge equilibrium when

$$g_2 [F(L) - F(0)] + (g_3 - g_2) [F(L/2 + r_2) - F(L/2 - r_2)] = N/3, \tag{3.46}$$

or, equivalently, when

$$g_2 = \frac{N/3 - g_3 [F(L/2 + r_2) - F(L/2 - r_2)]}{F(L) - F(0) - F(L/2 + r_2) + F(L/2 - r_2)}. \tag{3.47}$$

Equation (3.47), which only depends on one spatial threshold r_2, allows us to determine general patterns of the full-bridge equilibrium by observing the possible g_2 values where the high-bridge

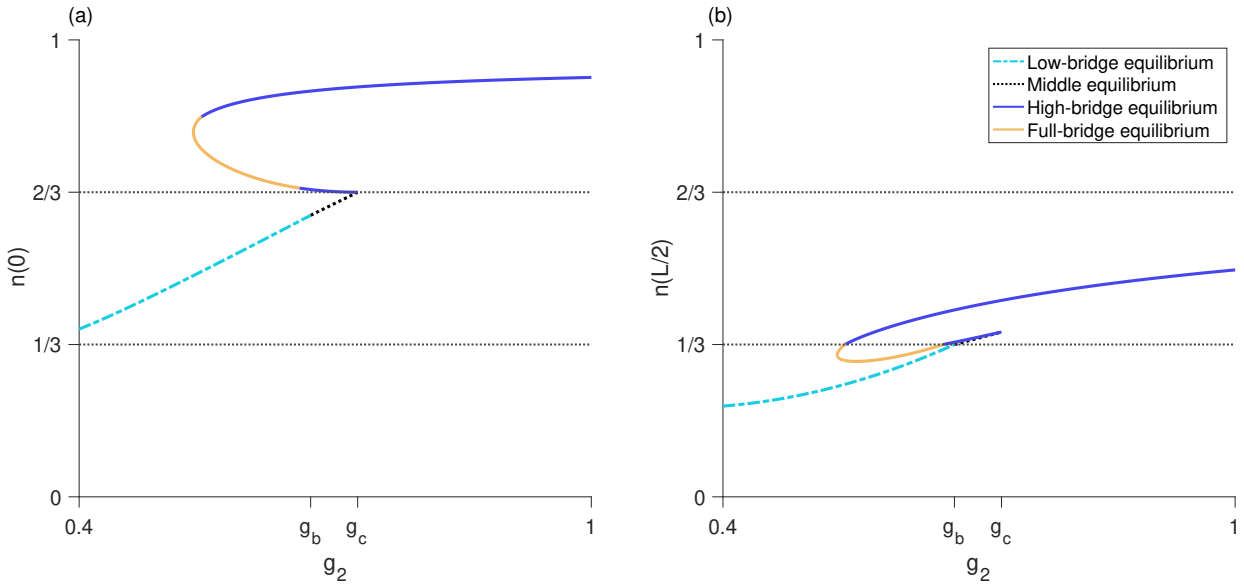

Fig. 3.10 Bifurcation diagram as g_2 varies for the three-step model. **a**, the maximum amplitude $n(0)$ of the equilibrium distributions. **b**, the minimum amplitude $n(L/2)$ of the equilibria. Neither the low or high equilibria exist for this parameter set. There is now only one low-bridge equilibrium. A fold bifurcation occurs in the full-bridge equilibrium, and there are two branches of high-bridge equilibria. The middle equilibrium and low-bridge equilibrium, as well as the upper branches of both high-bridge and full-bridge equilibria, are stable. The lower branches of the high-bridge and full-bridge equilibria are unstable. Parameters are $L = 1$, $N = 1$, $\alpha = 5$, $g_1 = 0.4$, $g_3 = 1$, $g_a \approx 0.36$, $g_b \approx 0.67$, $g_c \approx 0.73$, $g_d \approx 1.34$.

and full-bridge equilibria meet. As $r_2 \to L/2$, $g_2 \to -\infty$. As $r_2 \to 0$, $g_2 \to g_b$. Thus, we may infer that the full-bridge equilibrium is valid for at least some values $g_2 < g_b$.

If there are two branches of high-bridge equilibria, the full-bridge equilibrium will meet a high-bridge equilibrium twice at two different r_2 values or not at all. These options are illustrated in fig. 3.12b, when $g_3 < g_d$. In the latter case for smaller g_3 values, the full-bridge equilibrium is never valid (fig. 3.8). In the former case for slightly larger g_3, the full-bridge equilibrium will exist in between two segments of the high-bridge equilibria. Figures 3.9 and 3.10 show two different ways in which this may occur. In fig. 3.9, a fold bifurcation occurs in the high-bridge equilibrium, and the full-bridge equilibrium is spliced into the lower branch of the high-bridge equilibrium. In

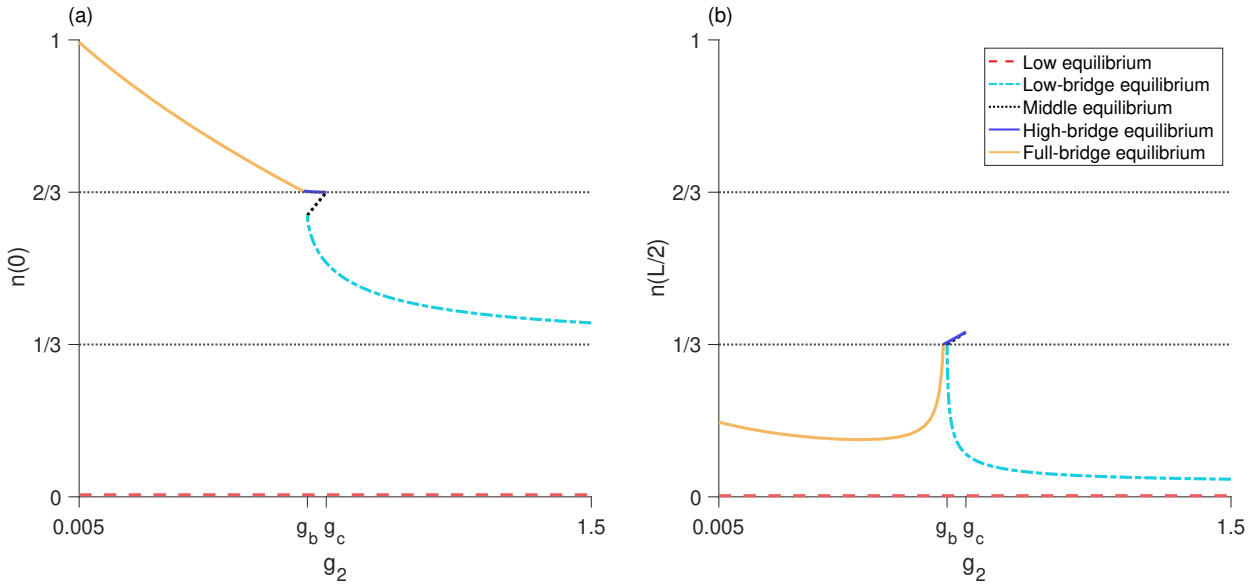

Fig. 3.11 Bifurcation diagram as g_2 varies for the three-step model. **a**, the maximum amplitude $n(0)$ of the equilibrium distributions. **b**, the minimum amplitude $n(L/2)$ of the equilibria. The high equilibrium does not exist for this parameter set. There is only one each of the low-bridge, high-bridge, and full-bridge equilibria. The low and middle equilibria are stable. The low-bridge, high-bridge, and full-bridge equilibria are unstable. Parameter values are $L = 1$, $N = 1$, $\alpha = 5$, $g_1 = 0.005$, $g_3 = 1.5$, $g_{s_1} \approx 0.009$, $g_a \approx 0.36$, $g_b \approx 0.67$, $g_c \approx 0.73$, $g_d \approx 1.34$.

fig. 3.10, there is a fold bifurcation in the full-bridge equilibrium instead, so that the upper full-bridge equilibrium meets the upper high-bridge equilibrium, and the lower full-bridge equilibrium meets the lower high-bridge equilibrium.

If there is a single high-bridge equilibrium for $g_1 < g_2 < g_c$, the full-bridge equilibrium may meet the high-bridge equilibrium either twice or once for some $g_2 < g_b$. These possibilities are illustrated in fig. 3.12b. That is, for $g_3 > g_d$, there are two options for crossing the inner solid boundary marking where the high-bridge and full-bridge equilibria meet (shown in fig. 3.12b). For g_3 just larger than g_d, there is a high-bridge equilibrium that transitions into a full-bridge and then back again as g_2 increases. Thus, the full-bridge equilibrium exists between two segments of the high-bridge equilibrium. For relatively larger g_3, the equilibrium starts as a full-bridge equilibrium

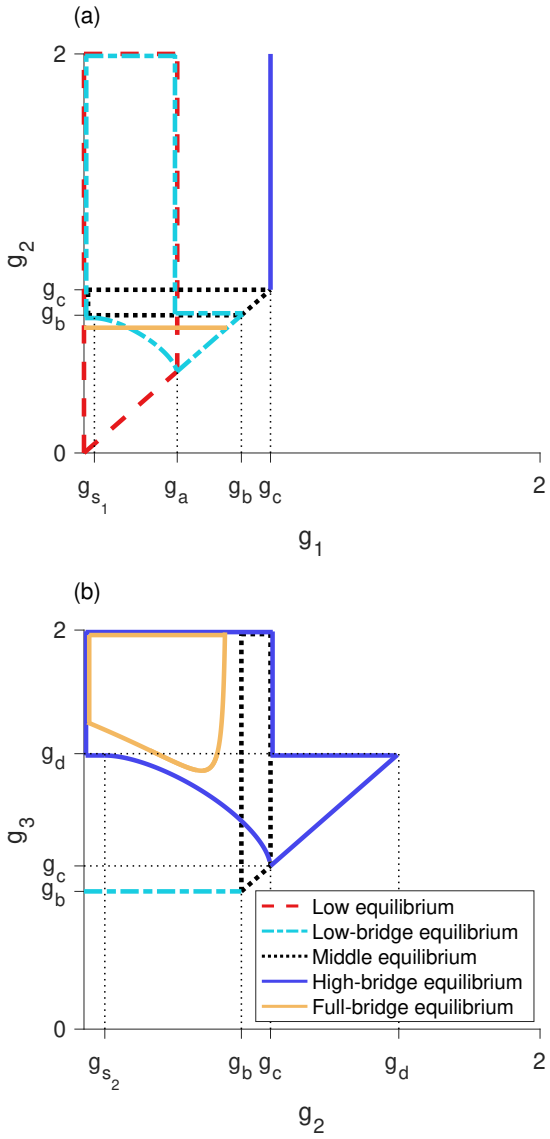

Fig. 3.12 Regions of validity in **a** $g_1 - g_2$ space and **b** $g_2 - g_3$ space for the three-step model, with the region where the high-bridge and full-bridge equilibria meet. All equilibria are invalid for $g_1 \geq g_2$ and $g_2 \geq g_3$. A fold bifurcation occurs in the high-bridge equilibrium; for larger L the fold bifurcation may occur in the full-bridge equilibrium. **a**, the full-bridge equilibrium may be valid for g_2 below the nearly horizontal solid line. **b**, the high-bridge equilibrium is valid inside the outer solid region. The inner solid curve marks the boundary where the full-bridge equilibrium meets the high-bridge equilibrium. The full-bridge equilibrium exists inside the inner solid region. For fixed g_3, increasing g_2 through the left boundary of the region for the full-bridge equilibrium corresponds to the high-bridge transitioning to a full-bridge equilibrium. As g_2 increases through the right boundary of the region for the full-bridge equilibrium, there is a transition back into a high-bridge equilibrium. For this domain length, the high equilibrium is not valid. Parameter values are $L = 0.675$, $N = 1$, $\alpha = 5$, $g_{s_1} \approx 0.05$, $g_{s_2} \approx 0.09$, $g_a \approx 0.4$, $g_b \approx 0.7$, $g_c \approx 0.8$, $g_d \approx 1.4$.

and turns into a high-bridge equilibrium (see fig. 3.11). It may also be the case that eq. (3.47) is never satisfied, so that the full-bridge equilibrium does not exist. This possibility exists for smaller L.

In general, we observe that if the full-bridge equilibrium exists and there are two branches of high-bridge equilibria, there may be one full-bridge equilibrium (fig. 3.9) or two (fig. 3.10). If there is only one high-bridge equilibrium, there will also only be one full-bridge equilibrium if it exists (fig. 3.11).

We also use a stability analysis to cast light on the full-bridge equilibrium. With a two-dimensional mapping of the spatial thresholds, we employ the Jury conditions [59], applied to the Jacobian of the map evaluated at the fixed point (r_1, r_2). Three Jury conditions are needed for stability of a fixed point of this system, given by

$$1 - \tau + \Delta > 0, \tag{3.48}$$

$$1 + \tau + \Delta > 0, \tag{3.49}$$

$$\Delta < 1, \tag{3.50}$$

where τ and Δ are the trace and determinant of the Jacobian. The first condition ensures there are no eigenvalues greater than $+1$, the second that there are no eigenvalues less than -1, and the third that no complex eigenvalues are outside the unit circle. Violating any Jury condition leads to a local bifurcation and loss of stability.

Differentiating the two-dimensional spatial-threshold mapping with respect to $r_{1,t}$ and $r_{2,t}$ gives the Jacobian, from which we check the Jury conditions eq. (3.48)–eq. (3.50). The map, Jacobian, and stability analysis may be found in appendix B.3. We find that the eigenvalues of the Jacobian are always real. Thus, we do not need to consider the third Jury condition in eq. (3.50), as this condition deals with complex eigenvalues. We also find that the second Jury condition in eq. (3.49)

is always satisfied. The only Jury condition that may be violated is the first. In particular, violation of this Jury condition leads to the fold bifurcation that we have already mentioned, where two distinct full-bridge equilibria emerge as g_2 increases (see fig. 3.10).

In the case when $g_3 > g_d$, the full-bridge equilibrium is unstable. The only stable full-bridge equilibrium occurs if there is a fold bifurcation. In this case, the upper branch is stable and the lower branch is unstable. If a fold bifurcation occurs in the high-bridge equilibria and the full-bridge equilibrium exists between two segments of the lower high-bridge equilibrium, it is also unstable. These are largely heuristic results, and based primarily on continuity of stability for the high-bridge equilibria along with numerical experiments testing the first Jury condition for a wide range of parameter sets.

Three-step block-pulse IDE: conclusions

The three-step block-pulse IDE yields a remarkable complexity of behaviors. With six different types of equilibria and a variety of possible transitions between those equilibria, the dynamics of the system may be extremely varied, as seen in figs. 3.8 to 3.11. There are potential fold bifurcations for three of the equilibria. That is, as g_2 (or any growth level) increases, there may be a fold bifurcation resulting in the sudden appearance of two new equilibria, one stable and one unstable. As the parameter increases further, there may also be another fold bifurcation in which an unstable equilibrium and a stable equilibrium collide in a sharp point and annihilate one another.

Stability of the equilibria again seems to follow a general trend. The one-level equilibria are always stable, and stability always alternates so that there are never two neighboring stable or unstable equilibria. In the case of a fold bifurcation, the upper equilibrium that emerges is stable, while the lower equilibrium is unstable. These patterns directly mirror the behavior of the two-step model.

Based on the trends observed in the one-, two-, and three-step block-pulse IDEs, we hypothesize that for an m-step block-pulse IDE the same stability patterns will continue. It is evident that

the one-level equilibria, which have one growth-level g_i inside the patch, are always stable. Stability of equilibria should also alternate between stable and unstable, and if a fold bifurcation occurs, the resulting upper branch of equilibria will be stable and the lower branch unstable. Based on the process outlined in previous sections for using the spatial-threshold fixed-points to find the full spatial equilibrium-distribution, we also construct a general expression for a p-level equilibrium,

$$\begin{aligned} n(x) = {} & g_q \left[F(x+L/2) - F(x-L/2) \right] \\ & + \sum_{i=q}^{q+p-1} (g_{i+1} - g_i) \left[F(x+r_i) - F(x-r_i) \right], \end{aligned} \tag{3.51}$$

for $1 \leq p \leq m$, where q is the index of the smallest growth-level, g_q, that the p-level equilibrium sees inside the patch.

3.5 Applications

To illustrate the effectiveness of the block-pulse IDE, we applied three-, five-, and ten-step block-pulse models to an IDE with Beverton-Holt growth and an IDE with an Allee effect. For the original models, we calculated the maximum amplitudes of both stable and unstable equilibria for varying growth-parameters using a phase-plane method, applicable for IDEs with the Laplace kernel (see, e.g., Kot and Schaffer [64], Lutscher [84]). This method cannot, in general, be used for other kernels, which is why we chose the Laplace kernel for our examples.

For the block-pulse models, we calculated the maximum amplitudes of both stable and unstable equilibria using analytic expressions for the equilibria derived from eq. (3.51). For each m-step block-pulse model, there are m one-level equilibria, $m-1$ two-level equilibria, and so on, for a total of $m(m+1)/2$ different equilibria. In general, there are $m-p+1$ different p-level equilibria for every $1 \leq p \leq m$.

For the m one-level equilibria, the population distributions are trivial to calculate using eq. (3.51). For each of the $m(m-1)/2$ remaining p-level equilibria, $2 \leq p \leq m$, we first employed a multivariate root-finder to solve for the set of $p-1$ spatial-threshold fixed-points. Then, we substituted

the fixed points into the relevant equilibrium distribution from eq. (3.51), evaluated at $x = 0$. In particular, to find the spatial-threshold fixed-points, we used `MATLAB` 2019a [90] and the built-in function '`fsolve`,' a function for solving a system of nonlinear equations by minimizing the sum of squares. (The open-source softwares `Octave` [32] and `R` [106] both have the same command.) We used this function with the trust-region dogleg algorithm, a robust and efficient iterative optimization-method for solving nonlinear systems of equations.

As there may be two branches of any given p-level equilibrium for $p \geq 2$, careful choice of initial guesses for the spatial thresholds is required to ensure that both solutions to the nonlinear system are reliably found. Choosing one initial guess to have the spatial thresholds close to $L/2$ and a second initial guess to have the spatial thresholds close to 0 is a good rule of thumb to ensure both branches, if they exist, of a p-level equilibrium are picked up. For example, in a three-level equilibrium, we might choose the first initial guess for the spatial thresholds to be $(r_1, r_2) = (L/2 - \varepsilon, L/2 - \varepsilon)$ and the second initial guess to be $(r_1, r_2) = (\varepsilon, \varepsilon)$ where ε is some small positive value.

Bifurcation diagrams comparing the original models to block-pulse models as the growth parameter varies are shown for the Beverton-Holt model in fig. 3.13 and for the Allee model in fig. 3.14. Van Kirk and Lewis [139] compute similar bifurcation diagrams using the average dispersal-success approximation. We therefore note that block-pulse IDEs are a complementary approach to methods like average dispersal-success or geometric symmetrization, and these methods may be used to answer similar ecological questions.

3.5.1 Block-pulse IDE with Beverton-Holt growth

The Beverton-Holt model is a classical model of compensatory population growth given by

$$g(n_t) = \frac{R_0 n_t}{1 + [(R_0 - 1)/K] n_t}, \tag{3.52}$$

where K is the carrying capacity and R_0 is the net reproductive rate of the population. For the IDE with Beverton-Holt growth, there is a transcritical bifurcation in which a branch of nontrivial

equilibria becomes positive, exchanging stability with the branch of trivial equilibria. A comparison of the maximum amplitudes of the equilibria for the full growth-model and three-, five-, and ten-step block-pulse IDEs are shown in fig. 3.13, where we distinguish between the different p-level equilibria of the block-pulse IDEs to illustrate where the types of equilibria occur and how they merge. For all three block-pulse models, a single fold bifurcation occurs between each set of density thresholds iN/m and $(i+1)N/m$, $i = 1,2,...,m-1$.

As the number of steps in the block-pulse model increases, we see increasing agreement between the equilibria for the two models. Numerically we observe that for each fold bifurcation in the block-pulse model, the upper branch of equilibria is stable and the lower branch is unstable. This is in agreement with our earlier conclusions regarding stability from section 3.4. With an increasing number of steps, the block-pulse equilibria that trace the stable nontrivial equilibrium branch have longer and longer stable upper branches while the unstable portions get rapidly smaller. The lowest branch of equilibria also gets closer to zero, while the lowest fold bifurcation (where two equilibria collide and destroy each other) gets slowly closer to the point of bifurcation for the full Beverton-Holt model. For ten steps, the block-pulse model offers a decent approximation of the true equilibrium solutions, though it is not as accurate closer to the transcritical bifurcation in the full Beverton-Holt model.

In all three block-pulse models, there is typically only a small set of equilibria with large maximum amplitudes that have a larger number of growth levels. In the three-step model, this is the three-level equilibrium; in the five-step model it is the four-level equilibrium; and in the ten-step model it is the six-level equilibrium. Indeed, for the ten-step model, even though there could be equilibria that have up to ten growth-levels, we see that nearly all of the equilibria have five or fewer growth-levels, and no equilibria have more than six growth-levels.

To assess numerical efficiency of the models, we also implemented three methods of solving the piecewise-defined IDE in eq. (3.8) by iteration. We used a trapezoidal approximation to the integral, a convolution integral, and the CDF form of the model from eq. (3.10) to eliminate inte-

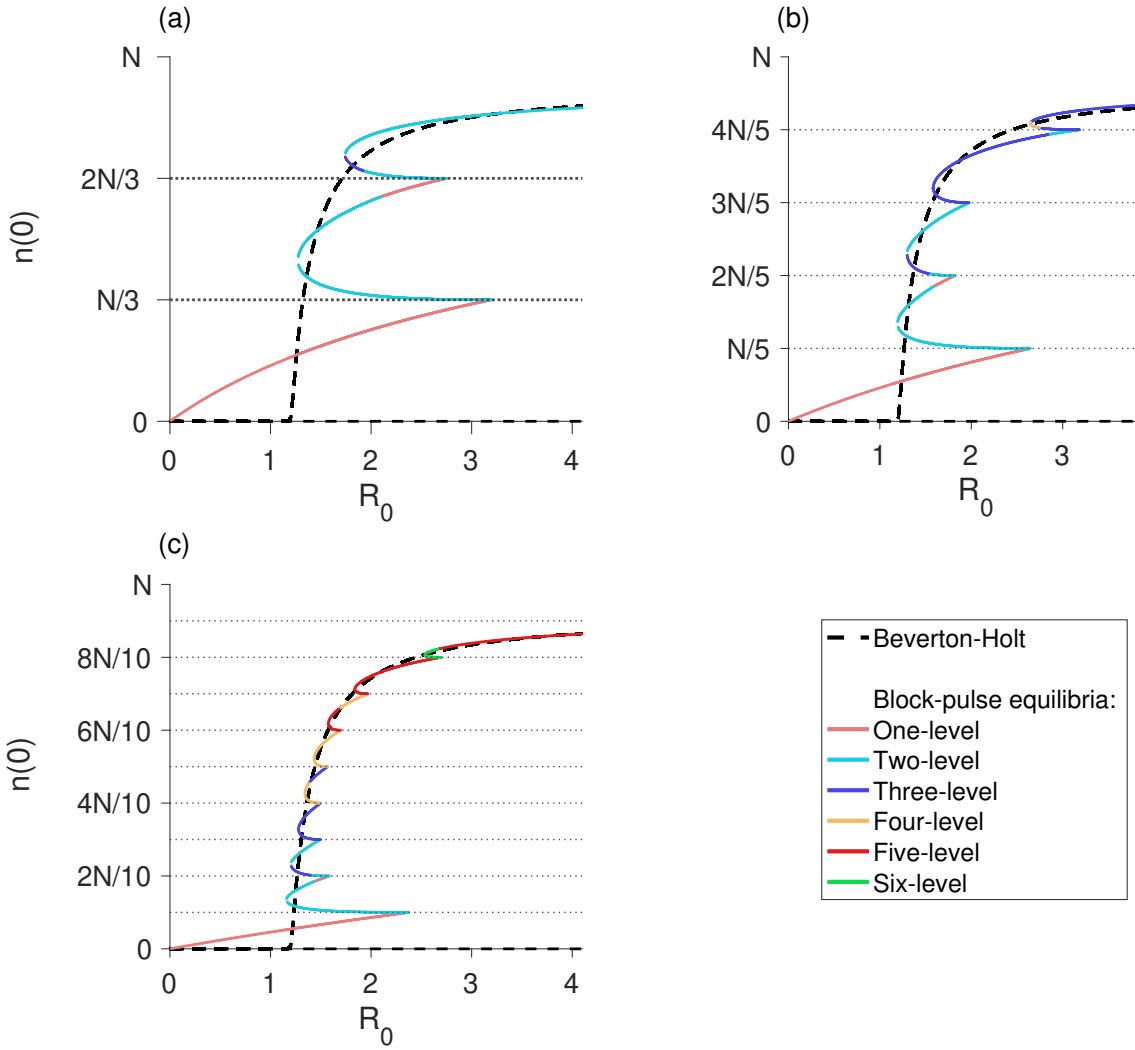

Fig. 3.13 The maximum population-density as R_0 varies for the Beverton-Holt model (dashed) compared to a **a** three-step block-pulse model, **b** five-step block-pulse model, and **c** ten-step block-pulse model. All block-pulse models are shown with solid lines; p-level equilibria are distinguished from each other for each $p = 1, 2, \ldots, m$. The Beverton-Holt model has a stable trivial equilibrium until just past $R_0 = 1$; a transcritical bifurcation occurs as a positive stable branch of nontrivial equilibria emerges and the trivial branch of equilibria becomes unstable. In the block-pulse models, the lower branch of each fold bifurcation is unstable while the upper branches are stable, so that stability alternates. Horizontal dotted lines indicate the density thresholds for each block-pulse model. Parameter values are $L = 1$, $N = 1$, $\alpha = 5$, $K = 1$.

gration entirely. For comparison between these methods, we used a domain length of $L = 1$ and spatial grid spacing of 2^{-10}. We simulated the model for 100 R_0 values with 100 different tent-map initial conditions each, running the three methods on a laptop with `MATLAB` 2019a [90].

For a ten-step Beverton-Holt block-pulse model, the trapezoidal approximation with the built-in function '`trapz`' took 5214 seconds to run. The convolution integral, using the built-in '`conv`' function ran in 26 seconds. (The '`trapz`' and '`conv`' commands exist under the same names for `Octave` and `R` as well.) Using cumulative distribution functions to iterate the block-pulse model ran in 16 seconds, a more than 300-fold increase in speed over the simple trapezoidal approximation.

The full Beverton-Holt model, meanwhile, ran in 57 seconds using the built-in convolution integral. Thus, to obtain the stable equilibria of the model, the fastest method of implementation for a ten-step block-pulse model ran about 3.5 times faster than an extremely efficient method for simulating the original model, while still offering a good approximation to the original model.

The ten-step block-pulse equilibria calculated with analytic expressions ran in 303 seconds. This method is not directly comparable to the others as it calculates both stable and unstable equilibria.

3.5.2 Block-pulse IDE with an Allee effect

We also applied three-, five-, and ten-step block-pulse models to an IDE with an Allee effect. The Allee growth-function was introduced in section 3.2, with

$$g(n_t) = \frac{\left[\left(1+\rho^2\right)/K\right] n_t^2}{1+\left(\rho/K\right)^2 n_t^2}, \tag{3.53}$$

where K is the carrying capacity and ρ is the growth parameter. For the IDE with Allee effect, a fold bifurcation leads to the emergence of two branches of nontrivial equilibria, with a stable upper branch and unstable lower branch. There is always a stable branch of trivial equilibria. Figure 3.14 shows the maximum amplitude of the equilibria as ρ varies for the Allee IDE compared to the block-pulse IDEs, again illustrating where the different p-level equilibria occur and how they

merge with one another. As in the Beverton-Holt model, a single fold bifurcation occurs between each set of density thresholds for each block-pulse model.

As the number of steps in the block-pulse model increases, we again see rapidly increasing agreement between the equilibria for the two different models. As in our analytics and the Beverton-Holt model, for each fold bifurcation that occurs in the block-pulse model as ρ increases, the upper branch is stable and the lower branch is unstable. Furthermore, as the number of steps in the block-pulse model increases, the block-pulse equilibria that trace the stable nontrivial equilibrium branch have increasingly longer stable branches while the unstable portions get rapidly smaller. Similarly, the block-pulse equilibria that trace along the unstable branch of Allee equilibria start to have longer unstable branches while the stable sections become very small. The lowest, stable line of equilibria in the block-pulse model also gets closer to zero as the number of steps increase. For only ten steps, we have reasonably good agreement between the block-pulse model and the Allee model on both location and stability of the equilibria.

As in section 3.5.1, for each block-pulse model the equilibria tend to correspond mostly to equilibria that have fewer growth-levels. Again, a six-level equilibrium is the equilibrium with the maximum number of growth levels in the ten-step model, and that equilibrium only occurs over a very small range of ρ values (fig. 3.14).

Using the same numerical methods as in the Beverton-Holt example, we also observed similar improvements in computational speeds for the Allee model. To obtain just the stable equilibria of the models, the CDF form of the 10-step block-pulse model ran a little over three times faster than the Allee model simulated with a convolution integral.

We also applied a ten-step block-pulse model to the IDE with Allee effect where we varied the patch length L for a fixed growth-parameter ρ. The resulting equilibrium behavior is shown in fig. 3.15 for three different dispersal kernels: the Gaussian (fig. 3.15a), the Laplace (fig. 3.15b), and the Cauchy (fig. 3.15c) distributions. We set the mean or median to zero and used the same median absolute deviation for all three kernels for consistency. As the unstable equilibria of the

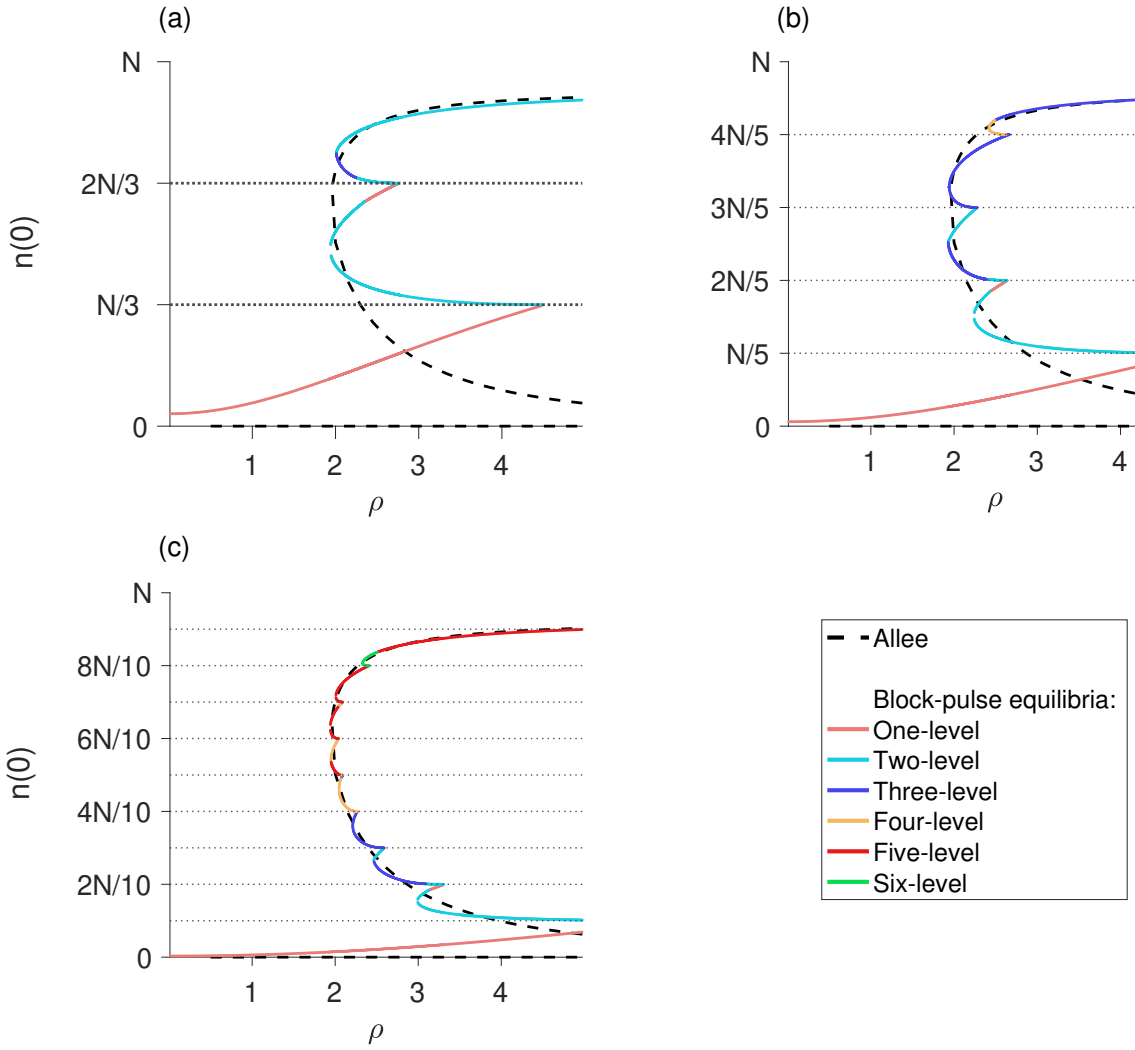

Fig. 3.14 The maximum population-density as ρ varies for an Allee-effect growth-model (dashed) compared to a **a** three-step block-pulse model, **b** five-step block-pulse model, and **c** ten-step block-pulse model. All block-pulse models are shown with solid lines; p-level equilibria are distinguished from each other for each $p = 1, 2, ..., m$. The lower branch of nontrivial Allee equilibria is unstable; the trivial and upper nontrivial branch of equilibria are stable. In the block-pulse models, for each fold bifurcation, the resulting lower branch is unstable and upper branch is stable, so that the lowest and highest branches of equilibria are stable, and stability alternates. Horizontal dotted lines indicate the density thresholds for each block-pulse model. Parameter values are $L = 1$, $N = 1$, $\alpha = 5$, $K = 1$.

original Allee model cannot be computed for the Gaussian and Cauchy kernels, we do not show the equilibria of the original model in these examples.

In general, we observe that larger patch-lengths L tend to correspond to equilibria that have a larger number of growth levels. This matches our intuition from section 3.4.3 that, for larger habitat-patches, population densities may be more likely to vary significantly over the patch.

While the bifurcation diagrams are reasonably similar for the Gaussian and Laplace kernels, the equilibrium behavior differs more significantly with the Cauchy kernel. In particular, the critical patch-length where a stable, nontrivial persistence-equilibrium emerges is larger for a model with a Cauchy dispersal kernel than the models with Gaussian or Laplace distributions. The maximum population-densities of the upper set of nontrivial equilibria are generally smaller, while the maximum population-densities of the lower set of nontrivial equilibria tend to be larger.

To compare the critical patch-size where a stable persistence-state first occurs more generally, we computed this critical patch-size for a variety of growth parameters ρ for the three kernels (fig. 3.15d). For the purposes of this problem, we defined the critical patch-length L_{crit} as the minimum L value where a nontrivial equilibrium occurred. As our smallest estimated equilibrium is not quite zero, but is clearly approximating a trivial equilibrium, we add that in this case, 'nontrivial' means an equilibrium whose maximum density $n(0) > \eta$, where η is some small positive number. For an alternative approach to calculating the critical patch-size for the Laplace kernel, see Li and Otto [77].

With this comparison, it appears that for a model with an Allee effect, the critical patch-length is somewhat sensitive to dispersal kernel for small growth-parameters ρ. For larger ρ, the difference in critical patch-length is negligible.

As a final illustration of the effectiveness of the block-pulse method, we compared the full spatial equilibrium-distributions of the original Allee model with those of the ten-step block-pulse model, using the Laplace kernel, for a given L and ρ value (fig. 3.16). In particular, we chose $L = 2$ and $\rho = 2.2$ for comparison to fig. 3.15b, where we see the block-pulse model has one-level,

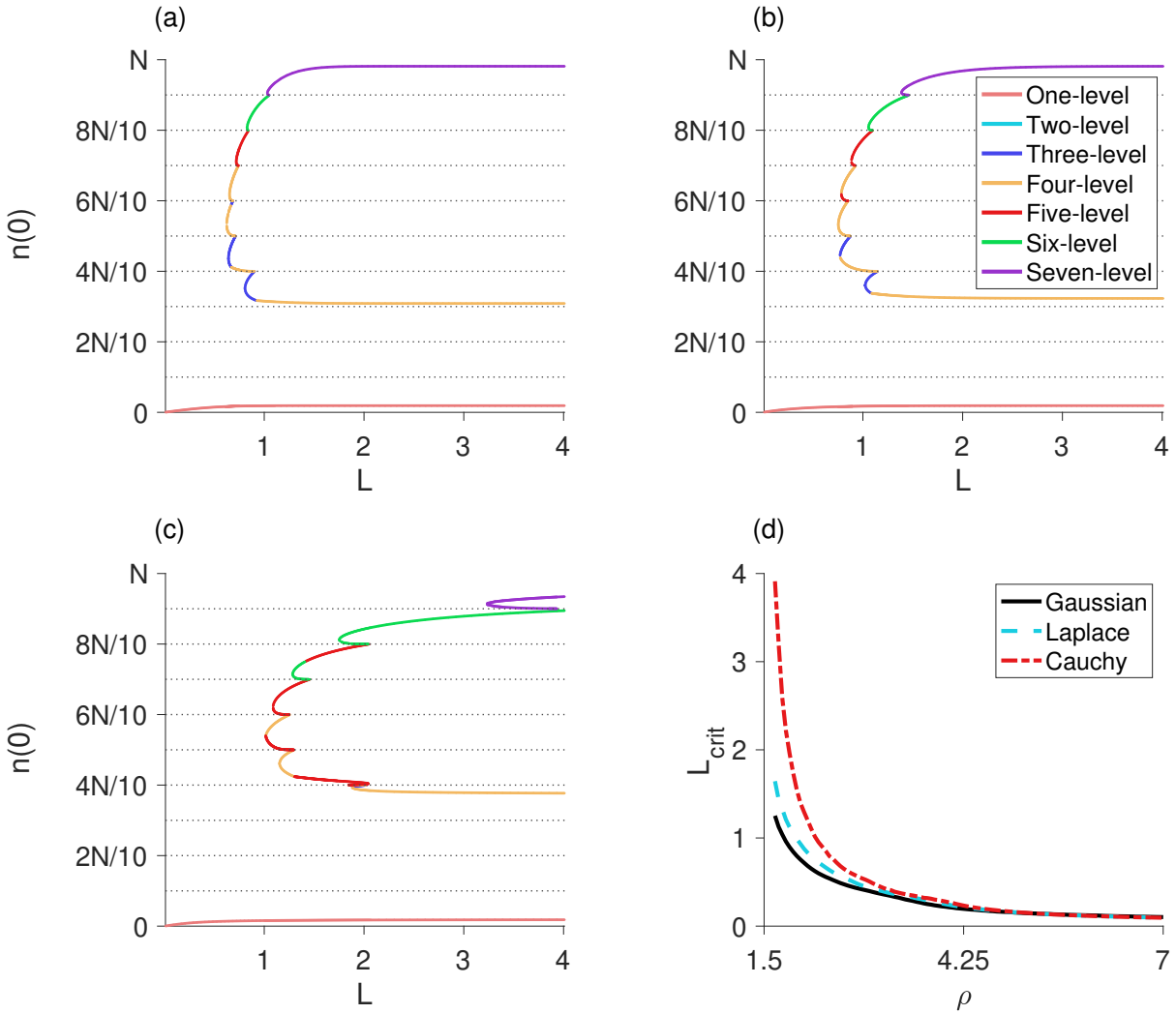

Fig. 3.15 The maximum population-density as L varies for a ten-step block-pulse model with a **a** Gaussian, **b** Laplace, **c** Cauchy dispersal kernel, where $\rho = 2.2$. In **d**, the critical patch-size for population persistence is shown for the three dispersal kernels for varying growth-parameters ρ. To compare the three kernels, we used the same median absolute deviation (MAD) as a measure of dispersion. Parameters values are $N = 1$, $K = 1$, $\alpha = 5$, $\eta = 0.05$, MAD $= 0.1386$.

four-level, and seven-level equilibria.

As can be seen in fig. 3.16, the analytic equilibria of the block-pulse model very closely match those of the original Allee model. The stable nontrivial equilibrium, in particular, is nearly indis-

tinguishable between the two models. Thus, even for equilibrium population-distributions which vary significantly over their habitat patch, the block-pulse method offers close approximations to the full distributions. Furthermore, the block-pulse model reliably approximates distributions with different qualitative shapes, as with the two nontrivial equilibria in fig. 3.16.

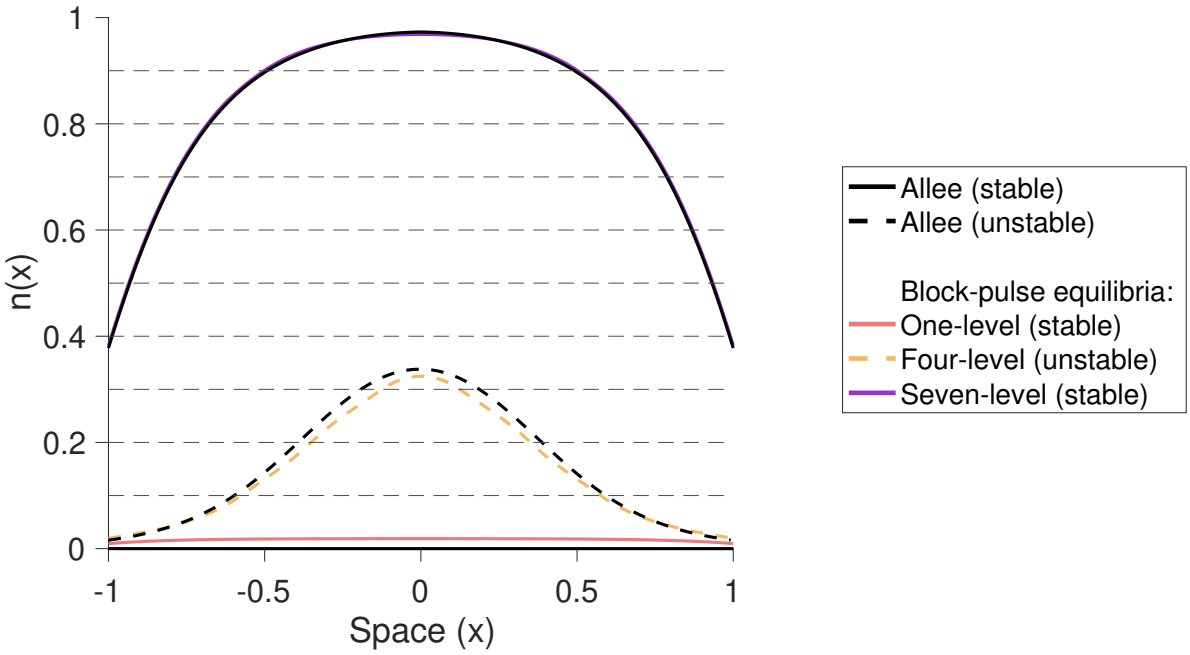

Fig. 3.16 The full spatial equilibrium-distributions of the original Allee model compared to the block-pulse model, using the Laplace kernel, for $\rho = 2.2$ and $L = 2$. For the block-pulse model, these are the full equilibrium-distributions corresponding to the maximum population-densities at $L = 2$ shown in fig. 3.15b. Stable equilibria are shown with solid curves; unstable equilibria are shown with dashed curves. Other parameter values are $N = 1$, $K = 1$, $\alpha = 5$.

3.6 Discussion

In this work, we have presented a simple method of approximating the growth function in an IDE model to make analysis more tractable. The resulting block-pulse IDE has explicit analytic expressions for the iterates and equilibrium distributions of the model. For a small number of steps

in the block-pulse series, we have fully described the possible equilibrium-solution behavior that emerges. These models have numerous different forms of equilibrium distributions, depending on how many density thresholds the population distributions pass through inside the spatial domain. These equilibria tend to merge with the neighboring equilibria, transitioning smoothly from one equilibrium type to the next as the population dips below a threshold at the edge of its habitat or rises above another threshold in the center of its patch.

Fold bifurcations are common features, where two new branches of equilibria emerge as a growth parameter increases. As that parameter increases further, fold bifurcations in which two equilibria collide also occur, resulting in the abrupt loss of two equilibrium distributions. Stability of the equilibria seems to follow a predictable pattern. All one-level equilibria are stable. If two equilibria emerge from a fold bifurcation, the upper equilibrium is stable and the lower equilibrium is unstable. No two neighboring equilibrium-distributions have the same stability.

Block-pulse IDEs are generalizable to any increasing growth-function, given certain assumptions about the dispersal kernel and initial population-distributions. Thus, block-pulse IDEs are a highly useful method for analyzing many forms of population growth. Many methods exist for approximating equilibrium distributions and analyzing population persistence in IDEs, but these largely use approximations of or special forms of the dispersal kernel [65, 139, 85, 63, 110]. In contrast, this is a novel formalization for a method that approximates the growth function in the IDE, though there are a few prior examples of piecewise-constant growth-functions in IDE models [65, 99, 96].

Block-pulse IDEs have a number of advantages inherent in their formulation. Chief among these is the ability to write down simple analytic expressions for the iterates of the model. Using these analytic expressions, we may obtain both unstable and stable equilibria of the block-pulse model. Furthermore, the equilibria of the block-pulse IDEs offer remarkably good approximations to the equilibria of the original models for only a modest number of terms in the block-pulse series. It is also straightforward to continually improve accuracy of the approximations by simply

increasing the number of steps m in the model.

The analytic equilibrium expressions of the block-pulse IDE rely on the spatial-threshold fixed-points, which are found by solving a nonlinear system of implicit equations. To solve this system, we use a root-finding method. Other root-finding methods for finding the solutions of nonlinear operators, like IDEs, exist and have been in use for many years [107, 67, 54, 148, 60, 104]. However, these methods are chiefly numerical and require solving for the population density at every location in the spatial domain.

In contrast, a block-pulse IDE is a hybrid method that is primarily analytical, with a small numerical element. The numerical component requires solving for only a small number of spatial-threshold points, making this method computationally efficient compared to root-finding for operator equations. The block-pulse method also offers insight into the nature of the equilibrium distributions, showing the spatial variation of the equilibrium densities and how this variation changes with a parameter of the model. Furthermore, we may classify stability of the block-pulse equilibria, whereas the root-finding methods do not allow for stability analyses.

We also note the effectiveness of using a block-pulse approximation to approach IDEs with an Allee effect, a class of models which have long been challenging to investigate. In the invasion problem on the infinite domain, there are numerous prior works investigating Allee effects both analytically and numerically [83, 65, 141, 143, 36, 52, 45, 130, 96]. However, on a finite domain, aside from Van Kirk and Lewis [139] there is little research on the impact of an Allee effect in an IDE model save for some numerical experiments [34, 48]. Block-pulse IDEs, therefore, offer a new method to explore Allee effects in IDEs.

We draw particular attention to the possibility of using block-pulse IDEs to estimate the critical patch-size L beyond which a stable persistence-state is possible. In general, the critical patch-size problem assumes there is no Allee effect [84]. However, as seen in fig. 3.15, we may estimate this critical patch-size by finding the smallest L such that a stable, nontrivial equilibrium exists.

Crucially, the critical patch-size appears to be somewhat sensitive to the choice of dispersal

kernel at smaller growth-parameters, particularly if the kernel is heavy-tailed like the Cauchy kernel. This is in contrast to the result for models without an Allee effect, where critical patch-size does not depend significantly on the shape of the kernel for symmetric dispersal [82, 84]. Thus, for kernels with heavier tails, the increased amount of long-distance dispersal may result in the population being pushed below the Allee threshold over a large enough portion of the habitat patch that extinction occurs.

As mentioned previously, block-pulse expansions may be applied to the dispersal kernel as well as, or instead of, to the growth function. For models with no Allee effect, the classic eigenvalue problem that emerges when studying the critical patch-size problem [154, 84] could potentially be analyzed by use of block-pulse expansions for the kernel as an alternative to current methods.

As we have noted already, block-pulse IDEs are a complementary approach to methods like average dispersal-success or geometric symmetrization, differing in which component of the IDE is approximated. Average dispersal-success, in particular, provides a leading-order approximation to the equilibrium population-size. If we were to combine the two approaches, using block-pulse functions for both the growth functions and to expand the kernel, we could feasibly obtain higher-order approximations to the equilibrium-solution distributions with a "full" block-pulse model where the entire integrand has been approximated by block-pulse functions.

Despite the advantages to block-pulse models, there are limitations of the current method. Any ecologically sound growth-function would have $g(0) = 0$, so that a population cannot grow from nothing. The block-pulse framework, however, does not include this feature, so that extinction is never possible. Assuming the original growth-function does satisfy $g(0) = 0$, we observe that as the number of steps m increase in the block-pulse model, we will have $g_1 \to 0$. An expedient solution therefore would be to set $g_1 = 0$ in the current model, rather than computing g_1 according to eq. (3.4). Alternatively, the definition of the subintervals in the block-pulse series could be adjusted to restrict $g(0) = 0$, though both options would take us away from the conventional definition of a block-pulse series.

The required assumptions about unimodality and symmetry in the dispersal kernels and population distributions restrict the types of problems this method can currently be used to analyze. Adapting the block-pulse framework to allow for asymmetric kernels and population distributions would be of immense benefit. Many current problems in spatial ecology, such as determining the speed of spread or finding conditions for population persistence in a moving habitat, have asymmetric population-distributions that our current model does not account for. If the restrictions on symmetry and unimodality can be loosened, we believe the block-pulse IDE may become even more useful.

Studying spreading rates with asymmetric dispersal would be valuable. However, an early example of piecewise-constant growth-functions in an IDE was for a species with an Allee effect, examining symmetric spatial spread from a point release in an infinite habitat [65]. In theory, we may be able to generalize an m-step block-pulse formulation for the same problem to gain deeper insight into spread rates for models with Allee effects, extending the finite habitat-patch framework.

Finally, a key extension of the model is to use block-pulse IDEs in a two-species model that incorporates species interaction, with two-dimensional block-pulse approximations used for the growth functions. This method may be of particular use in the case that one or both species have an Allee effect in their growth.

Along with being useful as an approximation method, block-pulse IDEs proved to be compelling in their own right, with remarkably rich dynamics for even the two- and three-step models. These models can shed light on spatial variation and stability of equilibrium distributions, and may be used to identify critical parameters for population persistence. Our work here formalizes this class of IDEs, providing a novel method to examine the behavior of spatiotemporal population models.

Appendices

A.3 Two-level stability analysis

A.3.1 Conditions for stability of two-level equilibria

We have already seen that in the two-step and three-step models, all of the one-level equilibria are stable. This leaves the two-level and three-level equilibria, where we analyze the stability of the spatial-threshold fixed-points r_i as a proxy for stability of the full equilibrium-solution.

The bridge equilibrium from section 3.4.2 and the low-bridge and high-bridge equilibria from section 3.4.3 share many features. We first introduce a few key expressions that will be used in analyzing stability of all of these equilibria, that is, all the two-level equilibria.

First, we note that the derivatives r_i', $i = 1,2$, given in eq. (3.35) and eq. (3.43) have the same general form. The magnitude of these derivatives governs stability of the two-level equilibria. Both numerator and denominator of eq. (3.35) and eq. (3.43) are negative, so the derivative is positive for the two-level equilibria. Thus, if $0 < r_i' < 1$, the fixed point is stable; if $r_i' > 1$, the fixed point is unstable.

For $i = 1,2$, the derivative $r_i' = 1$ exactly if

$$g_i\left[k\left(r_i + L/2\right) - k\left(r_i - L/2\right)\right] + 2\left(g_{i+1} - g_i\right)k\left(2r_i\right) = 0. \tag{A1}$$

If the left hand side of eq. (A1) is positive, the equilibrium is unstable; if it is negative, the equilibrium is stable. We may rewrite this condition so that the derivative is equal to one if

$$g_i = \frac{-2g_{i+1}k\left(2r_i\right)}{k\left(r_i + L/2\right) - k\left(r_i - L/2\right) - 2k\left(2r_i\right)} = g^*. \tag{A2}$$

for some r_i. If $g_i < g^*$, the two-level equilibrium is unstable. If $g_i > g^*$, the two-level equilibrium is stable.

The derivative of g^* with respect to r_i is negative everywhere, and so g^* is a decreasing function of r_i. The maximum value of g^* is at $r_i = 0$, so that

$$g^*_{\max} = \frac{-2g_{i+1}k\left(0\right)}{k\left(L/2\right) - k\left(-L/2\right) - 2k\left(0\right)} = g_{i+1}, \tag{A3}$$

where the second equality follows from the symmetry of the dispersal kernel, with $k(L/2) = k(-L/2)$. The minimum value of g^* is at $r_i = L/2$, with

$$g^*_{\min} = \frac{2g_{i+1}k(L)}{k(L)+k(0)}. \tag{A4}$$

A.3.2 Bridge equilibrium

There are three distinct parameter regimes for the bridge equilibrium of the two-step model, summarized in table 3.1. We approach stability of the bridge equilibria for each regime separately. The expressions from eqs. (A1) to (A4) are applied with $i = 1$.

First region: small g_1

In the first region, $g_1 < g_s$ and $g_2 > g_b$. We note that

$$g_2 > g_b = \frac{N/2}{F(L) - F(0)}, \tag{A5}$$

so that

$$g^*_{\min} = \frac{2g_2k(L)}{k(L)+k(0)} > \frac{Nk(L)}{[F(L)-F(0)][k(L)+k(0)]} = g_s. \tag{A6}$$

Thus, $g_1 < g_s < g^*_{\min}$ for all $r_1 \in (0,\, L/2)$. Therefore, the bridge equilibrium is unstable in this parameter regime.

Second region: moderate g_1

In the second region where $g_s < g_1 < g_a$ and $g_1 < g_2 < g_c$, there are two r_1 equilibria, as seen earlier. We prove this explicitly by showing there is some r_1 value where $r_1' = 1$ and a fold bifurcation occurs in this parameter region.

First, note that at $r_1 = 0$, $g_1 < g^*_{\max} = g_2$. Thus, the left-hand side of eq. (A1) is clearly positive and the equilibrium is unstable. At $r_1 = L/2$, $g_2 = g_b$ and so $g^*_{\min} = g_s$. As $g_1 > g_s$ in this parameter regime, we have $g_1 > g^*_{\min}$. Thus, the left-hand side of eq. (A1) is negative and the equilibrium is unstable.

Thus, the left-hand side of eq. (A1) goes from positive to negative as r_1 increases. Since g^* is a decreasing function of r_1, there is a a single r_1^* value where the left-hand side of eq. (A1) is equal to zero, and therefore where $r_1' = 1$, leading to a fold bifurcation. For $r_1 < r_1^*$ the equilibria will be unstable; for $r_1 > r_1^*$ the equilibria will be stable. The smaller r_1 correspond to the lower branch of bridge equilibria and the larger r_1 to the upper branch of equilibria, so that the lower branch is unstable and the upper branch is stable.

Third region: large g_1

In the third parameter region, where $g_a < g_1 < g_2 < g_b$, the equilibrium is not valid for all $0 < r_1 < L/2$. Instead, there is some intermediate r_1 value, which we call r_v, where $g_1 = g_2$. For $r_1 < r_v$, $g_2 < g_1$ and the bridge equilibrium is invalid. For $r_v < r_1 < L/2$, the bridge equilibrium is valid.

We suspect the bridge equilibrium to be stable in this region. For this to be the case, we require that $g_1 > g^*$ from eq. (A2) for all $r_v < r_1 < L/2$. As g^* is a decreasing function of r_1, the maximum value g^* can take on while the bridge equilibrium is still valid occurs at $r_1 = r_v$.

Thus, we need $g_1 > g^*(r_1 = r_v)$ for the bridge equilibrium to be stable. Checking this condition and using the fact that $g_1 = g_2$ at r_v, we find that if

$$g^*(r_1 = r_v) = \frac{-2g_1 k(2r_v)}{k(r_v + L/2) - k(r_v - L/2) - 2k(2r_v)} < g_1, \tag{A7}$$

then

$$g_1 [k(r_v + L/2) - k(r_v - L/2) - 2k(2r_v)] < -2g_1 k(2r_v). \tag{A8}$$

Canceling like terms, this means that

$$g_1 [k(r_v + L/2) - k(r_v - L/2)] < 0, \tag{A9}$$

which is clearly satisfied. Therefore, the bridge equilibrium is indeed stable for this parameter regime. This completes our stability analysis for the two-step model.

A.3.3 Low-bridge equilibrium

There are three distinct parameter regimes for the low-bridge equilibrium of the three-step model, summarized in table 3.4. The expressions from eqs. (A1) to (A4) are applied with $i = 1$. The stability analysis is identical to the analysis for the bridge equilibrium, save for the coefficients of the threshold values g_{s_1} and g_b, and so we do not repeat it here.

To summarize, in the first parameter regime where $g_1 < g_{s_1}$ and $g_2 > g_b$, the low-bridge equilibrium is unstable. In the second region where $g_{s_1} < g_1 < g_a$ and $g_1 < g_2$, a fold bifurcation occurs for some critical r_1^* where $r_1' = 1$; for $r_1 < r_1^*$ the equilibria are unstable and for $r_1 > r_1^*$ the equilibria are stable. These are the lower and upper branches of low-bridge equilibria respectively. In the third parameter region where $g_a < g_1 < g_2 < g_b$, the low-bridge equilibrium is stable.

A.3.4 High-bridge equilibrium

For the high-bridge equilibrium of the three-step model, the expressions from eqs. (A1) to (A4) are applied with $i = 2$. As before, we treat the stability for the two parameter regions from table 3.5 separately.

First region: moderate g_3

In the first parameter regime where $g_{s_2} < g_2 < g_d$ and $g_c < g_3 < g_d$, there are two r_2 equilibria. We prove this explicitly by showing there is a fold bifurcation at some r_2 value such that $r_2' = 1$.

At $r_2 = 0$, $g_2 < g^*_{\max} = g_3$. The left-hand side of eq. (A1) is positive and the equilibrium is unstable. At $r_2 = L/2$, $g_3 = g_d$ and $g_2 > g_{s_2} = g^*_{\min}$. The left-hand side of eq. (A1) is negative and the equilibrium is stable.

Thus, a fold bifurcation occurs at some r_2^* where the left-hand side of eq. (A1) is equal to zero and therefore $r_2' = 1$. For $r_2 < r_2^*$, the equilibria are unstable and for $r_2 > r_2^*$ the equilibria are stable. This means that the lower branch of high-bridge equilibria are unstable and the upper branch of equilibria are stable.

Second region: large g_3

In the second region, $g_2 < g_c$ and $g_3 > g_d$ and the high-bridge equilibrium is valid for only some $0 < r_2 < r_v$. For $r_2 > r_v$ we have $g_1 > g_2$. We suspect the high-bridge equilibrium is unstable, so that we should have $g_2 < g^*$.

We drop all subscripts on r for the remainder of this section for notational convenience and to shorten the equations. Using the functional form for g_2 from eq. (3.42), we thus want to show that

$$\frac{2N/3 - g_3 [F(2r) - F(0)]}{F(r+L/2) - F(r-L/2) - F(2r) + F(0)} < \frac{-2g_3 k(2r)}{k(r+L/2) - k(r-L/2) - 2k(2r)}. \tag{A10}$$

Solving the above expression for g_3, for instability of the high-bridge equilibrium we require

$$g_3 > \frac{\frac{2N}{3} [k(r+L/2) - k(r-L/2) - 2k(2r)]}{[F(2r) - F(0)][k(r+L/2) - k(r-L/2)] - 2k(2r)[F(r+L/2) - F(r-L/2)]}. \tag{A11}$$

The above equation is an increasing function of r. This can be confirmed by taking the derivative of the right-hand side with respect to r, and simplifying to find that the derivative is always positive for $0 < r < L/2$. The algebra to show this fact is straightforward but lengthy; we do not include it here.

Since the right-hand side of eq. (A11) is an increasing function of r, the maximum value occurs for $r = L/2$. If g_3 is larger than this maximum value, eq. (A11) will be satisfied for all $0 < r < L/2$. Substituting $r = L/2$ into the right-hand side of eq. (A11), our requirement becomes

$$g_3 > \frac{\frac{2N}{3} [k(L) + k(0)]}{[k(L) + k(0)][F(L) - F(0)]} = \frac{2N/3}{F(L) - F(0)} = g_d. \tag{A12}$$

In this parameter regime, $g_3 > g_d$, and so the requirement is evidently satisfied. Thus, the high-bridge equilibrium is unstable in this parameter regime.

B.3 Three-level stability analysis

The full-bridge equilibrium from the three-step model is a three-level equilibrium. With two spatial thresholds involved in the full-bridge equilibrium, stability is dependent on a two-dimensional

mapping of the spatial thresholds, with the maps given by

$$\begin{aligned} n_{t+1}(r_{1,t+1}) =& g_1 [F(r_{1,t+1}+L/2) - F(r_{1,t+1}-L/2)] \\ &+ (g_2-g_1)[F(r_{1,t+1}+r_{1,t}) - F(r_{1,t+1}-r_{1,t})] \\ &+ (g_3-g_2)[F(r_{1,t+1}+r_{2,t}) - F(r_{1,t+1}-r_{2,t})] = N/3, \end{aligned} \tag{A13}$$

$$\begin{aligned} n_{t+1}(r_{2,t+1}) =& g_1 [F(r_{2,t+1}+L/2) - F(r_{2,t+1}-L/2)] \\ &+ (g_2-g_1)[F(r_{2,t+1}+r_{1,t}) - F(r_{2,t+1}-r_{1,t})] \\ &+ (g_3-g_2)[F(r_{2,t+1}+r_{2,t}) - F(r_{2,t+1}-r_{2,t})] = 2N/3. \end{aligned} \tag{A14}$$

To classify stability, we will compute the Jacobian of this two-dimensional map and analyze the Jury conditions [59]. The Jacobian is given by

$$J = \begin{bmatrix} \frac{n_{11}}{d_1} & \frac{n_{12}}{d_1} \\ \\ \frac{n_{21}}{d_2} & \frac{n_{22}}{d_2} \end{bmatrix}, \tag{A15}$$

where

$$n_{11} = (g_1-g_2)[k(2r_1)+k(0)], \tag{A16}$$

$$n_{12} = (g_2-g_3)[k(r_1+r_2)+k(r_1-r_2)], \tag{A17}$$

$$n_{21} = (g_1-g_2)[k(r_2+r_1)+k(r_2-r_1)], \tag{A18}$$

$$n_{22} = (g_2-g_3)[k(2r_2)+k(0)], \tag{A19}$$

$$\begin{aligned} d_1 =& g_1 [k(r_1+L/2) - k(r_1-L/2)] + (g_2-g_1)[k(2r_1) - k(0)] \\ &+ (g_3-g_2)[k(r_1+r_2) - k(r_1-r_2)], \end{aligned} \tag{A20}$$

and

$$\begin{aligned} d_2 =& g_1\left[k\left(r_2+L/2\right)-k\left(r_2-L/2\right)\right]+\left(g_2-g_1\right)\left[k\left(r_2+r_1\right)-k\left(r_2-r_1\right)\right] \\ &+\left(g_3-g_2\right)\left[k\left(2r_2\right)-k\left(0\right)\right]. \end{aligned} \tag{A21}$$

Notice that the numerators and denominators in the Jacobian are all negative, so that every term in the Jacobian is positive. The three Jury conditions involve the trace and determinant, τ and Δ, of the Jacobian, where

$$\tau = \frac{n_{11}}{d_1}+\frac{n_{22}}{d_2} \tag{A22}$$

and

$$\Delta = \frac{n_{11}n_{22}}{d_1 d_2}-\frac{n_{12}n_{21}}{d_1 d_2}. \tag{A23}$$

First, we consider the Jury conditions that are not violated. The second Jury condition, $1+\tau+\Delta>0$, is always satisfied. Writing everything in a common denominator, we have

$$1+\tau+\Delta = \frac{d_1 d_2+n_{11}d_2+n_{22}d_1+n_{11}n_{22}-n_{12}n_{21}}{d_1 d_2}. \tag{A24}$$

As each n_{ij} and d_i is negative, their products are positive and all of the terms in the numerator of eq. (A24) are positive except for the last, $-n_{12}n_{21}$. The denominator is positive. Thus, we need to show that the single negative term in the numerator is less than all the other terms.

To show the numerator of the second Jury condition is positive, we notice that $-n_{12}n_{21}$ has the positive factor $\left(g_1-g_2\right)\left(g_2-g_3\right)$. We look for other terms in the numerator with this factor, and show that the sum of all terms with the factor $\left(g_1-g_2\right)\left(g_2-g_3\right)$ is positive, which is sufficient to demonstrate the numerator as a whole is positive. Collecting these terms, for the numerator of the second Jury condition to be positive we need

$$\begin{aligned} &\left[k\left(0\right)-k\left(2r_1\right)\right]\left[k\left(0\right)-k\left(2r_2\right)\right]+\left[k\left(r_1-r_2\right)-k\left(r_1+r_2\right)\right]\left[k\left(r_2-r_1\right)-k\left(r_2+r_1\right)\right] \\ &+\left[k\left(2r_1\right)+k\left(0\right)\right]\left[k\left(2r_2\right)+k\left(0\right)\right]-\left[k\left(r_1+r_2\right)+k\left(r_1-r_2\right)\right]\left[k\left(r_2+r_1\right)+k\left(r_2-r_1\right)\right] \\ &+\left[k\left(2r_1\right)+k\left(0\right)\right]\left[k\left(0\right)-k\left(2r_2\right)\right]+\left[k\left(2r_2\right)+k\left(0\right)\right]\left[k\left(0\right)-k\left(2r_1\right)\right]>0. \end{aligned} \tag{A25}$$

Since we assume the kernel is symmetric, $k(r_1+r_2) = k(r_2+r_1)$ and $k(r_1-r_2) = k(r_2-r_1)$. Expanding and canceling like terms, the above condition becomes

$$k^2(0) > k(r_1+r_2)\,k(r_1-r_2), \tag{A26}$$

which is evidently true. Thus, $1+\tau+\Delta > 0$ and the second Jury condition is always satisfied.

The third Jury condition, $|\Delta| < 1$, is not applicable here, as it deals with complex eigenvalues. The eigenvalues of this system are real. We show this by computing the eigenvalues of the Jacobian using the characteristic equation $\lambda^2 - \tau\lambda + \Delta = 0$, so that the eigenvalues are

$$\lambda_{1,2} = \frac{1}{2}\left(\tau \pm \sqrt{\tau^2 - 4\Delta}\right). \tag{A27}$$

If the discriminant $\tau^2 - 4\Delta > 0$, then the eigenvalues are real and we do not need to check the third Jury condition. We have

$$\begin{aligned}\tau^2 - 4\Delta &= \left(\frac{n_{11}}{d_1} + \frac{n_{22}}{d_2}\right)^2 - 4\frac{n_{11}n_{22}}{d_1 d_2} + 4\frac{n_{12}n_{21}}{d_1 d_2} \\ &= \left(\frac{n_{11}}{d_1} - \frac{n_{22}}{d_2}\right)^2 + 4\frac{n_{12}n_{21}}{d_1 d_2} > 0.\end{aligned} \tag{A28}$$

Therefore, we have real eigenvalues and the third Jury condition will never be violated.

Finally, the first Jury condition, $1-\tau+\Delta > 0$, may be violated. This is clearly demonstrated in fig. 3.10, where we observe a fold bifurcation in the full-bridge equilibrium. In practice, this condition is largely useful in checking specific full-bridge equilibria for stability. Numerical experiments testing the first Jury condition for 80 parameter sets with full-bridge equilibria demonstrated that the upper branch of equilibria is stable, while the lower branch is unstable, just as in the low-bridge and high-bridge equilibria when a fold bifurcation occurred.

C.3 Behavior of g_2 in the low-bridge and high-bridge equilibria

C.3.1 Low-bridge equilibrium

The function for g_2 from eq. (3.41) behaves nearly identically to that of the analogous function for the bridge equilibrium from section 3.4.2. At $r_1 = 0$, the low-bridge equilibrium meets the low

equilibrium and $g_2 \to \pm\infty$. At $r_1 = L/2$, the low-bridge equilibrium meets the middle equilibrium at $g_2 = g_b$. Equation (3.41) may also be multi- or single-valued in r_1.

For small g_1, the function for g_2 is single-valued with $g_2 \to \infty$ as $r_1 \to 0$ (see fig. 3.11). Therefore, we have a single low-bridge equilibrium valid for $g_2 > g_b$.

As g_1 increases through the limit $g_1 = g_{s_1}$ (see table 3.3), eq. (3.41) becomes multivalued (we again use a subscript s to denote that this is a switching point in the behavior of a single equilibrium; there is a second analogous switching-point for the high-bridge equilibrium). Now, $g_2 \to \infty$ and there are two r_1 solutions for some $g_2 < g_b$ (see figs. 3.8 and 3.9). There will be two low-bridge equilibria for $g_2 < g_b$. One of these terminates at $g_2 = g_b$, leaving one remaining low-bridge equilibrium for $g_2 > g_b$.

As g_1 further increases through g_a, the function becomes single-valued again with $g_2 \to -\infty$; the actual lower limit for g_2 is g_1 (see fig. 3.10). There is one low-bridge equilibrium for $g_1 < g_2 < g_b$. For $g_1 > g_b$, the equilibrium becomes invalid as $g_1 > g_2$.

C.3.2 High-bridge equilibrium

For the function for g_2 from eq. (3.42), similar behavior as that of the function from section C.3.1 occurs. At $r_2 = 0$, the high-bridge and middle equilibria meet at $g_2 = g_c$. At $r_2 = L/2$, the high-bridge equilibrium meets the high equilibrium and $g_2 \to \pm\infty$ depending on the value of g_3. The function may have one or two branches.

For $g_3 < g_c$, $g_2 > g_3$ and the high-bridge equilibrium is not valid. For $g_c < g_3 < g_d$, the function for g_2 has two branches, with $g_2 \to \infty$ (figs. 3.8 to 3.10). There are two high-bridge equilibria for some $g_2 < g_c$; for $g_2 > g_c$ only one equilibria remains. The lower bound in g_2 ranges from $g_2 = g_{s_2}$ up to $g_2 = g_c$. For $g_3 > g_d$, the function for g_2 is single-valued with $g_2 \to -\infty$; the lower limit of g_2 is effectively g_1 (fig. 3.11). There is a single high-bridge equilibrium valid for $g_1 < g_2 < g_c$.

D.3 Convergence of the block-pulse IDE

The equilibria found for the block-pulse model converge to the equilibria of the original model as $m \to \infty$, under certain broad conditions. To begin, we introduce Riemann–Stieltjes sums and Riemann–Stieltjes integrals, taking the definitions from Apostol [4].

Let $P = \{y_0, y_1, y_2, ..., y_M\}$ be a partition of the compact interval $[a,b]$, and let w_i be a point in the subinterval $[y_{i-1}, y_i]$. Then, the sum

$$S(P,f,\alpha) = \sum_{i=1}^{M} f(w_i)\,\Delta\alpha_i \tag{A29}$$

is a Riemann–Stieltjes sum of the function f with respect to α, where $\Delta\alpha_i = \alpha(y_i) - \alpha(y_{i-1})$. The function f is Riemann-integrable with respect to α on $[a,b]$ if there exists a number A such that for every $\varepsilon > 0$, there exists a partition P_ε of $[a,b]$ such that for every partition P finer than P_ε and for every choice of the points $w_i \in [y_{i-1}, y_i]$ we have $|S(P,f,\alpha) - A| < \varepsilon$. This number A, if it exists, is unique and it is known as the Riemann–Stieltjes integral,

$$A = \int_a^b f(y)\,d\alpha(y). \tag{A30}$$

In other words, if the Riemann–Stieltjes integral exists, i.e., if $f(y)$ is Riemann-integrable with respect to $\alpha(y)$, then as the mesh of P denoted by $\|P\|$ goes to zero, the Riemann–Stieltjes sum is equal to the Riemann–Stieltjes integral so that

$$\lim_{\|P\|\to 0} \sum_{i=1}^{M} f(w_i)\,\Delta\alpha_i = \int_a^b f(y)\,d\alpha(y). \tag{A31}$$

In order for the Riemann–Stieltjes integral to exist it is sufficient that $f(y)$ is continuous on $[a,b]$ and that $\alpha(y)$ is monotone increasing or, more generally, of bounded variation on $[a,b]$.

Furthermore, if $\alpha(y)$ has a continuous derivative $\alpha'(y)$ so that $\alpha'(y)$ is Riemann-integrable, then the Riemann–Stieltjes integral can be written as a Riemann integral as

$$\int_a^b f(y)\,d\alpha(y) = \int_a^b f(y)\,\alpha'(y)\,dy. \tag{A32}$$

Now, note that the equilibria $n(x)$ of the original IDE model satisfy

$$n(x) = \int_{-L/2}^{L/2} k(x-y)\, g[n(y)]\, dy, \tag{A33}$$

where the integral on the right has the form of a Riemann–Stieltjes integral with $[a,b] = [-L/2, L/2]$, $f(y) = g[n(y)]$ and $d\alpha(y) = \alpha'(y)\, dy = k(x-y)\, dy$. After accounting for the $-y$ argument in the dispersal kernel, we have $\alpha(y) = -F(x-y)$. The growth function is assumed to be continuous, and the cumulative distribution function (and its negative) is monotone and therefore of bounded variation. Thus, this Riemann–Stieltjes integral exists, and is equal to the limit of the Riemann–Stieltjes sum as the mesh of the partition P for the sum goes to zero.

The Riemann–Stieltjes sum for the above Riemann–Stieltjes integral has the general form

$$S(P, g, F) = \sum_{i=1}^{M} g(w_i)\left[F(x-y_{i-1}) - F(x-y_i)\right], \tag{A34}$$

after making the appropriate substitutions for f and α in eq. (A29). Choose a partition on the compact interval $[-L/2, L/2]$ to be $P = \{y_0, y_1, y_2, ..., y_M\} = \{-L/2, -r_1, -r_2, ..., r_2, r_1, L/2\}$, where r_i are the equilibrium spatial-thresholds for a given m-step block-pulse IDE and $M = 2m-1$.

Recall that each spatial threshold corresponds to a density threshold, so that each subinterval of the partition P corresponds to a subinterval of the population density where the growth function is between two density thresholds. Given that the block-pulse coefficients from eq. (3.4) are the averages of the growth function $g[n(y)]$ over each subinterval of population density, we may safely choose w_i in each subinterval of the partition so that

$$g(w_i) = \begin{cases} g_i, & i = 1, 2, ..., \frac{M+1}{2}, \\ g_{M-i+1}, & i = \frac{M+3}{2}, ..., M-1, M, \end{cases} \tag{A35}$$

given our prior assumptions on the growth function and dispersal kernel. After some rearranging, eq. (A34) has the same form as eq. (3.51) (with $p = m$ and $q = 1$). The block-pulse approximation is in fact a Riemann–Stieltjes sum corresponding to the Riemann–Stieltjes integral for the original equilibria. Since this integral exists, as the partition becomes finer, we know that the sum will

approach the integral. For the partition to become finer, $m \to \infty$, so that as $m \to \infty$, the block pulse equilibria are the original equilibria.

To rigorously show that the block-pulse equilibria converge to the true equilibria, consider the sequence $\{G_m\}$ of functions given by partial sums, where G_m represents the m-step block-pulse partial sum,

$$G_m = \sum_{i=1}^{m} g_i \phi_i [n(y)]. \tag{A36}$$

We know that the block-pulse series converges pointwise to $g[n(y)]$ as $m \to \infty$, so that the sequence $\{G_m\}$ converges pointwise to $g[n(y)]$ as $m \to \infty$. We note that the sequence $\{G_m\}$ is uniformly bounded by $|G_m[n(y)]| \leq N$ for all m and all $y \in [-L/2, L/2]$, where N was taken to be a finite limit on population density. Thus, since $\{G_m\}$ is pointwise convergent and uniformly bounded, the sequence is boundedly convergent for $y \in [-L/2, L/2]$.

We recall that $F(x-y)$ is of bounded variation, and note that the integrand of

$$n(x) = \int_{-L/2}^{L/2} G_m[n(y)] k(x-y)\, dy \tag{A37}$$

is Riemann-integrable and therefore the integral exists. We have already demonstrated that

$$n(x) = \int_{-L/2}^{L/2} g[n(y)] k(x-y)\, dy \tag{A38}$$

exists.

We therefore satisfy the conditions for the bounded convergence theorem for the Riemann–Stieltjes integral [49, 94], an extension of Arzelà's bounded convergence theorem [4]. By the bounded convergence theorem for Riemann–Stieltjes integrals,

$$\lim_{m\to\infty} \int_{-L/2}^{L/2} G_m[n(y)] k(x-y)\, dy = \int_{-L/2}^{L/2} g[n(y)] k(x-y)\, dy, \tag{A39}$$

so that the block-pulse equilibria converge to the equilibria of the original model. For proof and further discussion of Arzelà's bounded convergence theorem for integrals of Riemann–Stieltjes form, see Hildebrandt [49], Luxemburg [87], Monteiro et al. [93, 94].

Chapter 4
DISCUSSION

This body of work was inspired by a drive to better understand population dynamics and the ability of a population to persist, a firm belief in the benefit of interdisciplinary research and communication, and a sense of curiosity about the natural world. While this research is theoretical in nature, it offers conceptual insights into population behavior. The models themselves may also be parameterized for populations that satisfy the underlying biological assumptions. At its heart, this dissertation does not attempt to conclusively answer questions of population persistence, but seeks to add another drop of knowledge to to the immense body of work on problems in spatial ecology. Taken together, this cohesive body of knowledge continues to improve our understanding of population dynamics and, together, allows us to work towards preservation of the natural world.

4.1 Competition in successional communities

First, I sought to comprehensively examine how a pioneer–climax system of plants might respond to competitive interactions when growth occurs in discrete, synchronized intervals. Ecological intuition suggests that a climax species would naturally outcompete the pioneer species; however, the mathematical predictions conclude that there are a variety of parameter regimes under which the climax population is excluded. Furthermore, stable coexistence of both pioneer and climax populations is frequently possible, both at fixed population-densities and fluctuating cycles of densities.

With this potential disparity between mathematical insight and ecological reasoning, an interdisciplinary venture would be beneficial. Ecological timescales are often vast, and historical records may be patchy or nonexistent, making it challenging to make definitive empirical statements regarding long-term behavior in some systems. Parameterizing the pioneer–climax model

with existing data or performing small-scale lab experiments to test model predictions could offer an explanation of the frequency of scenarios in which pioneer exclusion was not the only viable long-term behavior. This would also have the benefit of making the model more immediately applicable.

A pioneer–climax model that incorporates spatial components would be constructive as well. If the pioneer occupies a small refuge-patch at the edges of the habitat, or the populations are otherwise spatially non-uniform, this may be an additional route towards coexistence or pioneer persistence. I have also postulated that, with increasing habitat-disturbance and range shifts caused by climate change, successional communities will become more common. These are naturally spatial considerations.

4.2 Allee effects in moving-habitat models

Initially, my work attempted to build a spatial pioneer–climax model from the nonspatial model. In particular, I wished to estimate the conditions required for population persistence when the habitat patches were shifting. To do so, I applied an existing method known as geometric symmetrization to a moving-habitat pioneer–climax model. Geometric symmetrization has been suitable for single-species models [113] as well as competition [114] and host–parasitoid models [89]. None of the models on which geometric symmetrization had been used had an Allee effect.

The climax population, however, is subject to a strong Allee effect, and initial exploration of a climax-only model revealed that this effect caused the approximations of critical speed to be wholly inaccurate when compared to numerical simulations, both quantitatively and qualitatively. Gradually reducing the strength of the Allee effect to a weak Allee effect and then to no Allee effect at all indicated that the Allee effect was the underlying problem in the method's poor predictions. Critical-speed estimates improved somewhat as the strength of the Allee effect decreased, and when there was no Allee effect, there was quantitative agreement with numerical simulations in line with what we might expect based on previous applications of geometric symmetrization.

To confirm that the issue was not exacerbated by removing the population interactions between pioneer and climax species, I also briefly explored geometric symmetrization applied to a pioneer–climax moving-habitat model. Similar results occurred for this model, with predictions of critical speeds for climax persistence being very poor compared to numerically simulated critical-speeds.

Though there are heuristic explanations as to why geometric symmetrization works, no formal analytical explanation exists [84]. As a result, it is also challenging to identify precisely why geometric symmetrization was ineffective for a model with an Allee effect. At its core, geometric symmetrization is a linearization method. With significantly nonlinear dynamics in a typical model with Allee growth, it seems likely that the process of linearization is simply insufficient to capture the true behavior of the model, particularly when dispersal is asymmetric.

Prior to linearization, a key component of geometric symmetrization involves spatially averaging the population distributions to ultimately reduce the IDE model a spatially-implicit difference-equation model, and I suspect this may also be part of the problem when an Allee effect is involved. The spatial distribution of a population plays an important role when there is an Allee effect, particularly with a strong Allee effect, as populations may be below the Allee threshold in some areas of the patch and above it in others. As the shifting habitat-patch introduces asymmetry into the spatial distributions, knowledge of where the population is above or below the threshold is particularly important to understanding persistence, and spatially averaging the populations disregards this information entirely.

4.3 Methods for integrodifference equations

With this result for the moving-habitat model, I sought to explore alternate methods of approaching a general IDE with an Allee effect. Both geometric symmetrization and the closely-related average dispersal-success approximation involve approximating the integral operator for the kernel. As a complementary but alternate approach, I approximated the nonlinear growth-function instead. A variety of possible approximations to the growth function were explored, before land-

ing on a piecewise-constant approximation using block-pulse functions. Block-pulse functions have an established framework, simple construction, and ease of use that made them appealing as the method of choice. Furthermore, under our construction, block-pulse IDEs are useful not just for Allee-effect growth, but for any strictly-increasing growth-function.

The insights gained with block-pulse IDEs are compelling. With a moderate number of steps in the piecewise-constant approximation, the equilibrium distributions of the block-pulse IDEs closely match the true equilibria. We also gain a wealth of knowledge about the equilibria themselves, including information about stability and spatial variation of the distributions. In their current form, we may use block-pulse IDEs to examine population persistence on a finite habitat-patch, a problem which is particularly relevant in the context of habitat fragmentation. Of particular note, the critical patch-sizes predicted for a model with an Allee effect are sensitive to the choice of dispersal kernel. On the whole, block-pulse IDEs offer a novel method for approaching analysis of IDEs, and in particular, examining IDEs with Allee effects.

4.4 Block-pulse IDEs, pioneer–climax systems, and the path forward

The future applicability and connections that may be made using block-pulse IDEs are just as intriguing as the current results from block-pulse IDEs. To extend the current framework, loosening the restrictions on symmetry and unimodality in the kernel and population distributions is especially pertinent. This would allow us to use the analytic framework for block-pulse IDEs with asymmetric kernels and non-monotone growth-functions as well. Asymmetric kernels arise in many applications, including in the moving-habitat models discussed earlier. By accounting for non-monotone growth-functions, we may consider overcompensatory growth and further increase the method's overall applicability.

If we wanted to maintain unimodality of the population distributions but not require symmetry of the kernel or population distributions, we would need an alternate condition to ensure the convolution of the two distributions is unimodal. If at least one of the distributions is log-concave

and both are unimodal, then the convolution of the distributions is unimodal [55]. While many dispersal kernels are log-concave, many fat-tailed dispersal kernels, including the Cauchy kernel, are not. Ecologists increasingly embrace fat-tailed kernels to model population dispersal, and so this loss is not insignificant. Thus, while removing the restriction that the distributions must be symmetric would increase the applicability of block-pulse IDEs in terms of ecological problems we may examine, it comes with the tradeoff of limiting the dispersal kernels we may consider.

The symmetry and unimodality of the population distributions are at the heart of many of the analytic results of block-pulse IDEs. Without symmetry of the population distributions, we also lose symmetry of the spatial thresholds where a population passes through a density threshold. Thus, we would need to solve for up to twice the number of spatial thresholds as in the current framework. Without unimodality, the matter is complicated even further, as we may have more than two spatial thresholds for each density threshold.

Nevertheless, note that a block-pulse IDE may be applied in its current form even to asymmetric or multimodal population-distributions. This may be done by iterating the model using cumulative distribution functions and numerically finding the spatial thresholds at each iterate, rather than relying on the analytic expressions for the equilibria presented in chapter 3.

Kot et al. [65] used a two-step piecewise-constant approximation for an IDE with strong Allee effect to estimate the rate of spread of a population on an infinite habitat. This work provided early inspiration for the block-pulse IDE framework developed here, and engenders a natural extension of using block-pulse IDEs to analyze the point-release invasion of a population with an Allee effect. In this problem, rather than finding equilibrium spatial-thresholds, we would track the thresholds through space. On the surface, there is no indication whether these thresholds would move at the same speeds, which may be a complicating factor.

I began this work with a pioneer–climax system and, as already mentioned, intended to examine that system in a moving-habitat model. With loosened restrictions on symmetry and unimodality of the population distributions, we may feasibly use a block-pulse framework to examine the critical

speed of range shifts, returning to my original intent. A block-pulse IDE could be used to estimate critical speeds for both a climax population on its own as well as a pioneer–climax system, given a two-dimensional block-pulse function. This is, perhaps, the problem that most fascinates me. How does the Allee effect influence the critical speed of range shifts? How do the critical speeds for each population differ from each other? What is the impact of habitat arrangement on the critical speeds?

Beyond these questions relating block-pulse IDEs in their current form to the pioneer–climax system, block-pulse functions may be used to expand the kernel as well. If we can answer the critical-speed problem using block-pulse functions on the growth function, can we improve the critical-speed estimates by using a block-pulse expansion of the asymmetric kernel? What happens if we expand the symmetrized kernel from geometric symmetrization with block-pulse functions?

Ultimately, no piece of research can ever answer all the questions we might have. This is extraordinarily clear in this dissertation, which ends in a place that may allow me to return to the questions I began with. The twists and turns taken in this research highlight the limitations of mathematical models, which sometimes cannot answer the questions we wish to explore even after making great simplifications. At the same time, these twists illustrate the resiliency of curiosity as we develop new methods and ideas to forge ahead in a bid to understand the world around us. In a world that is changing rapidly, I can only hope to engage this curiosity further by exploring the natural world and collaborating with other curious people, and to be as resilient as the populations that persist nevertheless.

BIBLIOGRAPHY

[1] W. C. Allee, O. Park, A. E. Emerson, T. Park, and K. P. Schmidt. *Principles of Animal Ecology*. Saunders Company, Philadelphia, 1949.

[2] E. J. Allen, L. J. S. Allen, and X. Gilliam. Dispersal and competition models for plants. *J. Math. Biol.*, 34:455–481, 1996.

[3] M. Andersen. Properties of some density-dependent integrodifference equation population models. *Math. Biosci.*, 104:135–157, 1991.

[4] T. M. Apostol. *Mathematical Analysis*. Addison-Wesley Publishing Company, Reading, second edition, 1974.

[5] V. I. Arnol'd. Loss of stability of self-oscillations close to resonance and versal deformations of equivariant vector fields. *Funct. Anal. its Appl.*, 11:85–92, 1977.

[6] D. G. Aronson, M. A. Chory, G. R. Hall, and R. P. McGehee. Bifurcations from an invariant circle for two-parameter families of maps of the plane: A computer assisted study. *Commun. Math. Phys.*, 83:303–354, 1982.

[7] E. Babolian, Z. Masouri, and S. Hatamzadeh-Varmazyar. New direct method to solve nonlinear Volterra-Fredholm integral and integro-differential equations using operational matrix with block-pulse functions. *Prog. Electromagn. Res. B*, 8:59–76, 2008.

[8] M. A. Balcı and M. Sezer. Hybrid Euler–Taylor matrix method for solving of generalized linear Fredholm integro-differential difference equations. *Appl. Math. Comput.*, 273:33–41, 2016.

[9] B. E. Beisner, D. T. Haydon, and K. Cuddington. Alternative stable states in ecology. *Front. Ecol. Environ.*, 1:376–382, 2003.

[10] R. J. H. Beverton and S. J. Holt. *On the Dynamics of Exploited Fish Populations*. Her Majesty's Stationery Office, London, 1957.

[11] D. S. Boukal and L. Berec. Single-species models of the Allee effect: Extinction boundaries, sex ratios and mate encounters. *J. Theor. Biol.*, 218:375–394, 2002.

[12] J. Bramburger and F. Lutscher. Analysis of integrodifference equations with a separable dispersal kernel. *Acta. Appl. Math*, 161:127–151, 2019.

[13] S. Brown, J. Dockery, and M. Pernarowski. Traveling wave solutions of a reaction diffusion model for competing pioneer and climax species. *Math. Biosci.*, 194:21–36, 2005.

[14] J. R. Buchanan. Asymptotic behavior of two interacting pioneer/climax species. *Fields Inst. Commun.*, 21:51–63, 1999.

[15] J. R. Buchanan and J. F. Selgrade. Constant and periodic rate stocking and harvesting for Kolmogorov-type population interaction models. *Rocky Mt. J. Math.*, 25:76–85, 1995.

[16] B. Buonomo and S. Rionero. Linear and nonlinear stability thresholds for a diffusive model of pioneer and climax species interaction. *Math. Methods Appl. Sci.*, 32:811–824, 2009.

[17] M. L. Cain, B. G. Milligan, and A. E. Strand. Long-distance seed dispersal in plant populations. *Am. J. Bot.*, 87:1217–1227, 2000.

[18] J. Cao and P. Weng. Single spreading speed and traveling wave solutions of a diffusive pioneer–climax model without cooperative property. *Commun. Pure Appl. Anal.*, 16:1405–1426, 2017.

[19] I. Chen, J. K. Hill, R. Ohlemüller, D. B. Roy, and C. D. Thomas. Rapid range shifts of species associated with high levels of climate warming. *Science*, 333:1024–1026, 2011.

[20] J. S. Clark. Why trees migrate so fast: Confronting theory with dispersal biology and the paleorecord. *Am. Nat.*, 152:204–224, 1998.

[21] J. S. Clark, C. Fastie, G. Hurtt, S. T. Jackson, C. Johnson, G. A. King, M. Lewis, J. Lynch, S. Pacala, C. Prentice, E. W. Schupp, T. Webb III, and P. Wyckoff. Reid's Paradox of rapid plant migration. *BioScience*, 48:13–24, 1998.

[22] J. S. Clark, M. Lewis, and L. Horvath. Invasion by extremes: Population spread with variation in dispersal and reproduction. *Am. Nat.*, 157:537–554, 2001.

[23] C. A. Cobbold and R. Stana. Should I stay or should I go: Partially sedentary populations can outperform fully dispersing populations in response to climate-induced range shifts. *Bull. Math. Biol.*, 82, 2020.

[24] O. Cornejo-Pérez and I. Barradas. Dynamics of a pioneer–climax species model with migration. *Appl. Math. Model.*, 39:6568–6579, 2015.

[25] F. Courchamp, T. Clutton-Brock, and B. Grenfell. Inverse density dependence and the Allee effect. *Trends Ecol. Evol.*, 14:405–410, 1999.

[26] F. Courchamp, L. Berec, and J. Gascoigne. *Allee Effects in Ecology and Conservation*. Oxford University Press, Oxford, 2008.

[27] J. H. Curry and J. A. Yorke. A transition from Hopf bifurcation to chaos: Computer experiments on maps in R^2. In N. G. Markley, J. C. Martin, and W. Perrizo, editors, *The Structure of Attractors in Dynamical Systems*, pages 48–68, Berlin, 1978. Springer-Verlag.

[28] J. M. Dalling. Pioneer species. In B. D. Fath, editor, *Encyclopedia of Ecology*, pages 181–184. Elsevier, Amsterdam, 2019.

[29] R. Descartes. *[1637] La Géométrie*. Hermann, A., Paris, 1886.

[30] S. W. Dharmadhikari and K. Joag-Dev. *Unimodality, Convexity, and Applications*. Academic Press, Boston, 1988.

[31] J. M. Diez, C. M. D'Antonio, J. S. Dukes, E. D. Grosholz, J. D. Olden, C. J. B. Sorte, D. M. Blumenthal, B. A. Bradley, R. Early, E. Ibáñez, S. J. Jones, J. J. Lawler, and L. P. Miller. Will extreme climatic events facilitate biological invasions? *Front. Ecol. Environ.*, 10:249–257, 2012.

[32] J. W. Eaton, D. Bateman, S. Hauberg, and R. Wehbring. GNU Octave version 7.3.0 manual: a high-level interactive language for numerical computations, 2022. URL https://urldefense.com/v3/__https://www.gnu.org/software/octave/doc/v7.3.0/__;!!K-Hz7m0Vt54!hyoxjUTEWcmRDh-K66WibBLB9G8jRhTNcJUSwSXw5BY7wvipjTDZp_8XjrV9OTlIuK_wzlZAGXP78U9Lpf4$.

[33] A. Ebadian and A. A. Khajehnasiri. Block-pulse functions and their applications to solving systems of higher-order nonlinear Volterra integro-differential equations. *Electron. J. Differ. Equ.*, 2014:1–9, 2014.

[34] R. Etienne, B. Wertheim, L. Hemerik, P. Schneider, and J. Powell. The interaction between dispersal, the Allee effect and scramble competition affects population dynamics. *Ecol. Model.*, 148:153–168, 2002.

[35] W. F. Fagan and F. Lutscher. Average dispersal success: Linking home range, dispersal, and metapopulation dynamics to reserve design. *Ecol. Appl.*, 16:820–828, 2006.

[36] W. F. Fagan, M. A. Lewis, M. G. Neubert, C. Aumann, J. L. Apple, and J. G. Bishop. When can herbivores slow or reverse the spread of an invading plant? A test case from Mount St. Helens. *Am. Nat.*, 166:669–685, 2005.

[37] R. A. Fisher. The wave of advance of advantageous genes. *Ann. Eugen.*, 7:355–369, 1937.

[38] C. Folke, S. R. Carpenter, B. Walker, M. Scheffer, T. Elmqvist, L. Gunderson, and C. S. Holling. Regime shifts, resilience, and biodiversity in ecosystem management. *Annu. Rev. Ecol. Evol. Syst.*, 35:557–581, 2004.

[39] J. E. Franke and A. A. Yakubu. Exclusion principles for density-dependent discrete pioneer–climax models. *J. Math. Anal. Appl.*, 187:1019–1046, 1994.

[40] J. E. Franke and A. A. Yakubu. Pioneer exclusion in a one-hump discrete pioneer–climax competitive system. *J. Math. Biol.*, 32:771–787, 1994.

[41] K. Gagnon, S. J. Peacock, Y. Jin, and M. A. Lewis. Modelling the spread of the invasive alga *Codium fragile* driven by long-distance dispersal of buoyant propagules. *Ecol. Model.*, 316:111–121, 2015.

[42] N. M. Gilbertson and M. Kot. Dynamics of a discrete-time pioneer–climax model. *Theor. Ecol.*, 14:501–523, 2021.

[43] N. M. Gilbertson and M. Kot. Block-pulse integrodifference equations. Unpublished manuscript, 2022.

[44] M. E. Gilpin and M. E. Soule. Minimum viable populations: Processes of species extinctions. In M. E. Soule, editor, *Conservation Biology: The Science of Scarcity and Diversity*. Sinauer Associates, Sunderland, 1986.

[45] D. W. Goodsman and M. A. Lewis. The minimum founding population in dispersing organisms subject to strong Allee effects. *Methods Ecol. Evol.*, 7:1100–1109, 2016.

[46] J. L. Harper. *Population Biology of Plants*. Academic Press, London, 1977.

[47] M. A. Harsch, Y. Zhou, J. HilleRisLambers, and M. Kot. Keeping pace with climate change: stage-structured moving-habitat models. *Am. Nat.*, 184:25–37, 2014.

[48] M. A. Harsch, A. Phillips, Y. Zhou, M. R. Leung, D. S. Rinnan, and M. Kot. Moving forward: Insights and applications of moving-habitat models for climate change ecology. *J. Ecol.*, 105:1169–1181, 2017.

[49] T. H. Hildebrandt. *Introduction to the Theory of Integration*. Academic Press, New York, 1963.

[50] H. S. Horn. The ecology of secondary succession. *Annu. Rev. Ecol. Evol. Syst.*, 5:25–37, 1974.

[51] Y. Huang and P. Weng. Traveling wavefronts of a diffusive competing pioneer and climax system with delays. *Math. Comput. Model.*, 57:2532–2548, 2013.

[52] A. Hurford, M. Hebblewhite, and M. A. Lewis. A spatially explicit model for an Allee effect: Why wolves recolonize so slowly in Greater Yellowstone. *Theor. Popul. Biol.*, 70: 244–254, 2006.

[53] A. Hurford, C. A. Cobbold, and P. K. Molnár. Skewed temperature dependence affects range and abundance in a warming world. *Proc. R. Soc. B*, 286:1157–1166, 2019.

[54] V. Hutson and J. S. Pym. *Applications of Functional Analysis and Operator Theory*. Academic Press, New York, 1980.

[55] I. A. Ibragimov. On the composition of unimodal distributions. *Theory Probab. its Appl.*, 1: 255–260, 1956.

[56] Z. H. Jiang and W. Schaufelberger. *Block Pulse Functions and Their Applications in Control Systems*. Springer Berlin Heidelberg, Berlin Heidelberg, 1992.

[57] D. M. Johnson, A. M. Liebhold, P. C. Tobin, and O. N. Bjørnstad. Allee effects and pulsed invasion by the gypsy moth. *Nature*, 444:361–363, 2006.

[58] Y. Joshi and D. Blackmore. Bifurcation and chaos in higher dimensional pioneer–climax systems. *Int. Electron. J. Pure Appl. Math.*, 1:303–337, 2010.

[59] E. I. Jury. *Theory and Application of the z-Transform Method*. Wiley, New York, 1964.

[60] L. V. Kantorovich and G. P. Akilov. *Functional Analysis*. Pergamon Press, Oxford, 1982.

[61] T. H. Keitt, M. A. Lewis, and R. D. Holt. Allee effects, invasion pinning, and species' borders. *Am. Nat.*, 157:203–216, 2001.

[62] H. Kim and J. A. Marlin. Solutions of a pioneer–climax model. *Can. Appl. Math. Q.*, 7: 143–158, 1999.

[63] M. Kot and A. Phillips. Bounds for the critical speed of climate-driven moving-habitat models. *Math. Biosci.*, 262:65–72, 2015.

[64] M. Kot and W. M. Schaffer. Discrete-time growth-dispersal models. *Math. Biosci.*, 80: 109–136, 1986.

[65] M. Kot, M. A. Lewis, and P. van den Driessche. Dispersal data and the spread of invading organisms. *Ecology*, 77:2027–2042, 1996.

[66] A. M. Kramer, L. Berec, and J. M. Drake. Editorial: Allee effects in ecology and evolution. *J. Anim. Ecol.*, 87:7–10, 2018.

[67] M. A. Krasnosel'skii, G. M. Vainikko, P. P. Zabreiko, Y. B. Rutitskii, and V. Y. Stetsenko. *Approximate Solution of Operator Equations*. Wolters-Noordhoff Publishing, Groningen, 1972.

[68] Y. A. Kuznetsov. *Elements of Applied Bifurcation Theory*. Springer, New York, 2004.

[69] J. Latore, P. Gould, and A. M. Mortimer. Spatial dynamics and critical patch size of annual plant populations. *J. Theor. Biol.*, 190:277–285, 1998.

[70] H. A. Lauwerier. Two-dimensional iterative maps. In A. V. Holden, editor, *Chaos*, pages 58–95. Princeton Univ. Press, Princeton, 1986.

[71] C. T. Lee, M. F. Hoopes, J. Diehl, W. Gilliland, G. Huxel, E. V. Leaver, K. McCann, J. Umbanhowar, and A. Mogilner. Non-local concepts and models in biology. *J. Theor. Biol.*, 210: 201–219, 2001.

[72] J. Lenoir, J. C. Gégout, P. A. Marquet, P. de Ruffray, and H. Brisse. A significant upward shift in plant species optimum elevation during the 20th century. *Science*, 320:1768–1771, 2008.

[73] J. M. Levine and C. M. D'Antonio. Forecasting biological invasions with increasing international trade. *Conserv. Biol.*, 17:322–326, 2003.

[74] M. A. Lewis and P. Kareiva. Allee dynamics and the spread of invading organisms. *Theor. Popul. Biol.*, 43:141–158, 1993.

[75] M. A. Lewis, B. Li, and H. F. Weinberger. Spreading speed and linear determinacy for two-species competition models. *J. Math. Biol.*, 45:219–233, 2002.

[76] M. A. Lewis, S. V. Petrovskii, and J. R. Potts. *The Mathematics Behind Biological Invasions*. Springer, Cham, 2016.

[77] B. Li and G. Otto. Wave speed and critical patch size for integro-difference equations with a strong Allee effect. *J. Math. Biol.*, 85:59, 2022.

[78] B. Li, H. F. Weinberger, and M. A. Lewis. Spreading speeds as slowest wave speeds for cooperative systems. *Math. Biosci.*, 196:82–98, 2005.

[79] M. Liermann and R. Hilborn. Depensation: Evidence, models and implications. *Fish Fish.*, 2:33–58, 2001.

[80] B. Liu and M. Kot. Accelerating invasions and the asymptotics of fat-tailed dispersal. *J. Theor. Biol.*, 471:22–41, 2019.

[81] J. Liu and J. Wei. Bifurcation analysis of a diffusive model of pioneer and climax species interaction. *Adv. Differ. Equ.*, 2011:1–11, 2011.

[82] D. R. Lockwood, A. Hastings, and L. W. Botsford. The effects of dispersal patterns on marine reserves: Does the tail wag the dog? *Theor. Popul. Biol.*, 61:297–309, 2002.

[83] R. Lui. Existence and stability of travelling wave solutions of a nonlinear integral operator. *J. Math. Biol.*, 16:199–220, 1983.

[84] F. Lutscher. *Integrodifference Equations in Spatial Ecology*. Springer, Cham, 2019.

[85] F. Lutscher and M. A. Lewis. Spatially-explicit matrix models. A mathematical analysis of stage-structured integrodifference equations. *J. Math. Biol.*, 48:293–324, 2004.

[86] F. Lutscher and S. V. Petrovskii. The importance of census times in discrete-time growth-dispersal models. *J. Biol. Dynam.*, 2:55–63, 2008.

[87] W. A. J. Luxemburg. Arzela's dominated convergence theorem for the Riemann integral. *Amer. Math. Monthly*, 78:970–979, 1971.

[88] K. Maleknejad, B. Basirat, and E. Hashemizadeh. Hybrid Legendre polynomials and Block-Pulse functions approach for nonlinear Volterra–Fredholm integro-differential equations. *Comput. Math. with Appl.*, 61:2821–2828, 2011.

[89] K. Marcinko. *Mathematical analysis of host–parasitoid dynamics*. PhD thesis, University of Washington, 2020.

[90] MATLAB. *version 9.6.0.1214997 (R2019a)*. The MathWorks Inc., Natick, 2019.

[91] J. R. McAuliffe. Markovian dynamics of simple and complex desert plant communities. *Am. Nat.*, 131:459–490, 1988.

[92] R. P. McIntosh. *The Background of Ecology*. Cambridge University Press, New York, 1985.

[93] G. A. Monteiro, U. M. Hanung, and M. Tvrdý. Bounded convergence theorem for abstract Kurzweil–Stieltjes integral. *Monatsh. Math.*, 180:409–434, 2016.

[94] G. A. Monteiro, A. Slavík, and M. Tvrdý. *Kurzweil–Stieltjes Integral: Theory and Applications*. World Scientific Publishing Co., Singapore, 2019.

[95] J. D. Murray. *Mathematical Biology: I. An Introduction*. Springer, Berlin Heidelberg, third edition, 2002.

[96] M. Nestor and B. Li. Periodic traveling waves in an integro-difference equation with non-monotonic growth and strong Allee effect. Preprint at https://doi.org/10.48550/arXiv.2202.00234, 2022.

[97] M. G. Neubert and M. Kot. The subcritical collapse of predator populations in discrete-time predator–prey models. *Math. Biosci.*, 110:45–66, 1992.

[98] A. Okubo and S. A. Levin. A theoretical framework for data analysis of wind dispersal of seeds and pollen. *Ecology*, 70:329–338, 1989.

[99] G. L. Otto. *Nonspreading solutions in integro-difference models with Allee and overcompensation effects*. PhD thesis, University of Louisville, 2017.

[100] J. M. Pandolfi. Succession. In B. D. Fath, editor, *Encyclopedia of Ecology*, pages 616–623. Elsevier, Amsterdam, 2019.

[101] P. S. Petraitis. *Multiple Stable States in Natural Ecosystems*. Oxford University Press, Oxford, 2013.

[102] A. Phillips and M. Kot. Persistence in a two-dimensional moving-habitat model. *Bull. Math. Biol.*, 77:2125–2159, 2015.

[103] D. Pimentel, R. Zuniga, and D. Morrison. Update on the environmental and economic costs associated with alien-invasive species in the United States. *Ecol. Econ.*, 52:273–288, 2005.

[104] R. Precup. *Methods in Nonlinear Integral Equations*. Kluwer Academic Publishers, Dordrecht, 2002.

[105] S. Purkayastha. Simple proofs of two results on convolutions of unimodal distributions. *Stat. Probab. Lett.*, 39:97–100, 1998.

[106] R Core Team. R: A language and environment for statistical computing, 2021. URL https://www.R-project.org/.

[107] L. B. Rall. *Computational Solution of Nonlinear Operator Equations*. Wiley, New York, 1969.

[108] K. Ralls, P. H. Harvey, and A. M. Lyles. Inbreeding in natural populations of birds and mammals. In M. E. Soule, editor, *Conservation Biology: The Science of Scarcity and Diversity*. Sinauer Associates, Sunderland, 1986.

[109] G. P. Rao. *Piecewise Constant Orthogonal Functions and Their Application to Systems and Control*. Springer Berlin Heidelberg, Berlin Heidelberg, 1983.

[110] J. R. Reimer, M. B. Bonsall, and P. K. Maini. Approximating the critical domain size of integrodifference equations. *Bull. Math. Biol.*, 78:72–109, 2016.

[111] E. Renshaw. *Modelling Biological Populations in Space and Time*. Cambridge University Press, Cambridge, 1991.

[112] W. E. Ricker. Stock and recruitment. *J. Fish. Res. Bd. Can.*, 11:559–623, 1954.

[113] D. S. Rinnan. The dispersal success and persistence of populations with asymmetric dispersal. *Theor. Ecol.*, 11:55–69, 2018.

[114] D. S. Rinnan. Population persistence in the face of climate change and competition: A battle on two fronts. *Ecol. Model.*, 385:78–88, 2018.

[115] M. Scheffer and S. R. Carpenter. Catastrophic regime shifts in ecosystems: Linking theory to observation. *Trends Ecol. Evol.*, 18:648–656, 2003.

[116] A. Schröder, L. Persson, and A. M. De Roos. Direct experimental evidence for alternative stable states: A review. *Oikos*, 110:3–19, 2005.

[117] R. Seidl, D. Thom, M. Kautz, D. Martin-Benito, M. Peltoniemi, G. Vacchiano, J. Wild, D. Ascoli, M. Petr, J. Honkaniemi, M. J. Lexer, V. Trotsiuk, P. Mairota, M. Svoboda, M. Fabrika, T. A. Nagel, and C. P. O. Reyer. Forest disturbances under climate change. *Nat. Clim. Chang.*, 7:395–402, 2017.

[118] J. F. Selgrade. Planting and harvesting for pioneer–climax models. *Rocky Mt. J. Math.*, 24: 293–310, 1994.

[119] J. F. Selgrade. Using stocking or harvesting to reverse period-doubling bifurcations in discrete population models. *J. Differ. Equ. Appl.*, 4:163–183, 1998.

[120] J. F. Selgrade and G. Namkoong. Stable periodic behavior in a pioneer–climax model. *Nat. Resour. Model.*, 4:215–227, 1990.

[121] J. F. Selgrade and G. Namkoong. Population interactions with growth rates dependent on weighted densities. In S. Busenberg and M. Martelli, editors, *Differential Equations Models in Biology, Epidemiology and Ecology*, pages 247–256, Berlin, 1991. Springer-Verlag.

[122] J. F. Selgrade and J. H. Roberds. Lumped-density population models of pioneer–climax type and stability analysis of Hopf bifurcations. *Math. Biosci.*, 135:1–21, 1996.

[123] J. F. Selgrade and J. H. Roberds. Period-doubling bifurcations for systems of difference equations and applications to models in population biology. *Nonlinear Anal. Theory Methods Appl.*, 29:185–199, 1997.

[124] J. F. Selgrade and J. H. Roberds. Reversing period-doubling bifurcations in models of population interactions using constant stocking or harvesting. *Can. Appl. Math. Q.*, 6:207–231, 1998.

[125] N. Shigesada and K. Kawasaki. *Biological Invasions: Theory and Practice*. Oxford University Press, Oxford, 1997.

[126] D. Simberloff, J. Martin, P. Genovesi, V. Maris, D. A. Wardle, J. Aronson, F. Courchamp, B. Galil, E. García-Berthou, M. Pascal, P. Pyšek, R. Sousa, E. Tabacchi, and M. Vilá. Impacts of biological invasions: What's what and the way forward. *Trends Ecol. Evol.*, 28: 58–66, 2013.

[127] J. G. Skellam. Random dispersal in theoretical populations. *Biometrika*, 38:196–218, 1951.

[128] M. Slatkin. Gene flow and selection in a cline. *Genetics*, 75:733–756, 1973.

[129] P. A. Stephens and W. J. Sutherland. Consequences of the Allee effect for behaviour, ecology and conservation. *Trends Ecol. Evol.*, 14:401–405, 1999.

[130] L. L. Sullivan, B. Li, T. E. X. Miller, M. G. Neubert, and A. K. Shaw. Density dependence in demography and dispersal generates fluctuating invasion speeds. *Proc. Natl. Acad. Sci. U.S.A.*, 114:5053–5058, 2017.

[131] S. Sumner. Hopf bifurcation in pioneer–climax competing species models. *Math. Biosci.*, 137:1–24, 1996.

[132] S. Sumner. Stable periodic behavior in pioneer–climax competing species models with constant rate forcing. *Nat. Resour. Model.*, 11:155–171, 1998.

[133] C. M. Taylor. Allee effects. In A. Hastings and L. J. Gross, editors, *Encyclopedia of Theoretical Ecology*. University of California Press, Berkeley, 2012.

[134] C. M. Taylor and A. Hastings. Allee effects in biological invasions. *Ecol. Lett.*, 8:895–908, 2005.

[135] J. M. T. Thompson, H. B. Stewart, and Y. Ueda. Safe, explosive, and dangerous bifurcations in dissipative dynamical systems. *Phys. Rev. E*, 49:1019–1027, 1994.

[136] D. Tilman. *Plant Strategies and the Dynamics and Structure of Plant Communities*. Princeton University Press, Princeton, 1988.

[137] P. C. Tobin, L. Berec, and A. M. Liebhold. Exploiting Allee effects for managing biological invasions. *Ecol. Lett.*, 14:615–624, 2011.

[138] I. M. Turner. *The Ecology of Trees in the Tropical Rain Forest*. Cambridge University Press, Cambridge, 2001.

[139] R. W. Van Kirk and M. A. Lewis. Integrodifference models for persistence in fragmented habitats. *Bull. Math. Biol.*, 59:107–137, 1997.

[140] R. W. Van Kirk and M. A. Lewis. Edge permeability and population persistence in isolated habitat patches. *Nat. Resour. Model.*, 12:37–64, 1999.

[141] R. R. Veit and M. A. Lewis. Dispersal, population growth, and the Allee effect: Dynamics of the house finch invasion of eastern North America. *Am. Nat.*, 148:255–274, 1996.

[142] G. Walther, A. Roques, P. E. Hulme, M. T. Sykes, P. Pyšek, I. Kühn, M. Zobel, S. Bacher, Z. Botta-Dukát, H. Bugmann, B. Czúcz, J. Dauber, T. Hickler, V. Jarošík, M. Kenis, S. Klotz, D. Minchin, M. Moora, W. Nentwig, J. Ott, V. E. Panov, B. Reineking, C. Robinet, V. Semenchenko, W. Solarz, W. Thuiller, M. Vilá, K. Vohland, and J. Settele. Alien species in a warmer world: Risks and opportunities. *Trends Ecol. Evol.*, 24:686–693, 2009.

[143] M. H. Wang, M. Kot, and M. G. Neubert. Integrodifference equations, Allee effects, and invasions. *J. Math. Biol.*, 44:150–168, 2002.

[144] H. F. Weinberger. Long-time behavior of a class of biological models. *SIAM J. Math. Anal.*, 13:353–396, 1982.

[145] H. F. Weinberger, M. A. Lewis, and B. Li. Analysis of linear determinacy for spread in cooperative models. *J. Math. Biol.*, 45:183–218, 2002.

[146] H. F. Weinberger, M. A. Lewis, and B. Li. Anomalous spreading speeds of cooperative recursion systems. *J. Math. Biol.*, 55:207–222, 2007.

[147] P. Weng and X. Zou. Minimal wave speed and spread speed of competing pioneer and climax species. *Appl. Anal.*, 93:2093–2110, 2014.

[148] W. Werner. Some improvements of classical iterative methods for the solution of nonlinear equations. In E. L. Allgower, K. Glashoff, and H. O. Peitgen, editors, *Numerical Solution of Nonlinear Equations*, volume 878. Springer Berlin Heidelberg, Berlin, Heidelberg, 1981.

[149] D. Whitley. Discrete dynamical systems in dimensions one and two. *Bull. London Math. Soc.*, 15:177–217, 1983.

[150] A. Wintner. *Asymptotic Distributions and Infinite Convolutions*. Edwards Brothers, Ann Arbor, 1938.

[151] X. Yu, P. Weng, and Y. Huang. Traveling wavefronts of competing pioneer and climax model with nonlocal diffusion. *Abstr. Appl. Anal.*, 2013:1–12, 2013.

[152] Z. Yuan and X. Zou. Co-invasion waves in a reaction diffusion model for competing pioneer and climax species. *Nonlinear Anal. Real World Appl.*, 11:232–245, 2010.

[153] Y. Zhou and M. Kot. Discrete-time growth-dispersal models with shifting species ranges. *Theor. Ecol.*, 4:13–25, 2011.

[154] Y. Zhou and M. Kot. Life on the move: Modeling the effects of climate-driven range shifts with integrodifference equations. In M. A. Lewis, P. K. Maini, and S. V. Petrovskii, editors, *Dispersal, Individual Movement and Spatial Ecology: A Mathematical Perspective*. Springer Berlin Heidelberg, Berlin, 2013.